Politecnico di Torino
Dissertation for the attainment of the Italian "Laurea Magistrale"
Degree in Biomedical Engineering

Analysis of spatial parameters during gait with magneto-inertial sensors and infrared proximity sensors

Supervisors:
Prof. Ing. Marco Knaflitz
Prof. Ing. Andrea Cereatti
Dott. Ing. Marco Caruso

Candidate:
Rachele Rossanigo

December 2019

Acknowledgements

Questo lavoro è il termine del mio lungo percorso scolastico e universitario, che non sarebbe stato possibile senza le tante persone che ora devo ringraziare.

A livello accademico ringrazio il Professor Marco Knaflitz e il Professor Andrea Cereatti per le opportunità che mi sono state offerte e per la disponibilità che hanno mostrato nei miei confronti. Ringrazio di cuore tutti i ragazzi dell'ufficio in cui ho svolto la tesi, Stefano, Francesca e, soprattutto, Marco per l'enorme pazienza, gentilezza ed efficienza con cui hanno sempre risposto alle mie molte domande e risolto i miei dubbi.

Il ringraziamento più sentito va a tutta la mia famiglia, che mi ha sostenuta sia economicamente che moralmente in questi cinque anni di università. Il grazie più doveroso di tutti va ai miei fantastici genitori, che hanno saputo sempre indirizzarmi con saggezza senza mai impormi nulla, e ai miei nonni.

Non posso non ringraziare i miei amici e i miei compagni di corso che mi sono stati vicini in questi anni e soprattutto in questi ultimi mesi. In particolare ringrazio i miei più grandi amici, gli amici di sempre, Christopher, Beatrice, Milena, Laura, Elisabetta, Antonina e Sara. Li ringrazio perché hanno saputo, a volte inconsapevolmente, farmi sorridere e divertire anche quando non pensavo di essere dell'umore adatto per farlo. Ringrazio Benedetta, che mi ha permesso di sopravvivere in Svezia e ha fatto sì che il mio Erasmus diventasse un'esperienza piena di bei ricordi. Grazie anche a Diletta che più di tutti ha condiviso questo percorso di tesi con me.

Per ultimo, ma non per importanza, devo ringraziare Jurgen che ha subito più di tutti le mie frustrazioni e che nonostante tutto è ancora accanto a me.

Contents

Abstract

This thesis aims at estimating the base of support (BoS) during gait, that is defined as the area over which the body is supported during the double-support phase when both feet are in contact with the ground. The measure of BoS is helpful in evaluating gait disorders. In literature we observe the lack of studies that propose methods for BoS estimation outside human motion laboratories. Hence, this is a feasibility study that aims at implementing and evaluating the performance of an innovative method which provides the BoS estimate and can be suitable for applications out of the human motion laboratory. The hardware chosen for this thesis is a combination of Magneto-Inertial Measurement Units (MIMU) and the Infrared Time of Flight (IR ToF) sensors. During the last decades MIMU-based systems have become a promising hardware in motion analysis, enabling the orientation estimation of the body portion on which they are attached. The huge spread of these sensors has allowed an out-of-lab and low cost evaluation of gait alterations [5]. Although MIMUs are largely used in literature for gait analysis, they are not sufficient to calculate the relative distance between the feet, which is necessary for the estimation of the base of support. This additive information is provided by the IR ToF sensors, which, in this study, are attached on one instrumented foot and are used to 'scan' the opposite one.
In light of the above, my thesis comprises multiple sub-tasks and thus the workflow can be summarized in four principal steps:

1. the orientation estimation,
2. the position estimation,
3. the detection of the non-instrumented foot and the identification of a common reference coordinate system for both feet,
4. the validation of my entire method of BoS estimation with a stereophotogrammetric system.

The choice of the orientation estimation algorithm fell on a deterministic complementary filter and it is treated in Chapter 9. The implemented sensor fusion algorithm is based on the filter proposed by Madgwick in 2010 [36], which is quaternion-based and dependant on a single parameter. The accuracy of the sensor fusion algorithm was tested with specific experiments.
The displacement estimation is achieved with a double integration of the accelerations provided by the MIMU, which suffers from drift errors. Some methods are implemented and discussed in Chapter 10 to improve the position estimate and reduce the drift problem. Also the accuracy of the displacement estimation was tested with specific experiments.
To refer both feet to the same coordinate system, the inter-feet distances are measured with IR ToF sensors, the detected foot is modeled and the points of this model must be rotated in the same frame of the other foot.
Once both feet models positions are known, the BoS can be obtained.
Hence this study will comprise in Part I an introduction to the problem and the used hardware, in Part II an explanation of implemented methods, in Part III the procedures for validation.

Keywords: magneto-inertial sensors, wearable sensors, gait analysis, spatial parameters, infrared proximity sensors, inter-feet distance, base of support.

Abbreviations

MIMU	Magneto-Inertial Measurement Unit
SP	Stereophotogrammetry
GCS	Glabal Coordinate System
ECS	Earth's Coordinate System
LCS	Local Coordinate System
IR ToF	Infrared Time-of-Flight
DS	Distance Sensor
SL	Stride Length
SW	Step Width
BoS	Base of Support
IFD	Inter-Feet Distance
RMSd	Root Mean Square Deviation
GE	Gait Events
FF	Flat Foot instant
INDIP	INertal DIstance Sensors and Pressure Insoles

Chapter 1

Background

1.1 Clinical relevance

The clinical relevance of gait analysis is founded on the fact that walking is the most common daily life activity and hides a lot of information about the subject's health. Thus the gait analysis can be defined as the systematic, qualitative and quantitative study of the human motion while walking. It is supported by certain instrumentation for measuring body mechanics and movement and the muscle activity and, thus, the locomotion pattern. During the last decades gait analysis increases its importance and spreads in fields such as:

- the sport biomechanics to help athletes to improve their performances;
- the clinical targeted rehabilitation, periodically assessing a gait disorder and quantitatively describing the progression of the gait pathology;
- the functional diagnostics of diseases related to motor impairments identifying posture-related and movement-related problems.

To reach the goal of quantification of gait alterations, some measurable parameters must be defined. This study focuses on the base of support (BoS) estimation, so the principal aspects of gait analysis that have to be take into account are all the spatio-temporal parameters of the gait cycle related to stride and step. They will be described later.

Anyway, the accurate estimation of all the gait parameters has a crucial importance in providing reliable information as biomarker of mobility on the evolution of different diseases [1], such as:

- neurological diseases as the multiple sclerosis or Parkinson's;
- systemic diseases as the cardiopathies;
- alterations in deambulation due to stroke;
- diseases caused by ageing.

An example reported in [2] assesses that gait disturbances are shown to be an early indicator of mild cognitive impairment (MCI) till to forecast the degeneration of MCI to Alzheimer's disease.
Anoter example is provided by Salarian *et al.*, 2004, [3], who showed an application of the gait analysis to Parkinson's disease (PD), which is one of the most common degenerative diseases in the world population. They use gyroscopes attached to various parts of the body to estimate

spatio-temporal gait parameters, such as stride length, stride velocity, stance duration, double support duration, gait cycle time. The results found that the PD patients showed significant difference in all the parameters if compared to the data of the control group.

The clinical relevance of the BoS contains fundamental information relative to the equilibrium balance of the patient and this can be studied analysing the trajectory of the center of pressure and the limits of the BoS area [10]. Furthermore, the differences of BoS features can quantitatively describe several gait disorders and discriminate among them, as Figure 1.1 shows. Pirker *et al.* in [31] highliths in this reported figure some peculiarity of every analysed abnormal walking: the paraspastic gait is characterized by narrow step width and inwards rotation, the cerebellar gait by broadened base of support, the Parkinson's disease by the shortened and irregular step length, the frontal gait by the irregular walking with short step length and wider step width.

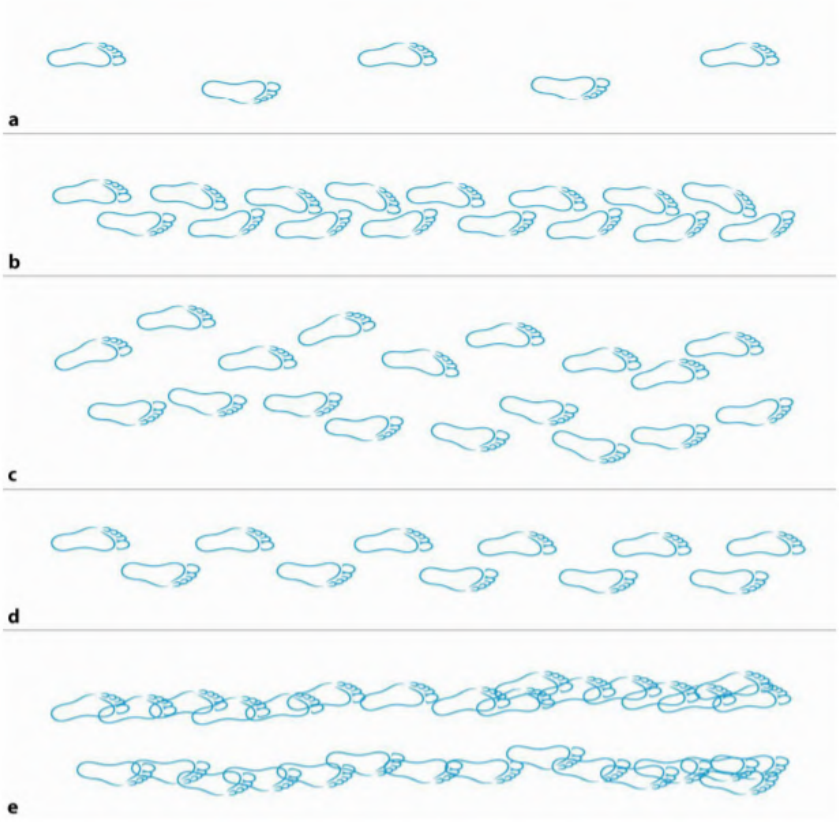

Figure 1.1: *This figure, taken from [31], representes the step sequence in common gait disorders. It is useful to understand how the base of support can be a relevant parameter for describing different types of pathological walkings. The letters refer to: a) Normal gait, b) Spastic paraparetic gait, c) Cerebellar ataxic gait, d) Parkinsonian gait, e) Frontal gait.*

1.2 Towards out-of-lab gait analysis

There are many existing methods to evaluate the spatio-temporal parameters of the gait, which comprises non wearable sensors (such as image processing, floor sensors, stereo-photogrammetry) and wearable sensors that includes accelerometers, gyroscopes, magnetometers, force sensors, extensometers, goniometers, active markers, electromyography [4]. Although the stereopho-

togrammetry (SP) is considered the gold standard, it is expensive and its use is limited to the laboratory environment. Furthermore, these motion capture systems imply complexity of measurements, which, together with the high cost and time-consume, limit their use in many laboratories. Therefore, it has become more and more important to find alternative solutions that do not require such instrumentation.

With the advance in microfabrication technology, the (M)IMUs (Magneto-Inertial Measurement Units) are largely used in motion analysis in last decades. These units are composed by a miniaturized accelerometer, gyroscope and magnetometer. Their spread in the field of gait analysis is due to the fact that they are low-cost, lightweight, source-less (despite other approaches such as optical/ ultrasonic/ electromagnetic trackers), low powered. They also guarantee fast responsibility and portability and enable their data to be processed on a microcontroller unit embedded in the MIMU, so they are self-contained. Since the usage of these units is not complicated, they can be mounted directly by the patients without any technical knowledge. For all these reasons, MIMUs are suitable for monitoring the follow up of patients with movement disorders or evaluating the gait alterations in clinical assessments as well as during daily life activities and over extended periods of time [5].

Nevertheless, MIMUs do not provide directly the measurements of interest in gait analysis, which are related to displacements, areas or angles, but their data must be merged together to obtain a significant information, that is the orientation of the body in which they are attached. Hence, the estimates depend not only on the performance of the hardware but also on the filtering algorithms of sensor fusion.

1.3 Base of support

The base of support (BoS) is defined as the area surrounding all the points of contact with the ground of a generic body. It is a key parameter for the evaluation of balance of the body. An object or a person are in balance if the center of pressure is inside the BoS, while, if it is not, thus the body falls. The center of pressure is the point where the line of gravity passing through the center of gravity touches the ground. The center of gravity (or center of mass) is the average position of all object's weight distribution.

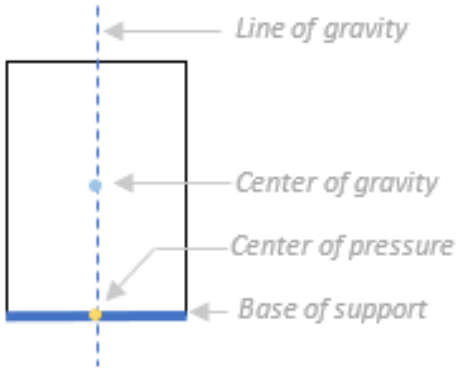

Figure 1.2: *Scheme of a generic object with its center of gravity, line of gravity, center of pressure, base of support.*

If there are more than one points of contact, then the BoS is the area surrounded by the entire perimeter of all the points of contact. In case of a standing person with both feet in

contact with the ground, the BoS thus comprises the area of the feet and is delimitated by the line connecting the forefeet and the line connecting the heels. It can be related to the step width during double support phase when the center of gravity is within the BoS. Although in the majority of the gait cycle, the BoS is only the area of the single supporting foot.

During the gait cycle the single foot passes from a complete adhesion with the ground to the oscillation in the air, so it is clear that the BoS dynamically changes. In [7] the different bases of support are defined according to the gait phases. During single limb support, the boundaries of the BoS are defined by the supporting foot width and foot length. When the stance foot begins to touch the ground, a new point of contact occurs. Thus the heel is the limit for the posterior boundary, while the anterior boundary varies with the progression of the foot movement towards the ground. The portion not anymore in the air decreases until the anterior boundary becomes the distal toes' end. In a laboratory where the stereophotogrammetry is available, precise points of the feet and lower limb can be observed attaching markers on them. In the evaluation of the size changes of BoS, it is useful to study the actual position of feet through a metatarsal–phalangeal marker and a heel marker. The medial and lateral boundaries can be defined thanks to the measured ankle and foot widths respectively at the location of the ankle marker and metatarsal–phalangeal joint marker. During double limb support, the BoS was defined similarly to single limb support, but the areas of the feet in contact with the ground are included as the area within them. Considering the gait phases: at heel strike, only the posterior boundary of the contacting limb has to be considered; at foot flat, the entire foot is included in the BoS; at heel off, the metatarsal–phalangeal joint becomes the posterior boundary; at toe off, the swing limb does not touch the ground, thus the BoS consists of the contralateral limb's foot, which was in single limb support. The Figure 1.3 summarises the definition of BoS during gait cycle.

Figure 1.3: *The base of support throughout the gait cycle, respectively at heel strike, foot flat, toe off and heel strike instants. The dark regions of the feet and the dashed lines represent the feet portions of contact and the perimeter of the base of support, [7].*

We can conclude that an univocal and unambiguous definition of what BoS means in this thesis is necessary. In this study, BoS is defined as the area surrounded by both feet in a double support phase (Figure 1.4).

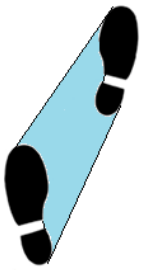

Figure 1.4: *Schematic representation of a BoS in a double support phase. The area comprises both feet (black) and the area between them (light blue).*

The definition of BoS implies a correlation between its numerical estimation and the level of balance of the subject. In fact, a clear example of a strategy to increase stability is to broaden the BoS. The excessive variability of spatio-temporal parameters such as the BoS or the stride length (distance between two contacts on the ground of the same foot) or the step width (distance between feet when they are both in contact with the ground) can be associated to the severity of movement disorders, gait instability and risk of falling [6]. Despite more common gait parameters, the BoS is rarely investigated in literature to asses gait alterations, since it is necessary a correlation of the two feet in space in order to calculate it. This study aims at stating a method to evaluate the BoS exploiting an innovative instrumental system and experimental setup.

Studying the balance of the gait is of primary importance in determining the state of movement diseases and forecasting the risk of fall. Even if during gait we are continuously in a state of imbalance, each subsequent step is aimed at preventing the fall and balance is maintained through interactions between center of gravity and BoS. Studies on the comparison between elder and younger people's gait highlighted that elder's ones show decreased time of contact and wider BoS [7]. This demonstrates that there is a direct correlation between the BoS and the stride width with the gait instability and thus the fall frequency. Hence, determining the size of the dynamic BoS during gait can be clinically relevant in the evaluation of the unsteady gait. The instant in which the BoS size is more significant is the one in which the instability is higher during the gait cycle and for this reason the BoS is commonly relevant in particular during at swing-foot contact [8] [9].

In most studies on locomotion stability, the evaluation of balance involves recordings from force-plate and a camera for motion capture systems to calculate the center of pressure shift, the center of gravity kinematics and the BoS [10]. The BoS is generally computed by force-plates [11] [12] [13] [14] [15] [16] and the center of gravity and the center of pressure traces and velocities by a camera motion analysis system [7]. Parallelly, there is another method to extract the BoS which consists of wearable sensors that enable to measure the inter-feet distance. An example is provided by the combination of magneto-inertial sensors and distance sensors, such as ultrasound sensors [17] or infrared-based technologies [18] [19] [45] to evaluate the stride and step length and step width.

Yiou *et al.* in 2006 [10] used cameras for motion capture system and force plates to obtain the centre of pressure (CoP) shift, the center of mass (CoM) kinematics and the base of support size, since the goal of that study was to analyse the BoS during gait initiation and the CoP traces on 19 healthy participants. Gait initiation is a transitory part between stationary standing and walking and it is an interesting gait phase in which balance could be observed. They found out

that the force plate method was accurate enough in the BoS estimation and consider the BoS estimation 'breaking it down' in step length and step width estimation. The step length was defined as the distance covered by the heel marker of the swing leg from the initial posture to heel contact, while the step width was considered as the mediolateral distance between swing heel marker at heel contact and the position of the stance heel marker at the same instant. Therefore, the BoS is not calculate directly but with the combination of two gait parameters, that can be evaluated with methods well implemented in literature.

Caderby *et al.* in 2014 [8] investigated the influence of gait speed on the mediolateral dynamic stability during gait initiation on 13 healthy subjects, analysing the CoP and CoM displacements and the duration of anticipatory postural adjustments (APA). Anticipatory postural adjustments are all the centrally-initiated dynamic phenomena that anticipate the onset of voluntary movements aiming at increasing stability. APA are manifested as CoP shifts towards the leg in swing phase that shifts also the CoM towards the stance-leg side. The experimental setup can be seen in Figure 1.5.

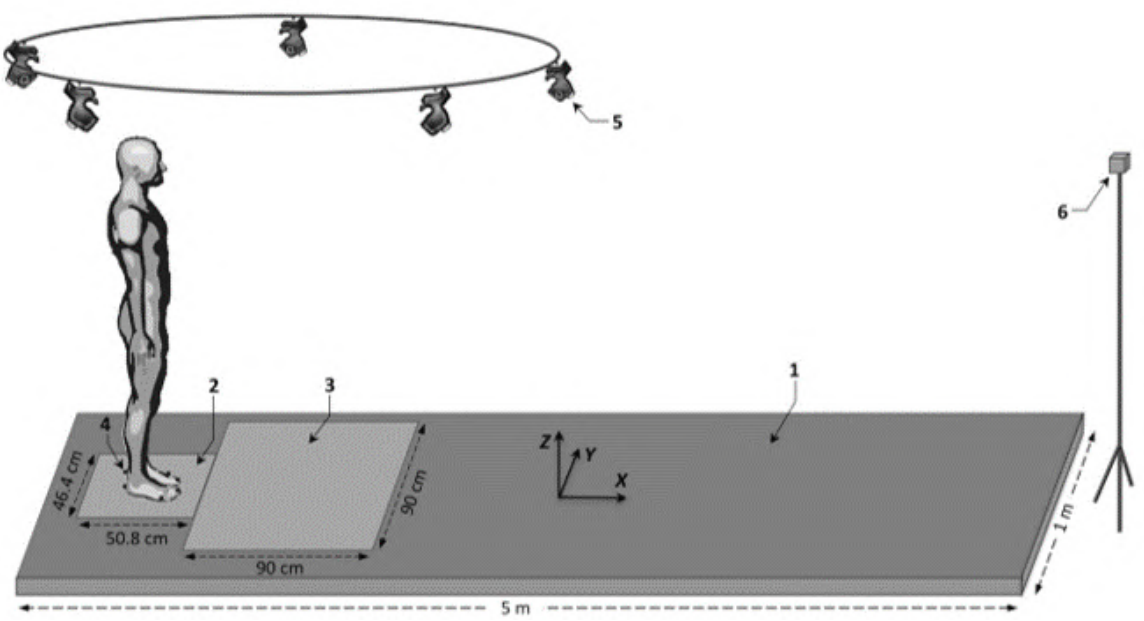

Figure 1.5: *Schematic illustration of Caderby et al [8] experimental set-up: 1) walkway, 2) and 3) force plates, 4) reflective marker, 5) Vicon camera, 6) visual target.*

Arvin *et al.* in 2016 [11] examined the effect of narrowing step width on mediolateral CoM kinematics and the relative margin of stability (MoS) in 14 healthy subjects. The hardware choices fell on an inertia sensor attached at the level of the lumbar spine and the force sensors in the treadmill, on which the participants had to walk, for the detection of the foot placement. The conclusions highlighted that the narrowing step width on older adults leads to less robust gait, given the founded effects on MoS.

If we want to estimate the BoS using only wearable sensors, MIMU data are not sufficient and must be integrated with the inter-feet distance (IFD). Weenk *et al.* in 2015 [17] developed an extended Kalman filter, fusing the inertial sensors data to the ultrasound data (Figure 1.6). This enables to merge the inertial-based information about acceleration and orientation to the relative foot distances. Thanks to this filter, several gait parameters can be estimated, among which the step length and step width. The study evaluated and compared to the optical reference step lengths and widths from 54 trials of 3 healthy subjects. The results, mean ($\pm$ standard

deviation), showed that the absolute difference was 1.7 cm (± 1.8 cm) for the step length and 1.2 cm (± 1.2 cm) for the stride width. Also the walking around in a square and walking with a turn were investigated and the results consisted of absolute differences of 1.7 cm (± 2.0 cm) and 1.5 cm (± 1.5 cm) for step lengths and stride widths respectively.

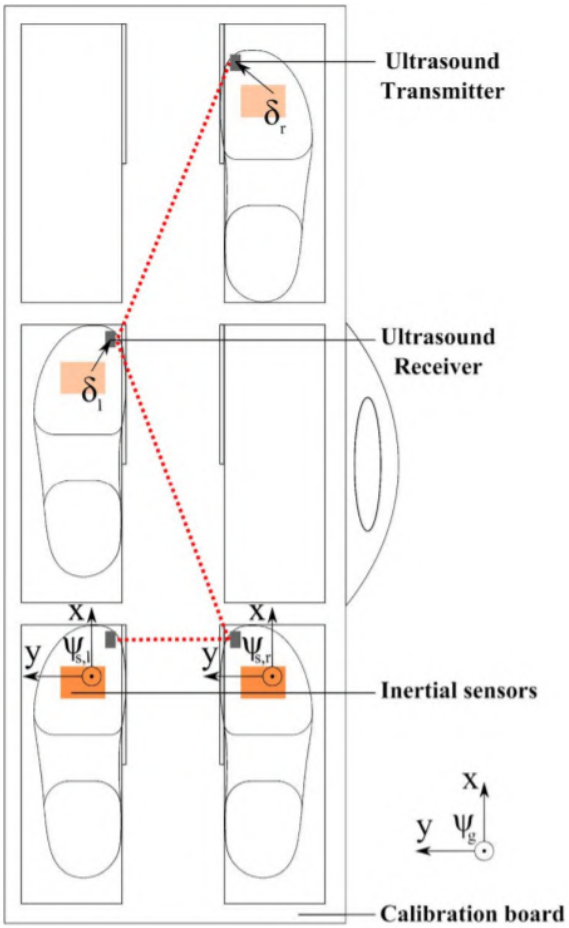

Figure 1.6: *Schematic drawing of shoes on the ultrasound calibration board, Week et al, 2015 [17]. On each foot there are an inertial sensor and an ultrasound transducer. Dashed lines indicate lines of sight between ultrasound transducers during walking.* ψ_g *indicates the global coordinate frame.* $\psi_{s,l}$ *and* $\psi_{s,r}$ *indicate the shoe coordinate frames. Vectors from inertial sensor to transducer are indicated with* δ_r *and* δ_l*.*

Trojaniello *et al.* in 2014 proposed an experimental setup for the IFD estimation consisting of an IMU and an infrared range sensor (IRR). The IRR-IMU integration showed a mean error of 2.7 mm in the IFD estimates.

The study of Hung *et al.* in 2013 aimed at developing a both feet motion tracking system using an IMU, infrared LEDs and a camera to improve the position estimates of the feet knowing their IFD (Figure 1.7).

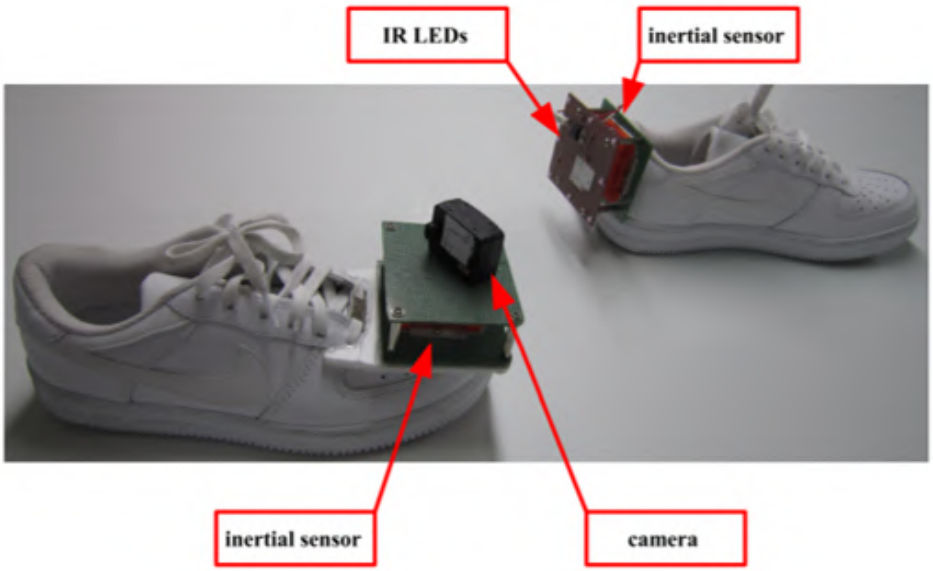

Figure 1.7: *Hung et al. [18] experimental setup to measure the IFD, involving IR LEDs attached on a foot and a camera on the other.*

Bertuletti *et al.* in 2017 [6] proposed a feasibility study for the use of the infrared time-of-flight (IR ToF) sensors for the estimation of the inter-feet distance (IFD) during gait. The experimental setup integrates a MIMU and a IR ToF sensor attached on the lateral internal side of a foot. In this study, the colors of the surface target, the distance between the IR emitter and the target, the angle of incidence, and the relative velocity between the sensor and the target are analysed to assess if they affect the estimate accuracy or not. The proximity sensors were moved in front of a stationary target and were attached on a pendulum to replicate the human gait. The results showed that these proximity sensors are not sensitive to variations in distance and in the the target colors (except for a decreasing of accuracy with black). Although, their accuracy depends on the variations of the angle of incidence (for angle equal or greater than $\pm 60°$). Again Bertuletti et al in 2019 [45] presented a study where the MIMU and two IR ToF sensors (experimental setup reported in Figure 1.8) were used to estimate the number of steps.

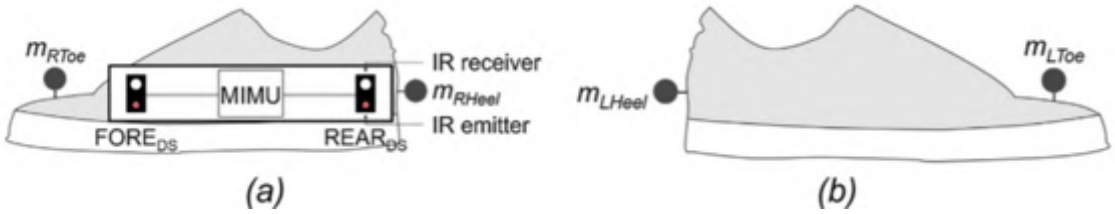

Figure 1.8: *Schematic representation of the experimental setup of Bertuletti et al [45] study. The toe and heel markers were necessary for the comparison with SP. a) Right foot, b) Left foot. Taken from [45].*

In literature the presence of infrared distance sensors for gait analysis is mainly confined to the improvement of orientation and displacement estimation through a redundant system which consists of MIMU and infrared distance sensors. The latter have the purpose to provide the foot clearence during the gait cycle [20] [21] [22]. In Figure 1.9 the sensor configurations of these three studies are reported.

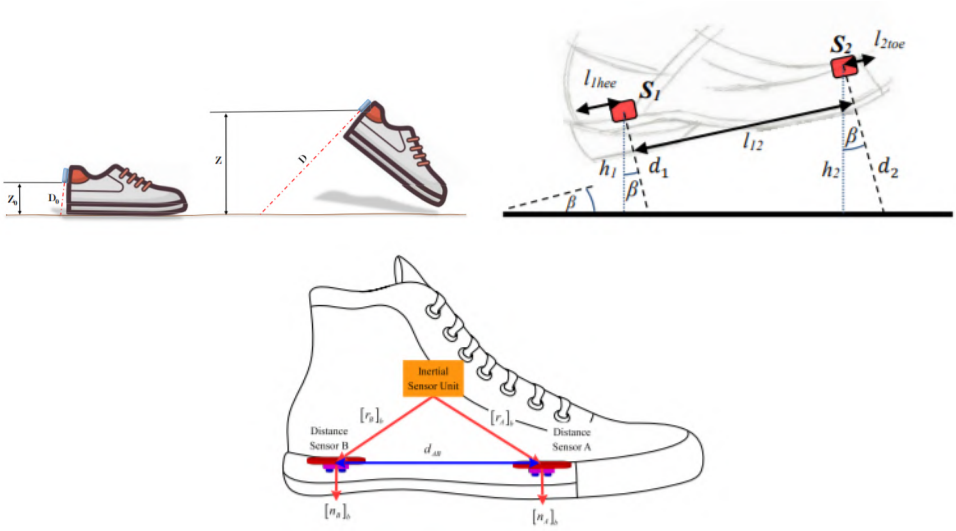

Figure 1.9: *Schematic drawing of shoes instrumented with infrared distance sensors for the foot clearance estimation, from top left: [20], [21], [22].*

In conclusion, in literature the estimation of BoS with wearable sensors is definitely rare. The presence of BoS in literature is more related to considerations on the position of the center of pressure and to its limits than to a final parameter that can bring alone helpful and quantitative information about the gait stability of the patient. This is due to the fact that the IFD is a necessary information and it is not always available. Indeed, the IFD can be achieved only with instrumentations enabling to position both feet in the same reference system: stereophotogrammetry and force plates. Thus BoS estimation is done nowadays predominantly in laboratory. This study targets a new method based on only wearable sensors to enable the BoS estimation out of the laboratories and its final aim is to provide estimates accurate enough to be a quantitative clinical parameter of primary relevance in equilibrium balance.

Chapter 2

Outline of the research project

The goal of this thesis is to devise and develop innovative methods based on the use of wearable sensors for enriching traditional gait spatio-temporal parameters with additional information related to the step width and base of Support (BoS) during walking. In the current state of the art, the estimation of spatial parameters involving the knowledge of the relative feet position and orientation is performed in the human motion analysis laboratory by means of optoelectronic stereophotogrammetric system (SP) and force plates [8] [10]. In this regard, the present research aims at providing and validating tools and algorithms which can enable to perform gait analysis out of the laboratory and in more ecological conditions. It is well renowned that magneto-inertial sensing represents the most promising technology for out-of-lab gait analysis. Miniaturized magneto-inertial measurement units (MIMUs) allow for the realization of low cost and light system thus allowing to collect data for extended period of time.
However, one of the major limitation intrinsic to the use of this technology is that it is not possible to define a common reference coordinate system for describing the relative position between the feet, unless imposing specific initial conditions, since data recorded by each MIMU are self-referenced. It is worthwhile noting that the MIMU can provide the orientation of a rigid body on which it is attached with respect to a global coordinate system without knowing the position of its origin [5]. It follows that, by attaching a MIMU on each foot, it is possible to estimate the relative orientation of both feet with respect to the same global reference, but it is not possible to collect any information about the position of the feet in the 3D space.
When the goal is limited to the analysis of traditional spatio-temporal gait parameters, such as stride length and duration, then it is sufficient to estimate the orientation and displacement of a single foot. For example, the stride length can be obtained knowing the difference of the positions of a foot at the beginning and at the end of a gait cycle. However, this information is not sufficient for describing either the inter-foot-distance (IFD) or the BoS, which requires both the estimation of stride length and IFD.
A possible solution to overcome this limitation is to use wearable sensors that integrate magneto-inertial technology with distance sensors (DS) [17] [19] [18]. In the framework of the present thesis, the focus was set on the use of infrared time-of-flight (IR ToF) sensors for the distance measurements. Among the different technologies available for distance-related measurements, IR ToF technology was chosen as it guarantees the following advantages with respect to the US distance sensors and the camera-based solutions with IR LEDs [6]: 1) a higher output data rates with respect to ultrasound (US) sensors; 2) transmitter and receiver are embedded in the same sensor; 3) stable performances changing the environmental conditions; 4) light weight and small size.
The fusion of MIMU and IR ToF sensors is an innovative and very recent instrumentation setup for gait analysis. Indeed, in literature IR ToF sensors have been exploited in gait analysis exclusively for the foot clearance estimation [20] [21] [22], but not for the purpose of expressing

the absolute positions and orientation of both feet in the same coordinate system.
For the present research it was opted for a minimal invasive experimental set-up by instrumenting only one foot with a MIMU and two distance sensors both attached on the lateral internal side. The position of the non-instrumented foot can be found based on the original methods, developed and presented in the present study, which allow for a low-resolution 'scanning' by means of the IR ToF when the feet face each other.

It is evident that the estimates of the orientation and position are critical points for this study since their accuracy heavily influences the BoS estimate. For the orientation estimation it was selected and implemented a complementary, quaternion-based sensor fusion filter. The latter filter has specific features which guarantee for low computational cost, absence of singularity problem (such as gimbal lock) and tuning of few parameters. The sensor fusion algorithm on which the implemented filter is mainly based is the Madgwick's one [36] because it has just one adjustable parameter. The filter was optimized for the specific goals of the research and some expedients were adopted to improve its performances in the application of the BoS estimation. The complete explanation of the implemented sensor fusion filter can be found in Chapter 9. Specific experiments were conducted to characterize and optimize the algorithm and tune the parameter. The validation of the accuracy of the method to provide the orientation is tested moving a MIMU along a straight path and checking if the found Euler angles were constant during the recording. The results of these experiments are reported in Chapter 12.
As previously mentioned, beside the orientation of the instrumented foot, also its position must be known. Double integrating the accelerations provided by MIMU, the displacement of the foot was calculated with respect to its first instant position. However, the integration suffers from a time-dependant drift that leads to overestimate the displacement causing unacceptable errors. To contain this drift some methods can be implemented:

- Acceleration filtering;
- Reduction of the integration interval to a gait cycle;
- Implementation of the Zero Velocity Update (ZUPT): the cyclical nature of gait is exploited to set to zero the velocity when the foot is in the flat-foot phase;
- Weighted and reverse integration. The final displacement estimation is obtained by a weighted sum of the direct integration and the integration reverse in time, imposing the null-velocity as initial and final condition. This method is based on the Direct and Reverse Integration (DRI) proposed by [51].

Methods implementing the detection of the integration instants, the filter acceleration, the ZUPT detector and the reverse integration are discussed in detail in Chapter 10. Specific experiments were performed to evaluate the accuracy of the proposed entire method for the position estimation. Some tests were done by translating a MIMU along a straight path with known length. The errors and the sensibility to the integration instants variation were reported in Chapter 13.
It is then possible to perform the detection of the non-instrumented foot under reliable estimates of the instrumented foot orientation and position (foot equation of motion). The implemented procedures to obtain the position of sparse points on the contralateral foot surface consist of:

1. acquiring the IR ToF data when the feet face to each other;
2. fitting a linear model on them, approximating the internal lateral side of the detected foot;
3. expressing this model and the instrumented foot in the same coordinate system.

The description of this method is in Chapter 11. The qualitative characterization of the procedure for fitting and modelling the sparse points detected by the IR ToF sensors in 3D space can be found in Chapter 14, which deals with the preliminary investigation done to discover potential issues and limitations of this method.
By implementing sequentially the abovementioned different algorithms and methods, it was then possible to obtain an estimate of the spatial gait parameters. To test and preliminarily validate the methods, an experiment on a healthy subject walking with self-selected velocity was performed in the human motion analysis laboratory using the SP as gold standard. The SP data were processed to express SP and MIMU data in the same coordinate systems. The stride length was estimated from both data and the differences were calculated. The step width was defined by the IFD measured by the distance sensors, thus a method to provide from SP data the distance between the positions of IR ToF sensors and the internal lateral plane of the non-instrumented foot is implemented. Finally, the BoS is geometrically calculated knowing the position of its vertices. The BoS estimate accuracy depends on the accuracy of orientation estimate, stride length and step width. The comparison between the BoS found from MIMU data and SP data highlights an error in the positioning of the non-instrumented foot model. To improve the estimate, the IR wave from distance sensors is not considered definitely perpendicular to the detected surface but the angle of the view cone of the IR ToF sensors is considered to rotate the directions of the distance vectors. All the results about the spatial gait parameters are reported in Chapter 15.

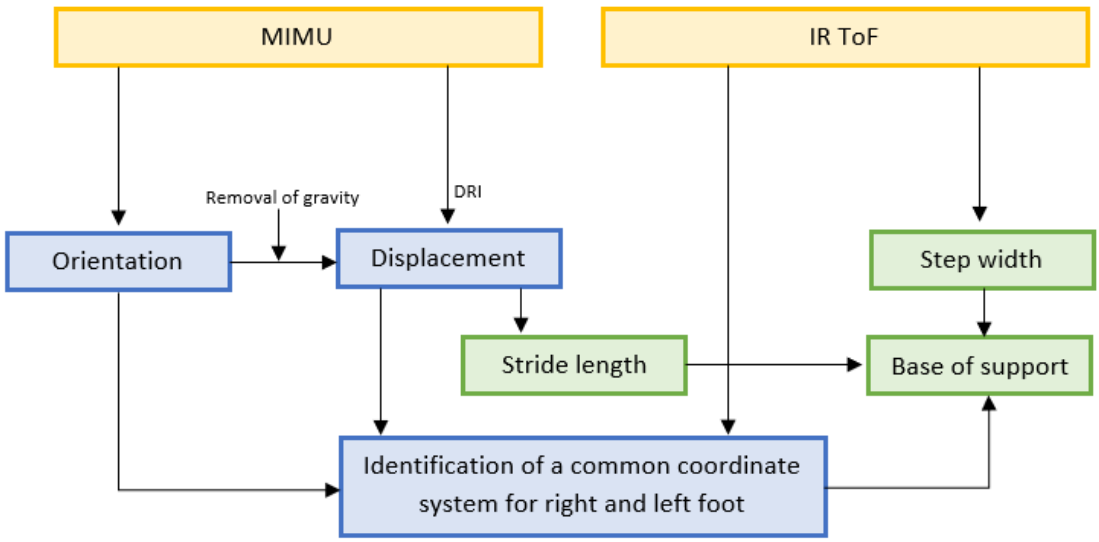

Figure 2.1: *Block diagram showing the used sensor data (yellow) and all the methods (blue) that have to be implememted to estimate the spatial gait parameters (green).*

Part I

Introduction

Chapter 3

Introduction to gait analysis

3.1 Gait cycle

To analyse and subsequently quantify how a subject walks, it is important to define the shortest part of gait that repeats itself: the gait cycle. According to this statement, the gait cycle is the functional unit of gait analysis and can be defined from any event of a foot to the subsequent same event of the same foot, for example as the period between two successive touches of the same foot on the ground. The most diffused choice is to take the heel strike as the reference event. The spatio-temporal parameters exploit the gait repeatability, in fact they are related to the phases of the gait cycle, and thus the understanding of the gait cycle phases is crucial.

The main distinct phases which alternate for each lower limb are stance and swing:

- stance phase or support of the analysed foot, thus consists of the entire period of time that the foot is in contact with the ground;
- swing phase or transfer, in which the foot prepares for a new support and the weight is transferred to the other, thus consists of the period of time in which the foot is in the air.

The stance phase occupies 60% of the cycle in normal walking, while it shortens up to 37% in running. The complementary portion of gait cycle is occupied by the swing phase.

The simultaneous observation of both lower limbs enables to introduce further segmentation of gait cycle. First of all a distinction can be done between double support or bipedal support, when both feet are considered in stance phase, and single support or unipedal support, when one foot is in contact with the ground and the other is in an oscillating phase. Figure 3.1 illustrates all the different gait phases which compose stance and swing. They are reported below with the corresponding gait cycle percentage, based on [25] and [26].

Stance (from 0 to 62% of the gait cycle) is made up of:

- Weight acceptance (0-12%): phase which aims at stabilising the limb. This phase can be further broken down into:
  - Initial contact (first 3% of the gait cycle): the heel touches the ground and starts the rotation to foot flat.
  - Loading response (3- 12%): after the heel strike event, the foot falls flat on the ground (foot flat event), the knee extents progressively to absorb the shock until the whole foot is on the ground, the hip flexes and the ankle is in dorsiflexion. Thus this phase is

characterised by the rapid weight load to the considered limb and is a double support phase.

- Single limb support (12-50%): phase in which the body progresses over the foot. It is divided into:
  - Mid stance (12-31%): the shank of the supporting limb rotates forward, the hip and the knee extent while the ankle is dorsiflexed. Since the opposite limb is in seeing phase, the subject body is moved forward. This phase of completely single support ends with the heel off event, when the heel stops to touch the ground. The feet face each other.
  - Terminal stance (31-50%): the center of mass progresses while the forefoot is used as 'push point', the knee increases its extension and subsequently begins a flexion. This phase ends with the opposite foot's heel strike.
  - Pre-Swing (50-62%): the flexion of the knee and the ankle increase while the extension of the hip decreases. It is the translation phase between stance and the subsequent swing. The foot is pushed and lifted off of the floor, thus the event that defines the end of this phase is the toe-off. Now the stance ends and the swing starts.

Swing (from 62 to 100% of the gait cycle) is composed by 4 sub-phases:

- Initial swing (62-75%): the leg has to prepare the advancement of the limb, so this phase is characterised by the flexion of the hip, the knee, and the ankle (which is slightly dorsiflexed). The foot clearance over the ground starts, since the foot is no longer in contact with the floor.
- Mid-Swing (75-87%): this phase shows the dorsiflexion of the ankle, the extension of the knee, the flexion of the hip, the advancement of the swinging limb beyond the line of the body gravity, and the thigh reaches its maximum advancement point. The feet face each other.
- Terminal Swing (87-100%): the swinging limb decelerates till the advancement ends. As for the joint status, the ankle is in dorsiflexion, the knee is extended and the hip is flexed. The muscles prepare themselves to the oncoming heel strike event, which states the end of the gait cycle. The foot is positioned to re-make an initial contact and start a new cycle.

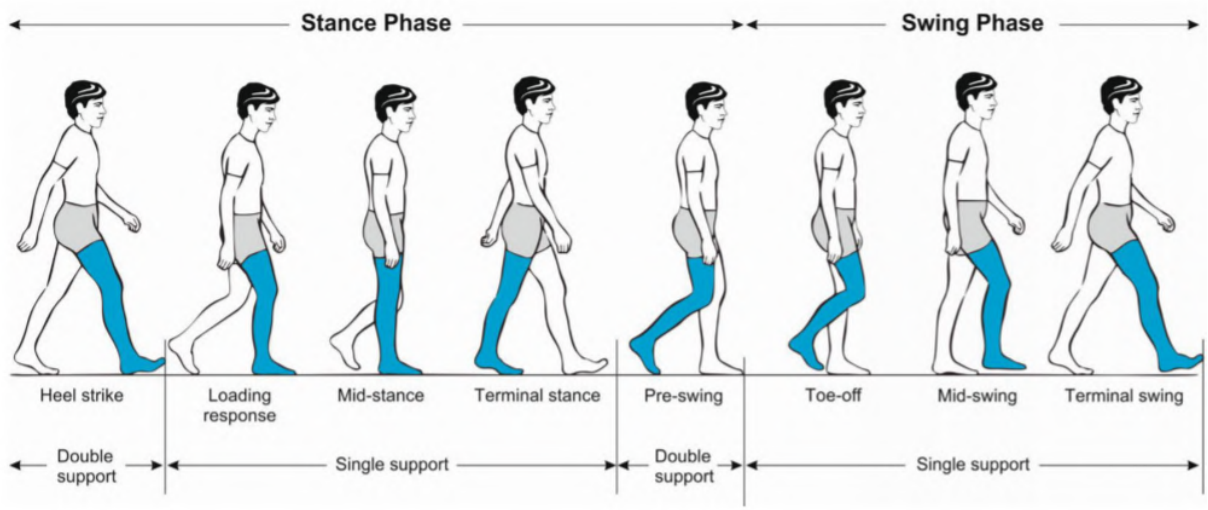

Figure 3.1: *Schematic representatrion of the main phases of the gait cycle (a stride), from [31].*

.

Figure 3.2: *Illustration of the foot positions in different instants of the gait cycle, adapted from www.chiroeco.com/gait-cycle.*

3.2 Definition of the principal spatio-temporal gait parameters

Once described the gait cycle and all its phases, we can proceed to deal with the gait parameters that can be extracted by the proper instrumentation and have a clinical relevance.

A stride is the sequence of events between a foot contact with the ground and the next contact of the same foot. Stride time is considered as the interval between those two events, so two following contacts with the ground of the same chosen point of the same foot, generally the heel. Although the centre of the heel is the most used point, since for some pathological situations it not appropriate, other studies have chosen instead the centers of mass of the feet [27], ankle joint centers [28], external borders of the feet [29]. Left and right strides are independent and a stride of one side overlaps with the preceding and subsequent strides of the opposite foot.

A step is the sequence of events between a foot contact and the next contact of the opposite foot. Step time is the temporal interval between those two events, so two following touches with the ground of the same point of one foot and the opposite one, generally the heel. Two steps, one for each side, constitute a stride.

The aim of the gait parameters is to be a quantifiable and objective measures through which describe a patient's locomotion state. The gait parameters can be divided into temporal and spatial. A brief outline of the main parameters is reported below.
Spatial (or Distance) Parameters include [30]:

- Stride Length, which is the distance between a point of a foot at its first contact with the ground and the same point on the same foot at the next contact. The direction if the stride length determines the local gait direction of progression;
- Step Length, which is the distance between a point of a foot at its first contact with the ground and the same point on the opposite foot at the next contact along the direction of progression;
- Stride Width, which is the distance, perpendicular to the direction of progression, between a point of a foot at its first contact with the ground and the same point on the opposite foot at the next contact. The width depends, thus, on the chosen point of the feet.

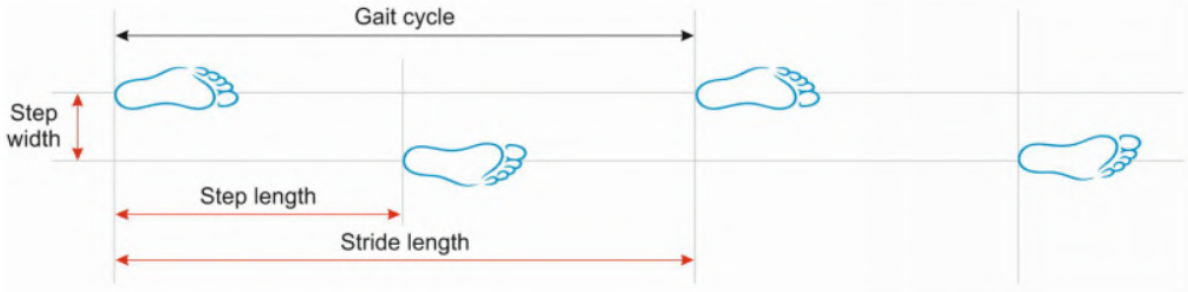

Figure 3.3: *Schematic representation of the spatial gait paramteres, [31].*

Temporal Parameters include [2]:

- Cadence, the number of steps per unit time;
- Speed, the distance covered by the subject per unit time;
- Stride Time, the duration of the stride;
- Step Time, the duration of the step;
- Stance Time, the duration of the stance phase;
- Swing Time, the duration of the swing phase;
- Single Limb Support, amount of time spent with only a foot on the ground expressed as percentage of the gait cycle.

The gait events (GE) are instants during gait cycle with particular importance, since they mark the end and the beginning of most of the gait cycle phases. The most relevant are the following [32] and are illustrated in Fig 3.4:

- Initial contact or Heel Strike: the heel touches the ground and the stance phase starts;
- Foot Flat: the foot is completely in contact with the floor;

- Heel-off: the foot starts to separate itself from the ground;
- Final contact or Toe-Off: the foot is no more in contact with the ground and the swing phase starts;
- Mid-swing: half of the swing phase, detected as the instant in which the foot reaches the maximum angular velocity.

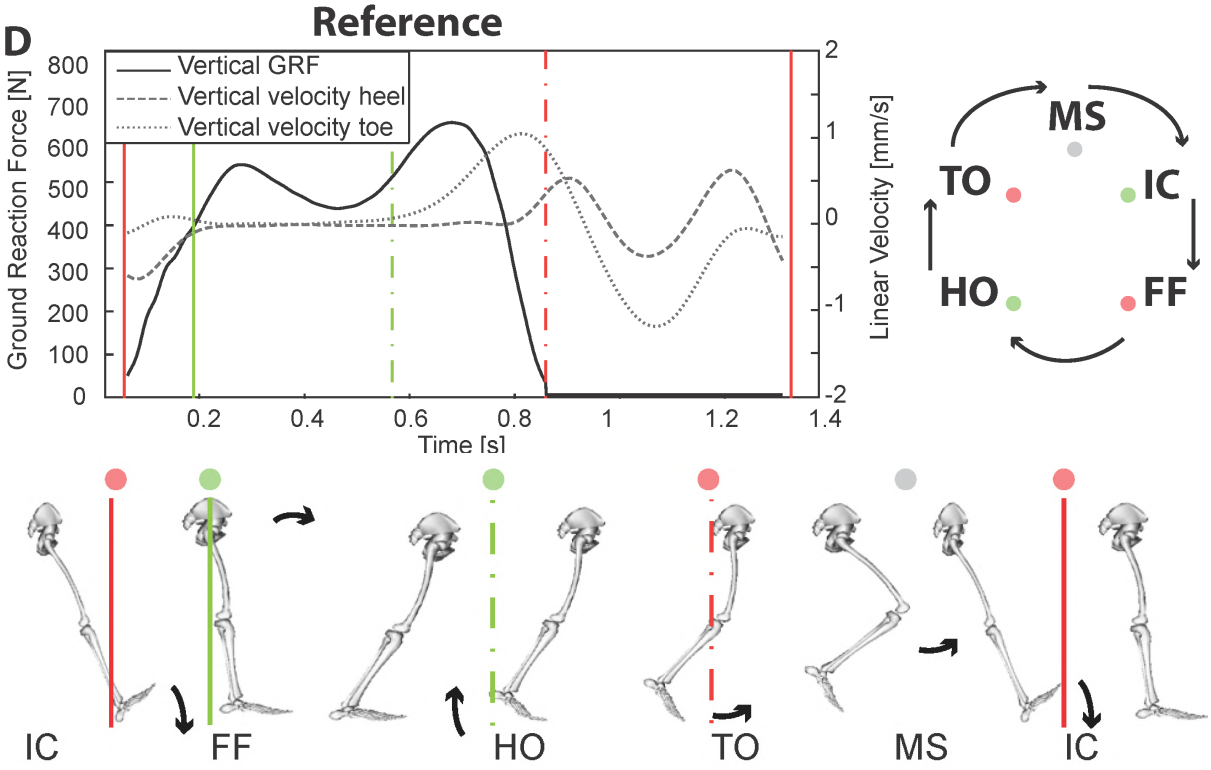

Figure 3.4: *Schematic representation of the GE, from [32].*

Chapter 4

Gait analysis instrumentation

The study of the biomechanics of the human motion, which is the main interest of the gait analysis, can be done with different methods and instrumentations. Goal of human movement analysis is to gather quantitative evaluation about the execution of a motor task. During the last decades, gait analysis have significantly developed and thus, hand in hand with it, also the hardware technologies has evolved.

Among this huge variety of methods, motion capture systems can be divided into optical and non-optical systems. The former are commonly considered as the gold standard of gait analysis. The optical systems use optical cameras, while non-optical systems include a large variety of instrumentations, in general based on inertial, electromagnetic, electromechanical or acoustic principles.

Another fundamental distinction in the existing methods to evaluate the human motion is between non-wearable and wearable sensors.

The former are the previously cited optical system, image processing, floor sensors, such as force plates. To better understand the image processing, the unique marker less systems are in general based on computer vision algorithms and start from image segmentation. Instead, the wearable sensors includes [4]: accelerometers, gyroscopes, magnetometers, force sensors, extensometers, goniometers, active markers, electromyography.

The optical system of the stereophotogrammetry (SP) and the Magneto-Inertial Measurement Unit (MIMU) are described in details below, since they are the instrumentation used in this work thesis, the former for the validation and the latter for the implementation of the proposed method.

4.1 Optoelectronic stereophotogrammetry

In laboratory the optoelectronic stereophotogrammetry is one of the most frequently used motion capture systems, especially when the focus of the gait analysis study is related to the position or the orientation. An example cab be seen in Fig. 4.1. With this system, we are able to capture the movement of whole-body center of mass, the joint kinematics and the relative movements between adjacent bones [33]. Another relevant point is that the SP enables realistic reconstructions and representations of the musculoskeletal system during a certain motion task gathering virtual reality.

The principles which SP system exploits to capture human motion is tracking the trajectories of spherical retroreflective markers attached to the body part of interest. How SP reaches this goal is explained in details below.

1. SP system enables the acquisition of 2D images thanks to cameras, which have to be

calibrated before their use. This leads to bi-dimensionally position the makers in image planes, thanks to some techniques of image processing which may involve, for example, linear thresholding. To enable the 3D reconstruction, the number of camera can vary from a minimum of 2 up to a maximum commonly of 50.

2. After the 2D acquisition of images, then the 3D reconstruction must be done to put all the markers in the same common coordinate frame. With the definition of the global coordinate system also the local reference frames can be estimated for any of the body segment of interest.

3. To obtain quantities of interest to analyse, the above information must be related with a human model. Then the known outputs become the trajectories of the markers, which stand for specific part of the body. Successively, also other quantities can be achieved such as joint kinematics, velocities, acceleration and so on.

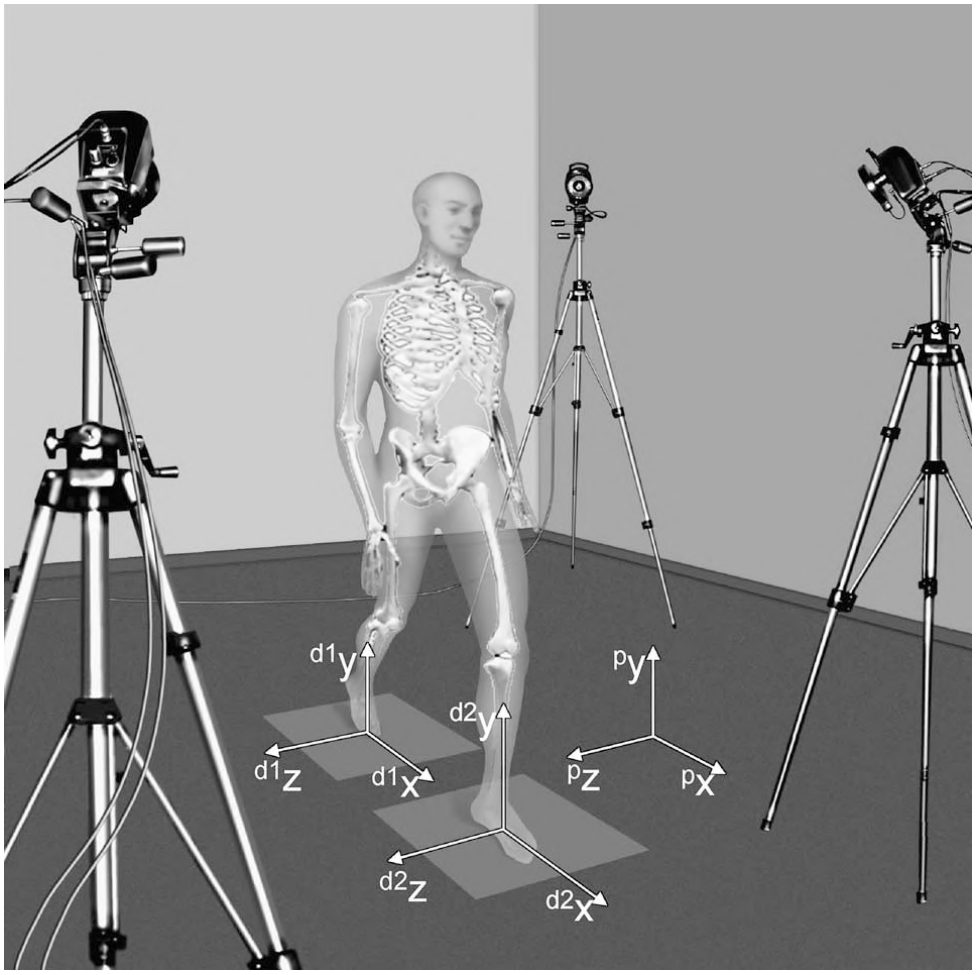

Figure 4.1: *Typical instrumentation of a human movement analysis laboratory with stereophotogrammetry system and force plates om the floor, [33].*

Vicon system is one of the most common SP system and it is the one used in this thesis validation process. This system is an optical passive system, which means that the spherical balls of the markers are covered with a retroreflective coating so that they reflect IR light. The IR light is emitted by the sources mounted on the cameras so that the light has to cover the path between the camera and the marker twice to be detected. The advantage to use the

IR light is the reduction of the artefacts produced by the natural light since the cross-talk is decreased. This is possible thanks to a IR pass filter placed on the camera lens [34]. In Fig. 4.2 an illustration of what is reconstructed with Vicon system can be seen.

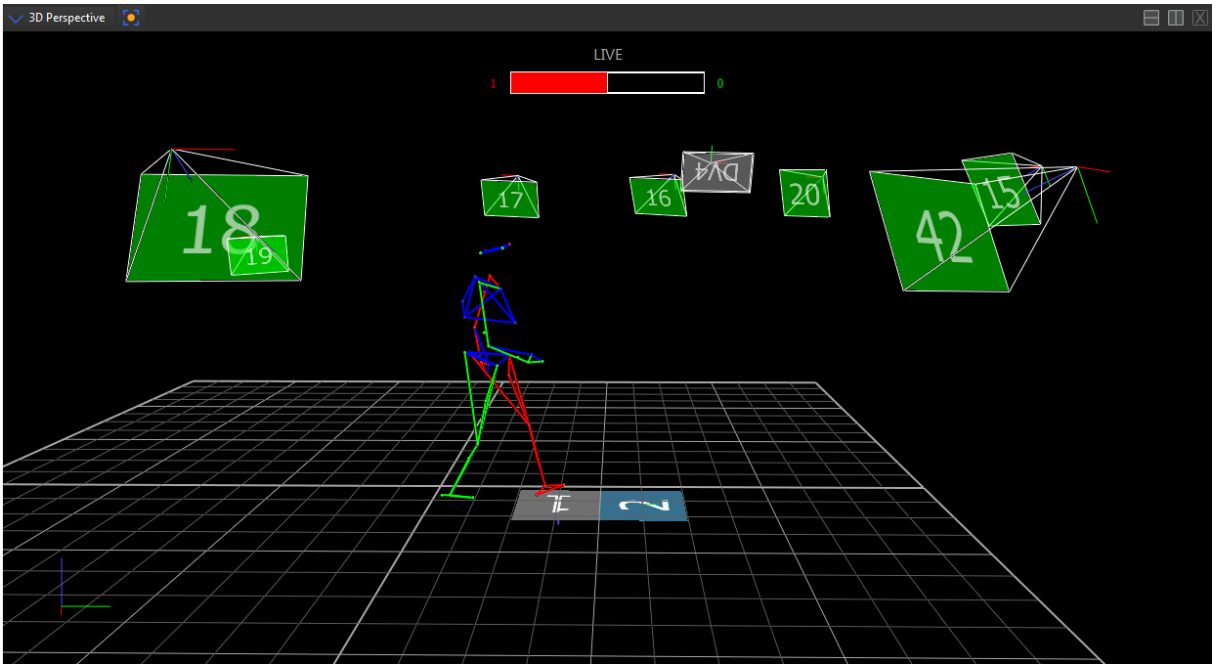

Figure 4.2: *Example of the vision of the acquisition volume with Vicon: the body segments are highlated thanks to the links between the desired markers. Adapted from https://docs.vicon.com/display/Nexus25/Automatically+assess+foot+strikes*

Other types of SP use, instead, active markers which are not reflective of light coming from a distinct source but directly 'light up'. They consist of IR LEDs and only one at time is activated. In this way it is easier to follow the marker on the image. Since the source of the IR light is in the marker itself, the light must just cover once the path between the camera and the marker and this enables to enlarge the volume of acquisition with respect to the passive type. The main disadvantage of the active markers is that they require an embedded power supply. Optotrack is an example of SP system which uses active markers.

In conclusion, the stereophotogrammetry is widely accepted as the gold standard in gait analysis due to its robust performance in the reconstruction of the trajectories of body segments. However, it has some drawbacks:

- it is expensive, time consuming for the calibration of the cameras and the subject preparation, and requires the presence of an expert to be used,
- it suffers from trajectory gaps when the light path is interrupted by an obstacle during the movement and the cameras do not receive it;
- the gait analysis can be carried out exclusively in a laboratory, so in a confined volume for a defined period of time, excluding a prolonged monitor of the patient over his/her daily activities.

4.2 Magneto-Inertial Measurement Units

The accurate estimation of the orientation of a rigid body, relative to an inertial frame, is required for a wide range of applications, such as navigation, robotics and motion analysis. The recent development of Micro Electro Mechanical Systems (MEMS) has allowed smaller and cheaper inertial sensors to be adopted in many different fields and even in the daily use, being in mobile devices like smartphones and tablets. In motion analysis, they have the great advantages over the optical tracking system:

- no need for specialised laboratories, expert technician and marker placements, so that inertial sensors can guarantee the usage in unconfined evaluation spaces for long periods;
- lack of need of high-costed instrumentation;
- high portability, self-power, possibility of wireless communication;
- they are self-contained, so that they do no need external sources of any type and can process data on board thanks to an embedded microcontroller.

The MIMUs are composed by orthogonally mounted tri-axis sensors: a gyroscope which measures the angular rate, an accelerometer which measures the linear and gravity acceleration, a magnetometer which measures the magnetic field in their MIMU coordinate systems. The information derived from the three different types of sensors has to be merged purposefully together to estimate the 3D orientation of the MIMU coordinate systems with respect to a defined global coordinate system. Although, the data provided by MIMUs, in particular if they are low-cost, are affected by high noise levels and time-varying biases. Therefore, a proper sensor-fusion algorithm must be used to merge the data to obtain a bias-free estimation of the orientation, trying to maintain a low computational cost [35].

To better understand the issues brought by MIMUs, it is appropriate to analyse individually the limits of each sensor. The gyroscope is the most bias-affected sensor and every axis has a different and time-varying bias. Furthermore, it is able to identify the difference in angle between the initial and final positions, so its measurement is not absolute but relative. The accelerometer is sensitive to the gravity and also the other accelerations, so it is more reliable, for the purpose of the orientation estimation, in static conditions. The magnetometer is highly affected by the ferromagnetic distortions due to a magnetically non-homogeneous environment.

If only the inertial sensing is considered (IMU), only the accelerometer and the gyroscope are taken into account and, even if the attitude can be estimated with respect to the local direction of the gravity, the heading remains unknown since the accelerometer is not sensitive to the rotation around the gravity axis [36]. Indeed, an additional reference vector is needed to properly estimate the three dimensional orientation, the magnetic field, which is available everywhere (except at the magnetic poles where it would be parallel to the gravity and so it would not add any information). Hence the inertial and magnetic sensing together are thus suitable for providing both attitude and heading directions.

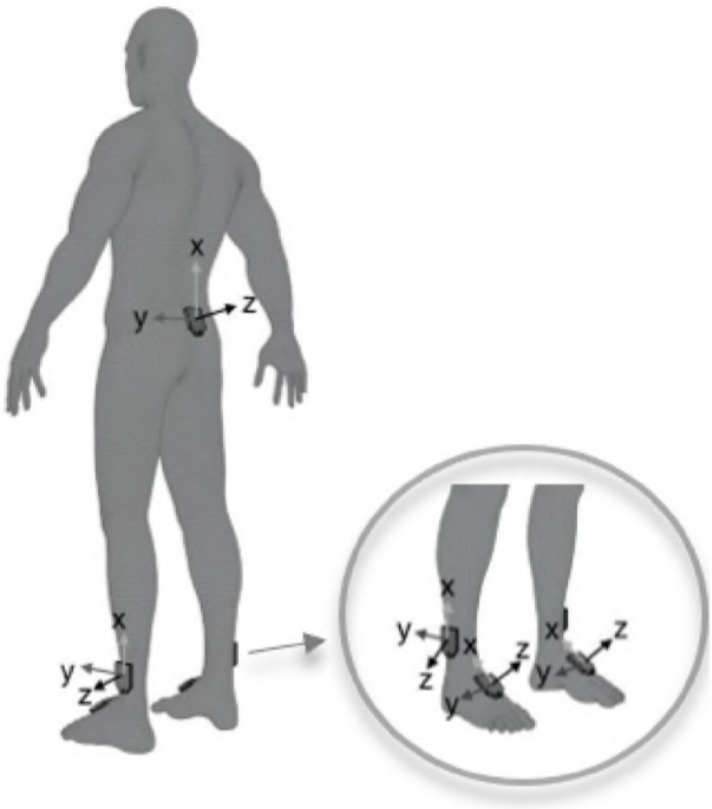

Figure 4.3: *Example of MIMU positioning on body in gait analysis, [37].*

4.2.1 Accelerometer

The accelerometer is a measurement device whose output consist of the proper acceleration, so the acceleration of the body on which is attached with respect to its own instantaneous coordinate frame. Accelerometers can be single or multi axis and detect the magnitude and direction of the acceleration, seen as a vector quantity. The diffusion of these sensors is due to the development of the Micromachined Micro-Electro-Mechanical Systems (MEMS), which enable their increasing presence in very small and portable devices. The power supply is external.

In most accelerometers, the physical principle exploited to measure the acceleration is based on the inertia of a mass subjected to an acceleration. An elastic element suspends a mass and this mass, in case of acceleration, moves from its rest position. The displacement is proportional to the acceleration so that a displacement-sensitive sensor can transforms it into an electrical signal. In fact, if we represent the accelerometer as a mass suspended by a spring (Fig. 4.4) and equalize the forces derived from Hooke's law and the second Newton's law:

$$F = kx \tag{4.1}$$

$$F = ma \tag{4.2}$$

$$kx = ma \tag{4.3}$$

it is clear that knowing the displacement is necessary to detect the acceleration.

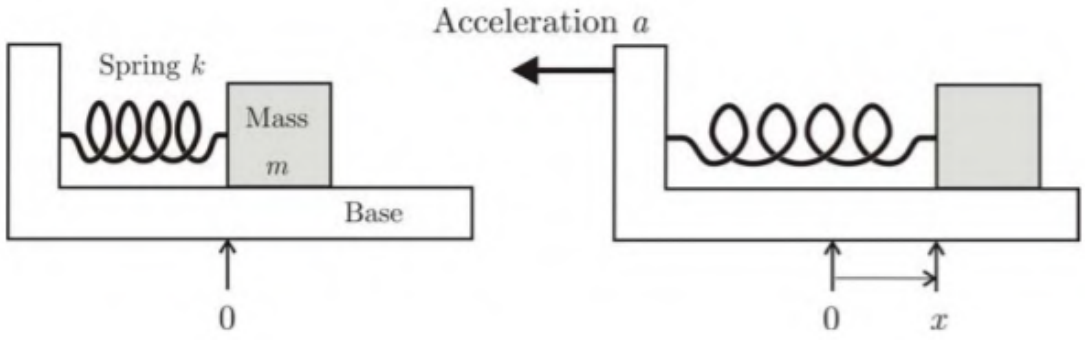

Figure 4.4: *This figure illustrates an approximation of a single axis accelerometer as a system with a mass suspended by a spring. Left: state with no acceleration. Right: state with a certain imposed acceleration. [34]*

Indeed, the functional principle consists in detecting the displacement and accelerometers can be classified according to the functional principle used to measure it.

- The capacitive accelerometer exploits the change of the electrical capacity of a capacitor derived from the change of the distance between its armatures. One of the two armatures consists of the mass and the other one is the fixed structure of the device. A circuit detects the capacitance variation and produces an electrical signal proportional to that change.
- The strain gauge accelerometer exploits the resistance variation of the strain gauges caused by the variation of tits length. The mass is mounted on thin sheets that flex in presence of acceleration causing an elongation of the strain gauges. The latter are connected to a Wheatstone bridge, whose unbalancing voltage is read by a voltmeter since it is proportional to the acceleration.
- The piezoresistive accelerometer has an electrical resistance which varies with the displacement. Accelerometers of this type are similar to the strain gauge type, since the Wheatstone bridge is the same but piezoresistive sensors are used instead of the strain gauges. The mass is suspended on a membrane on which piezoresistive elements are attached. These latter exploit the piezo-resistivity and transduce the mechanical deformation into an electrical signal.
- In piezoelectric accelerometers the mass is suspended on a piezoelectric crystal and, in case of acceleration, the mass compresses the crystal generating an electrical signal.

The most commonly used types in gait analysis are the piezoresistive and capacitance accelerometers [38].

Specifically, accelerometers are sensitive to an acceleration which is sum of the linear body acceleration, a_{body}, and the gravity acceleration, g. The found linear acceleration is projected along the specific sensing axis of the accelerometer, n (Fig.4.5). Thus the output is an acceleration expressed in the MIMU coordinate system and calculated as follows (without taking into account the axes offsets and electrical noise):

$$a_{sum} = a_{body} - g \tag{4.4}$$

$$a = a_{sum} \cdot n \tag{4.5}$$

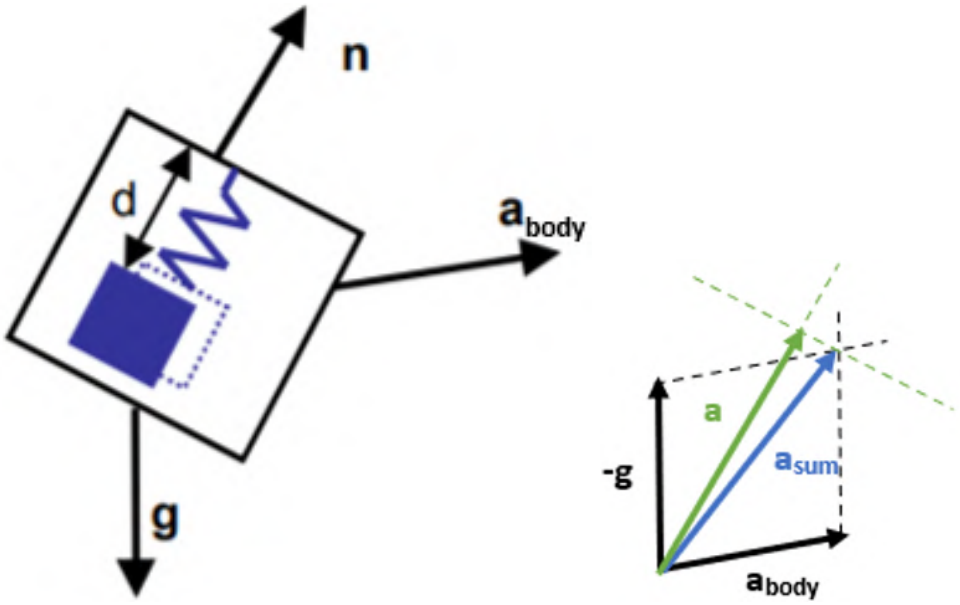

Figure 4.5: *The illustration represents a single axis accelerometer, [39]. The blue square symbolises the mass suspended with a spring, whose stiffness is represented in blue. d is the displacement of the mass, n is the sensing axis of this accelerometer. In the second image, the vectors are drawn: the blue vector is the vectoral sum of $-g$ and a_{body} while the green vector is the output of this accelerometer, the projection of a_{sum} on the sensing axis.*

A triaxial accelerometer can be achieved by mounting three single axis accelerometers together.

The function of accelerometers changes according to the static or dynamic phase in which they lie. In static condition, following the Equation 4.3, a_{body} is null and the only sensed acceleration is the gravity. Thus in the field of the orientation estimation, the useful information that can be obtained is the inclination of the body through trigonometric functions. Actually this is valid for a two-dimensional case, but in 3D, if the gravity axis coincides with one of the three sensing axes, the accelerometer is not sufficient to provide a 3D orientation of the body on which it is attached. This is because the other two sensing axes could not measure anything and all the output information relies on a single axis.
In dynamic condition, both a_{body} and g are present and the output acceleration alone cannot distinguish from them.

4.2.2 Gyroscope

Gyroscopes measure angular velocity around its sensing axis. Traditional gyroscopes are mechanical and consist of a rotating device which maintains fixed its rotating axis exploiting the conservation of angular momentum law [34]. A 3D gyroscope can be described as a wheel mounted in three gimbals, which are the pivoted supports that enable the rotation around three different axes. The fundamental equation describing a rotating rigid system is:

$$M = \frac{dL}{dt} = \frac{d(I\omega)}{dt} = I\alpha \tag{4.6}$$

Where M is the torque vector on the gyroscope, L the angular momentum vector, I the moment of inertia, ω the angular velocity, and α the angular acceleration. If a momentum M is applied perpendicular to the rotation axis, so to L, then a force rises perpendicular to M and L. The

derived motion is the precession and the reaction force induces the gyroscope to rotate around a fixed axis, called spin axis, which does not change its direction even if the support varies its orientation.

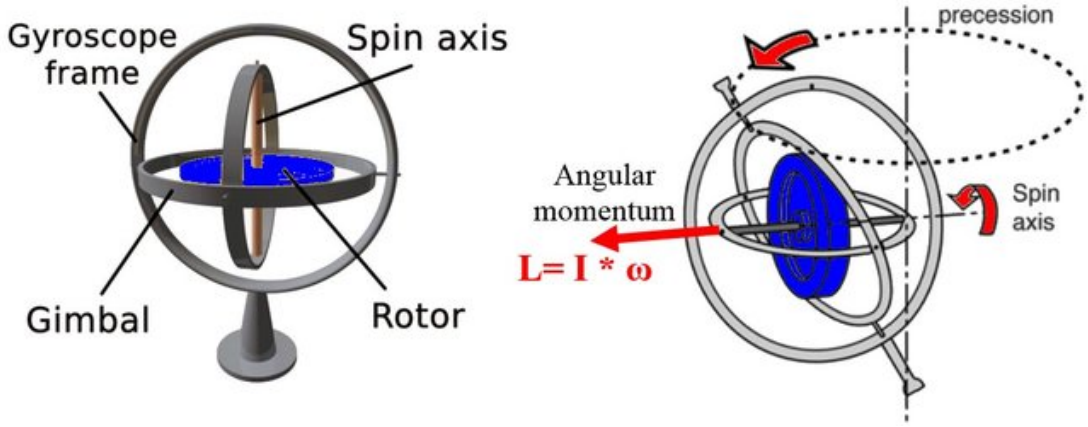

Figure 4.6: *Representation of gimbaled gyroscopes, [40].*

The main categories of gyroscopes are the mechanical and optical one [34]. Within them there are many different types. Laser and gimbaled gyroscopes are not suitable for gait analysis due to their large size and high cost. Thanks to the development of MEMs, miniaturizes gyroscopes can become widespread. They consist of a vibrating element that, if subjected to a rotation, is also affected by a vibration in the orthogonal direction to the original one, according to the Coriolis effect. The Coriolis force is described by this equation:

$$F_{Coriolis} = -2m(\omega \times v) \tag{4.7}$$

where m is the mass, ω the angular velocity of the object, v the velocity of the mass relative to the object motion. For example, if the mass is vibrating along x direction with linear velocity v and if the gyroscope is rotating around the z direction with angular rate ω, thus, according to Coriolis effect, the mass is also subjected to an apparent force causing an the additional vibration along the direction perpendicular to the previous two, y direction. This is represented in Fig. 4.7.

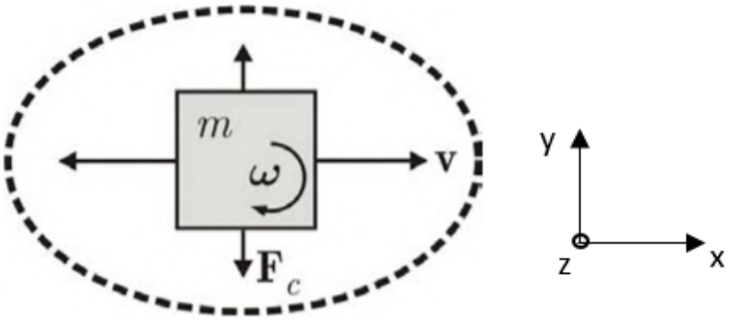

Figure 4.7: *This illustration shows the vibrating mass under the vibration v. The gyroscope rotation induces an additional vibration and so displacement due to the Coriolis force (Fc) perpendicular to the original displacement. Adapted from [34].*

The physical principle exploited to measure the angular rate is similar to the one described for accelerometers. Indeed, thanks to the Coriolis effect, we can read the displacement caused

by the additional vibration, since it is proportional to the magnitude of the angular rate. The transducers have to be sensitive to the displacement and can be based on piezo-resistivity or the change of capacitance.
In the most common configuration of gyroscopes, silicon is etched to construct a pair of tuning fork masses [41], as it shows Figure 4.8 . The masses are stimulated to vibrate by an oscillating electric field.

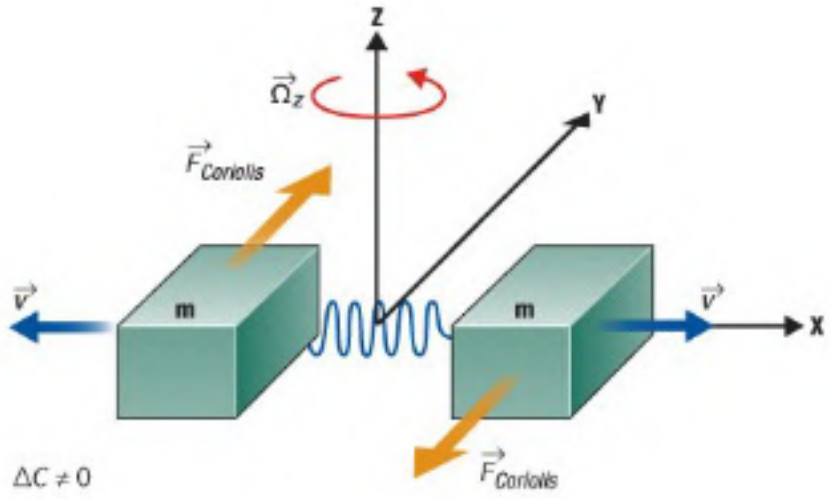

Figure 4.8: *Illustration of a tuning fork configuration gyroscope: a pair of vibrating masses (with linear vibration v) is subjected to an angular rate, so* $F_{Coriolis}$ *rise. It follows a change in the relative position and in the capacitance between the two masses, which can be detected. If the masses move in the same direction, neither change in relative position or capacitance occur. Source: www.analogictips.com/gyroscopes-part-2-optical-and-mems-implementations-faq*

All these considerations are valid for a single axis gyroscope and a triaxial gyroscope is constructed mounting three single axis gyroscope together.

The output of the gyroscope is corrupted, as the one of the accelerometer, by axes offset and electrical noise. It should be highlighted that the biases are not constant in time: they are different in different days and in particular in the first minutes after the power supply is activated the variation of them lead to non-reliable estimates [5]. The reason why the information given by gyroscopes is not sufficient is that they are heavily affected by the biases problem which lead to drift errors.

4.2.3 Magnetometer

The magnetometer is a measuring device that detect the magnetic field. The scalar magnetometers measure the magnitude of the magnetic field, where the vectoral ones measure the direction and the strength of the magnetic field detecting the component along a particular axis. Magnetic field, indeed, is a vector quantity, whose strength is measured in tesla in the SI units, while in gauss in centimetre-gram-second system of units. One tesla corresponds to 10,000 gauss. Using a three axial magnetometer and so knowing the components of the magnetic field in three different and independent directions allows to determine the vector in 3D space. The model of a single axis magnetometer is:

$$h = (h_{earth} + h_{extrernal}) \cdot n \tag{4.8}$$

where n is the sensing axis. In this model, offsets and measurement noise have to be added in real cases.

The most common of the magnetometers is the compass, which points in the direction of the Earth's magnetic north. Magnetometers are largely used in navigation and aircraft's attitude and heading reference system to provide the inclination of the horizontal plane with respect to Earth's magnetic north, so they are used as a heading reference. Furthermore, besides the application in the orientation estimation, magnetometers can be used also as metal detectors. As accelerometers and gyroscopes, the recent development of MEMS leads to increase the spread of such of these devices, decreasing the cost and miniaturising the size.

There are many types of magnetometers which are based on different functional principles. Generally, to obtain the magnetic field vector, a voltage proportional to its strength has to be produced. To do that the Hall effect and the magneto-resistivity are exploited. At the basis of both those principles, there is the Lorentz force which introduces an anisotropic conductive behaviour [42]. The force acting on a single charged carrier is:

$$F = q(E + (v \times B)) \tag{4.9}$$

where F is the Lorentz force, q the charge of the carrier, E the electric field vector, v the velocity of the carrier, and B the magnetic field vector. qE is called electric force (F_e) and $qv \times B$ is called magnetic force (F_m). The application of a magnetic field perpendicular to the current flow induces the deflection of the current flow. It follows that charged particles of opposite sign amass in the opposite edges of the conductor generating a voltage, V_h. Knowing that current I can be expressed as follows:

$$I = j \times A = nqvwd \tag{4.10}$$

$$v = \frac{I}{nqwd} \tag{4.11}$$

where j is the current density, n the number of charged carries, A the cross-section area of the conductor (w is the width and d is the thickness), v the drift velocity. In the equilibrium state:

$$F_m = F_e \tag{4.12}$$

$$qv \times B = \frac{V_h q}{w} \tag{4.13}$$

Considering the previous equations, we can conclude that the voltage caused by the accumulated charges is:

$$V_h = \frac{IB}{nqd} \tag{4.14}$$

Hall effect states that a voltage difference occur on the opposite faces of an electrical conductor due to the application of a magnetic field perpendicular to the current that flows in it. Thus, a Hall effect sensor consists of a metal strip through which a current flows. When a magnetic fields is applied, electrons move toward an edge and produce a voltage gradient. The force induced by the charged particles has to balance to the force generated by the magnetic field. It follows that the Hall voltage is a measure of the magnetic flux density. Although this type of magnetometers is mostly used in application with large magnetic field strength, such as anti-lock braking systems.

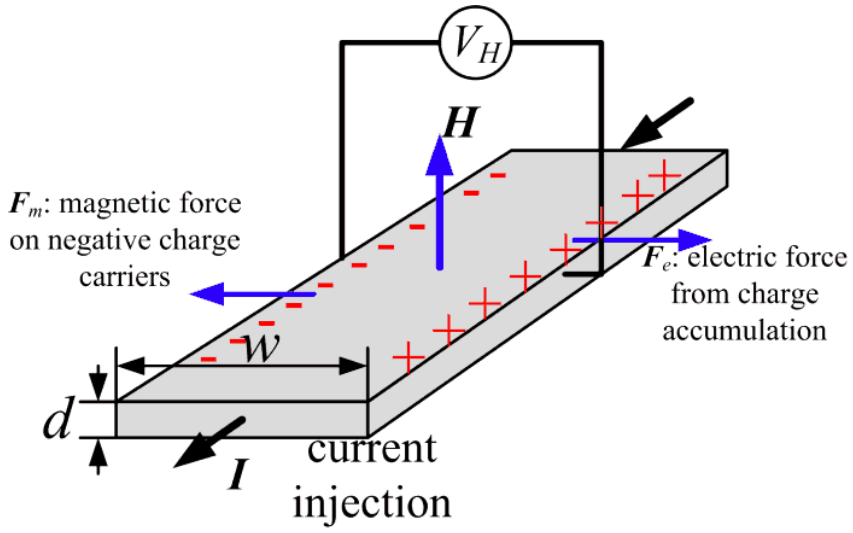

Figure 4.9: *Schematic illustration of an Hall effect sensor: a constant current I and a constant magnetic field H are applied. H is perpendicular to the surface and so to the direction of current flow. This leads to an accumulation of charged particles in the transverse direction to the current flow, so the Hall voltage (V_h) occurs. F_m is the magnetic force and F_e is the electric force. Taken from [42].*

In gait analysis, the physical principle which is commonly exploited is the magneto-resistivity. For example the commercially available MIMUs of Xsens Technologies B.V (Enschede, The Netherlands), MTi and Mtx comprise a magnetometer which uses a thin-film magnetoresistive principle [43]. Magnetoresistance is a characteristic of ferromagnetic materials which change their electrical resistance if they are in a magnetic field. It follows that this category of magnetometers produce a voltage proportional to the magnetic field. If the device is in an environment with no magnetic field, the current flows straight in a semiconductor plate. If a magnetic field is applied, thus the current flow deflects, because of the generation of the Lorentz force. Hence the current follows a longer path and subsequently the electrical resistance of the plate increases. The increment of resistance depends on the magnetic flux density and tilt angle with respect to the magnetic field direction. The magnetoresistance effect depends on the geometry and the configuration of the device. Several studies have been carried out to evaluate the performance of such devices with respect to different configurations [42]. It should be noted that the Hall effect sensor responds to magnetic field perpendicular to the sensor, while the magnetoresistive one is sensitive to parallel fields, as Figure 4.10 shows.

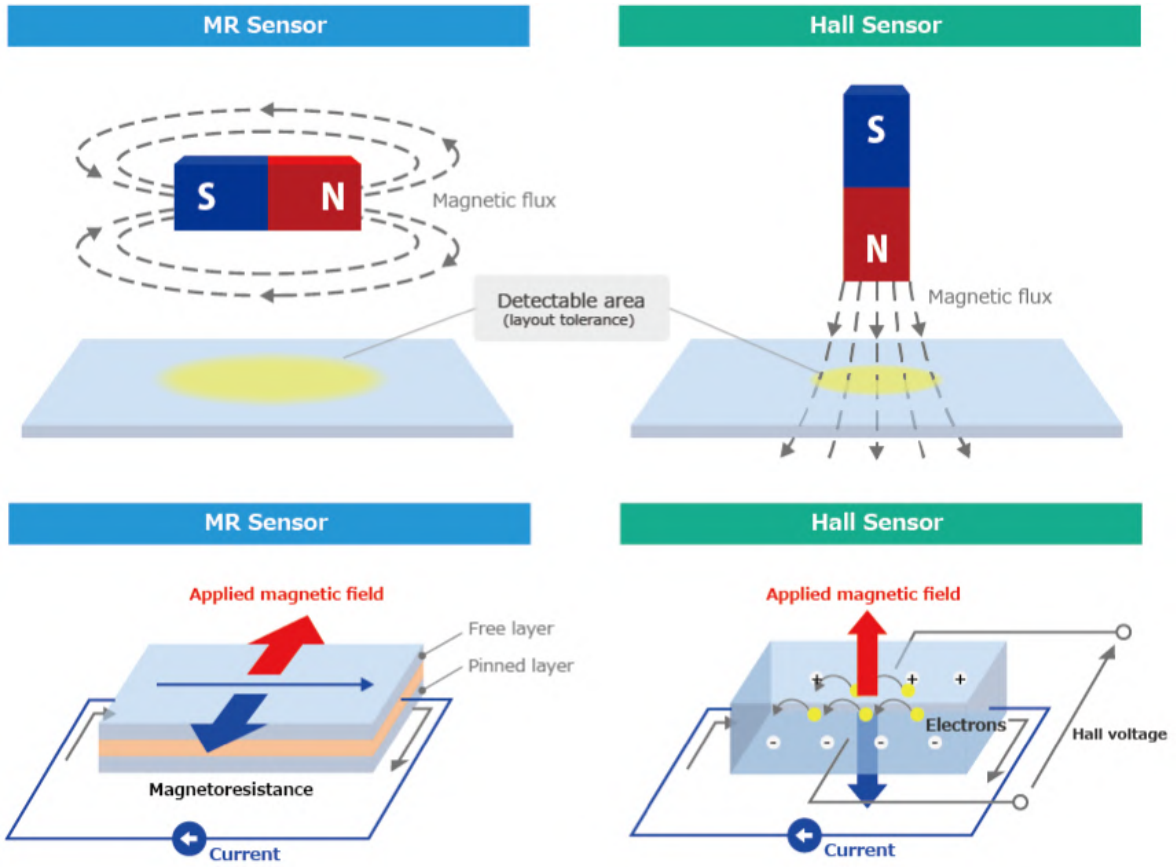

Figure 4.10: *These figures show the differences between Hall and magnetoresistive (MR) sensors: MR sensors have a wider detectable area since they detect the parallel magnetic field. Source: www.alps.com*

Earth's magnetic field is characterised by inclination and declination, as it can be seen in Figure 4.11. The inclination is the angle between the Earth's magnetic field and its projection on the horizontal plane, while the declination is the angle between the geographic North and projection of the Earth's magnetic field on the horizontal plane pointing towards the magnetic north.

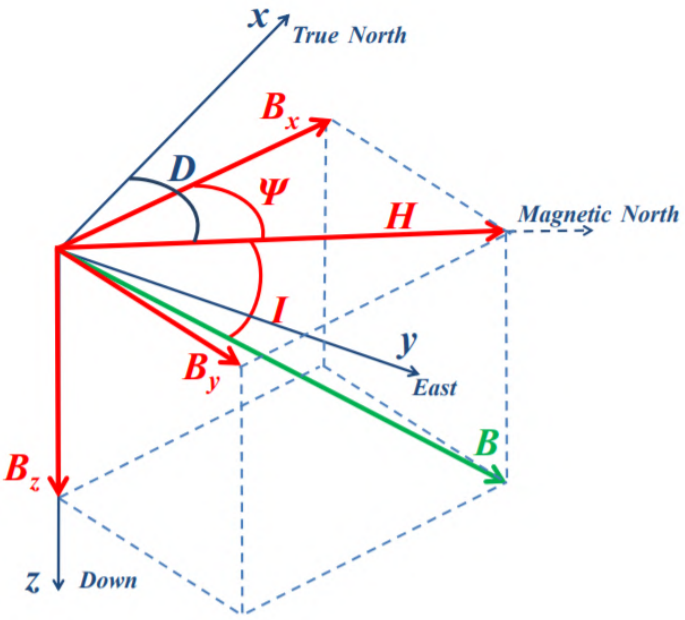

Figure 4.11: *'Earth's magnetic field in the Cartesian coordinates', taken from [44]. B is the Earth's magnetic field and H is its projection on the horizontal plane.*

In the orientation estimation application, the useful information derived from the magnetometer is the components of the Earth's magnetic field from whom we can extract the orientation through trigonometry rules. Indeed, if the sensor changes orientation also the components of the magnetic field along the sensing axes change. In this situation it is clear that the ideal condition reckons on the only presence of the Earth's magnetic field. If there are also external fields, we must try to exclude this disturb. In presence of these magnetic distortions the information provided by the magnetometer is heavily compromised and not reliable for orientation estimation. The worst scenario is the proximity of ferromagnetic objects. The main disturbances are classified as related to hard- and soft-iron. The former is defined as the additive magnetic field superimposed by a permanent magnet. Removing this field it is quite easy since it can be seen as a bias, thus we can remap the magnetic field excluding the disturbance. The soft-iron, instead, is the corruption of the Earth's magnetic field induced by an object with soft-iron properties, it is not additive and depends on the orientation of this source with respect to the geomagnetic field and also to the sensor. The compensation of the disturbances in this case is more complicated. However, it is even worst the case in which the magnetic disturbance is not known a priori, such as while the sensor is moving in a space not studied before, like outdoor walking. Thus would lead to an error that we could try to compensate comparing the components of the sensed magnetic vector before and after the instant in which the disturbance starts to appear.

Anyway, the magnetometer is used together with the accelerometer to provide accurate estimates of the orientation of the object on which they are attached, since in aggregate they can overcome the limits of the single sensor. Indeed, when an accelerometer lies in a horizontal plane, it is not sufficient to estimate the complete orientation but only the attitude. The information of the rotation around the vertical axis is added by the use of the magnetometer which provides the heading estimates. This is not possible only if the sensor is at magnetic poles, where the magnetic vector coincides approximatively with the gravity, so there is not any additive information. Hence the geomagnetic field changes with the geographic position, but for recordings in confined area the direction of Earth's magnetic field can be considered as constant.

Chapter 5

Orientation representation and transformation of coordinates

The orientation can be represented by several forms: Euler angles, direction cosine matric (DCM), quaternions and angle-axis. The Euler form uses three angles and it is the most conceptually easy to understand, but it has the great limit of a singularity state commonly referred as 'gimbal lock' [35]. On the contrary, DCM and quaternion do not incur a singularity state. In this study the choice falls on the quaternions as orientation representation for algorithms since the DCM consists of a 3x3 matrix, while the quaternions offer a linear formulation of the orientation dynamics and require less computational cost and storage memory since they have four parameters rather than nine as in the case of rotation matrix [35].

Regardless of the choice of the method of representation, to represent the orientation of a body, two coordinate systems have to be defined: one for the global coordinate system (GCS) and one for the local or body coordinate system (LCS) which is fixed with the body's motion. The first one is inertial, while the second not. Each coordinate systems is described by an origin and a orthonormal basis and it is assumed to be right-handed oriented. A common and practical choice is to define the x axis of GCS oriented in the direction of the Earth's north magnetic and the z axis as the direction of the gravity, pointing downwards. A vector in the space can be described in both the coordinate systems and it must be possible to convert the expression of the vector referred to GCS to LCS and vice versa. The relation between the two coordinate systems thus must be known thanks to the relative orientation between them. The coordinate systems are determined by a fixed origin, ${}^{\mathrm{G}}O$ and ${}^{\mathrm{L}}O$, and a basis, $\{g_x, g_y, g_z\}$ and $\{l_x, l_y, l_z\}$ for global and local frame respectively, as the illustration 5.1 shows. Expressing a 3D point in a coordinate system means to describe its components with respect to the chosen basis. If $p = \{p_x, p_y, p_z\}^{\mathrm{T}}$ is a point vector and we want to refer it to a system whose base is $\{s_x, s_y, s_z\}$, then p becomes:

$$ {}^{\mathrm{S}}p = p_x {}^{\mathrm{S}}x + p_y {}^{\mathrm{S}}y + p_z {}^{\mathrm{S}}z \tag{5.1} $$

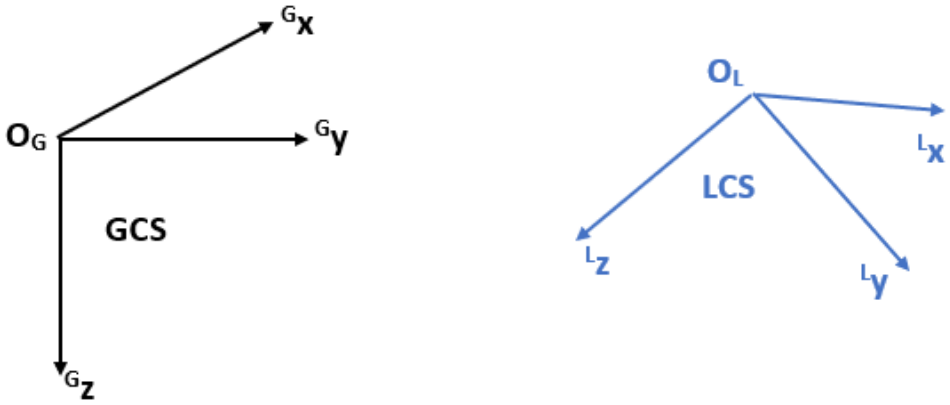

Figure 5.1: *Illustrations of a global and local coordinate systems: x y z global axes point to North, East and Down respectively.*

5.1 Rotation Matrix

The rotation matrix (${}^{\mathrm{G}}R_L$) is a 3x3 matrix which represents the relative orientation between two different coordinate systems. If a vector described in the local system r is multiplied for this matrix, thus we obtain the components of the same vector described in the global system. The matrix elements are the components of a system revolved in the other one, so the dot products between the components expressed in the two different bases: the columns contain the components of the local base (L) resolved in the global base (G), while the rows contain the components of the base G resolved in L.

$$ {}^{\mathrm{G}}R_L = \begin{pmatrix} {}^{\mathrm{L}}x \cdot {}^{\mathrm{G}}x & {}^{\mathrm{L}}y \cdot {}^{\mathrm{G}}x & {}^{\mathrm{L}}z \cdot {}^{\mathrm{G}}x \\ {}^{\mathrm{L}}x \cdot {}^{\mathrm{G}}y & {}^{\mathrm{L}}y \cdot {}^{\mathrm{G}}y & {}^{\mathrm{L}}z \cdot {}^{\mathrm{G}}y \\ {}^{\mathrm{L}}x \cdot {}^{\mathrm{G}}z & {}^{\mathrm{L}}y \cdot {}^{\mathrm{G}}z & {}^{\mathrm{L}}z \cdot {}^{\mathrm{G}}z \end{pmatrix} \tag{5.2} $$

It should be noticed that dividing the components of a vector by the vector module we obtain the cosine of the angles between the vector and the axes used to described it. These cosines are called direction cosines. Thus, for a unit vector the direction cosines coincides with the components of the vector itself. The scalar product between two components of different bases, which are unit vectors, are the cosine of the angles between the two considered unit vectors. This is why ${}^{\mathrm{G}}R_L$ is also called Direction Cosine Matrix (DCM). Since the elements derive from the dot product between two orthonormal bases, the matrix is orthogonal.

If it is known a rotation matrix which allows to transform the components of a vector from a third basis B to the G, we can multiply more than one matrices to obtain the orientation of B with respect to L:

$$ {}^{\mathrm{G}}R_B = {}^{\mathrm{G}}R_L {}^{\mathrm{L}}R_B \tag{5.3} $$

To change the reference system of vector is possible simply multiplying it for the rotation matrix which links the coordinate system in which it is expressed and the one in which we want to resolve it:

$$ {}^{\mathrm{G}}p = {}^{\mathrm{G}}R_L {}^{\mathrm{L}}p \tag{5.4} $$

If ${}^{\mathrm{G}}R_L$ is known and a matrix that converts the components in G to the one in L is needed, it is sufficient to transpose the matrix. Since the DCM is orthogonal, its transpose coincides with

its inverse.

$$^{\mathrm{G}}R_L = {}^{\mathrm{L}}R_G{}^{\mathrm{T}} \tag{5.5}$$

For example, we can think of a positive rotation of the local frame around the $^{\mathrm{G}}z$ axis by an angle α, as the Equation 5.6 shows. The corresponding DCM is:

$$^{\mathrm{G}}R_L = \begin{pmatrix} \cos\alpha & -\sin\alpha & 0 \\ \sin\alpha & \cos\alpha & 0 \\ 0 & 0 & 1 \end{pmatrix} \tag{5.6}$$

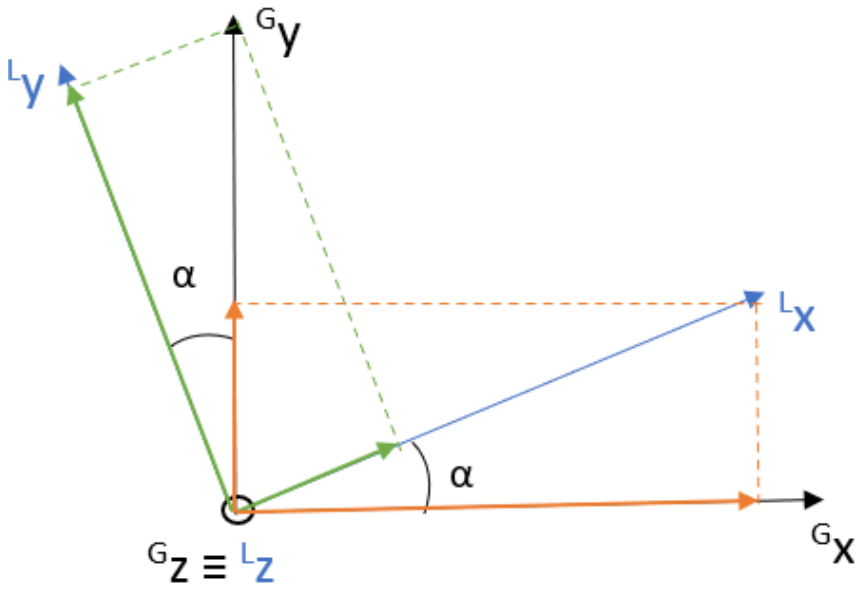

Figure 5.2: *Illustration of a positive rotation of the L basis around the z axis of an angle α. Since we consider right-handed coordinate systems the positive rotation is in the counter-clockwise direction.*

5.2 Euler angles

Euler angles aim at describing the orientation of a rigid body with respect to a reference coordinate system, considering three consecutive rotations around the axes of the moving body. The sequence in which the rotations are done influences the final result, thus it is important to specify the order of the axes around which the rotations occur. The valid combinations must not have two consecutive rotations around the same axis, so the possible sequences are twelve. If we consider only the ones which start and finish with different axes, the possibilities are: XYZ, XZY, YXZ, YZX, ZXY, ZYX, which are called Tait-Bryan angles. ZXZ, ZYZ, XYX, XZX, YXY, YZY are called proper Euler angles. If for example we want to express in form of DCM the sequence of rotations XYZ with angles α, β, γ, the total rotation matrix would be:

$$^{\mathrm{G}}R_L = \begin{pmatrix} 1 & 0 & 0 \\ 0 & \cos\alpha & -\sin\alpha \\ 0 & \sin\alpha & \cos\alpha \end{pmatrix} \begin{pmatrix} \cos\beta & 0 & \sin\beta \\ 0 & 1 & 0 \\ -\sin\beta & 0 & \cos\beta \end{pmatrix} \begin{pmatrix} \cos\gamma & -\sin\gamma & 0 \\ \sin\gamma & \cos\gamma & 0 \\ 0 & 0 & 1 \end{pmatrix} \tag{5.7}$$

The Tait-Bryan angles are also defined in aerospace engineering as yaw, pitch, and roll. To define these three angles we have to consider the axes of the original frame (x, y, z) and the ones

of the rotated frame (X, Y, Z). To describe the orientation of a body with respect to a global frame, we can consider that the coordinate system x, y, z is the fixed one and X, Y, Z is the one which follows the rigid body. If the two frames are distinct, they intersect in a lie called line of nodes, found as the intersection of planes xy ad XY. The intermediate states are x', y', z' (the frame after one rotation), and x", y", z" (the frame after the second rotation).

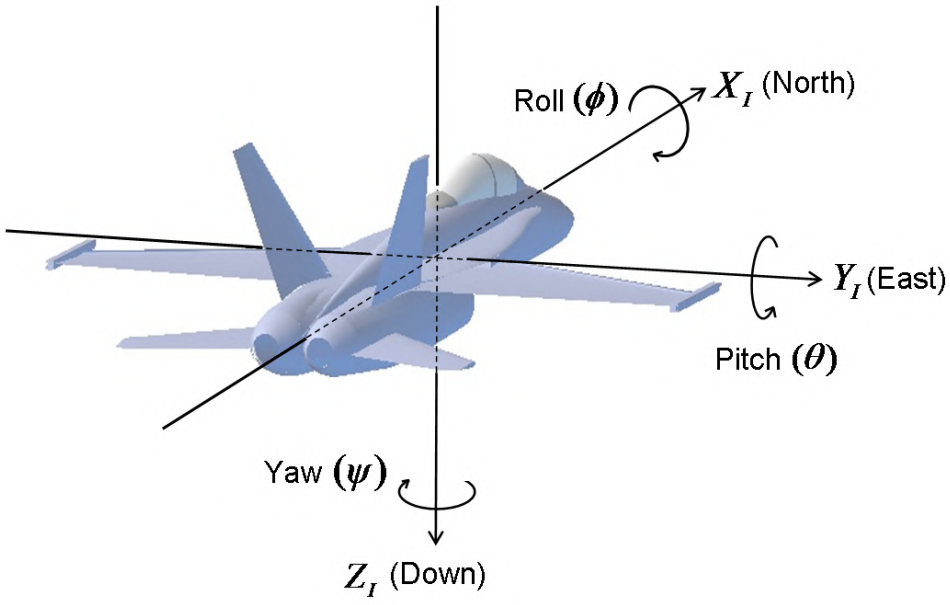

Figure 5.3: *Definition of the Euler angles in aircrafts. Source: http://www.chrobotics.com/library/understanding-euler-angles.*

The Euler angles are defined as follows:

- α the angle between x axis and the line of nodes, called yaw. It describes a rotation around the Z axis;
- β is the angle between z axis and Z axis, called roll. It describes a rotation around the x' axis;
- γ is the angle between X axis and the line of nodes, called pitch. It describes a rotation around the z" axis.

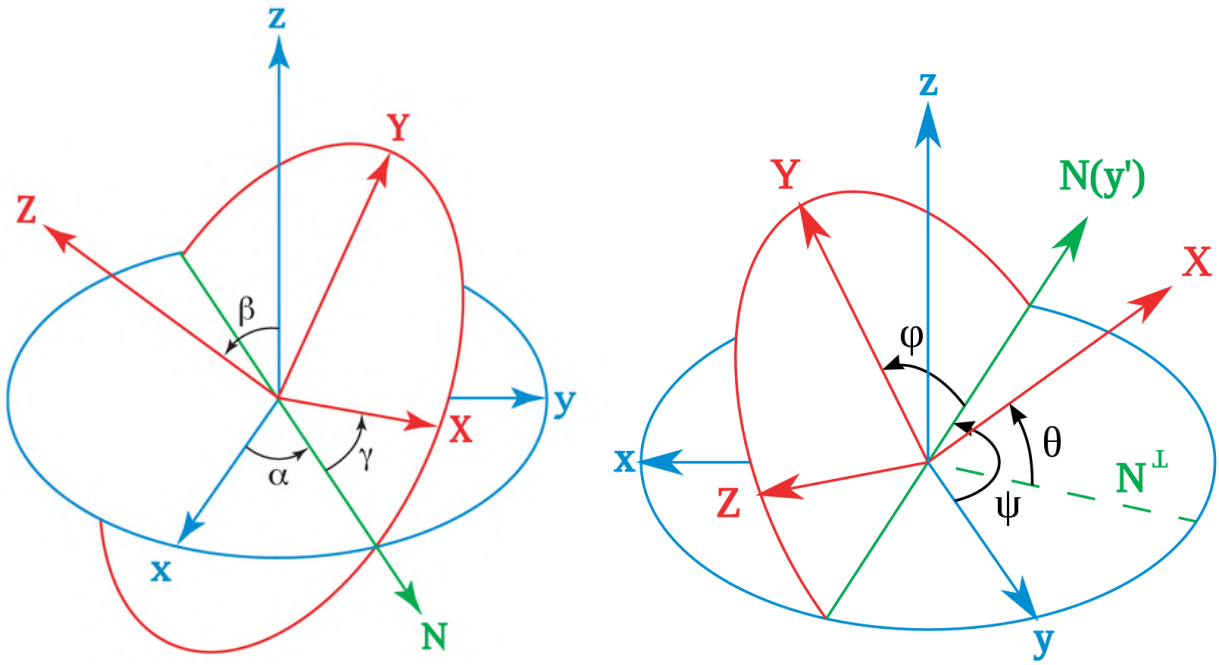

Figure 5.4: *Definition of Euler angles. Left: proper angles. Right: Tait-Bryan angles. Image source: https://en.wikipedia.org/wiki/Euler_angles.*

Although Euler angles consist of the method of orientation representation of most immediate interpretation, they suffer from a singularity state called gimbal lock, because of the close connection with the gimbals used in inertial navigation systems. This situation occurs when there is an alignment of two rotating axes long the same direction with the subsequent loss of a degree of freedom. This indetermination is related to the proper sequences, so when the first and last rotation axis are the same. This, indeed, happens when the second rotation is 0° or 180° in proper angles ($\pm 90^\circ$ in Tait-Bryan angles). Hence, if the pitch is $\pm 90^\circ$, then the yaw axis gimbal becomes parallel to the roll one. This error mathematically origins from the equations at the basis of the Euler angles with sine and cosine defined in specific intervals and which do not cover all the possibilities. According to Equation 5.7, if β is $\pm 90^\circ$ then we obtain:

$$ {}^{\mathrm{G}}R_L = \begin{pmatrix} 0 & 0 & 1 \\ \sin\alpha + \gamma & \cos\alpha + \gamma & 0 \\ -\cos\alpha + \gamma & \sin\alpha + \gamma & 0 \end{pmatrix} \tag{5.8} $$

from which it can be deduced that it represents a rotation only around the Z axis.

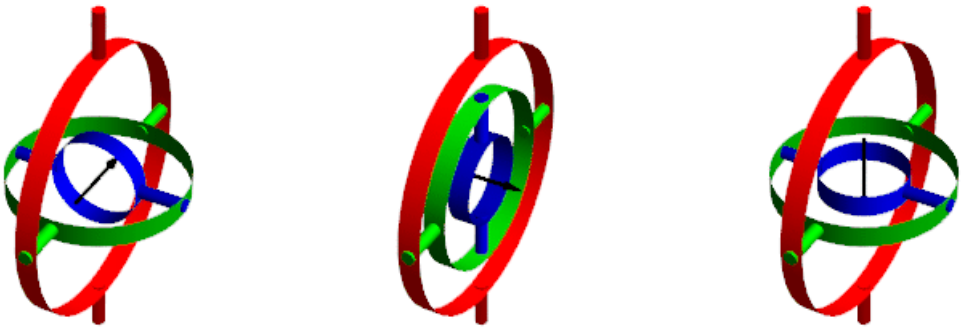

Figure 5.5: *Left: the three gimbals are indipendent. Centre and right: gimbal lock configurations, the pitch is* $\pm 90^\circ$ *so the first and third gimbals are parallel. This leads to the impossibility to distinguish yaw and roll angles. Credits to: https://www.allaboutcircuits.com/technical-articles/dont-get-lost-in-deep-space-understanding-quaternions/.*

5.3 Quaternions

In this thesis the quaternion is defined as [35]:

$$ {}^{\mathrm{A}}_{\mathrm{B}}q = [q_o, q_1, q_2, q_3] \tag{5.9} $$

$$ {}^{\mathrm{A}}_{\mathrm{B}}q = [\cos(\alpha/2), e_x \sin(\alpha/2), e_y \sin(\alpha/2), e_z \sin(\alpha/2)]^{\mathrm{T}} = [\cos(\alpha/2), \sin(\alpha/2) \cdot n^{\mathrm{T}}]^{\mathrm{T}} \tag{5.10} $$

Where α is the rotation angle and e is the unit vector that represents the rotation axis. So that quaternion describes an arbitrary rotation of the coordinate system A with respect to B. α and n are the variable which define the orientation in a angle-axis representation. Thus, the quaternions can be used to describe any generic rotation around n by an angle α.
The conjugate quaternion, given its unit norm, is equivalent to the inverse quaternion and describes the inverse rotation. Therefore, the conjugate quaternion can be used to represent the orientation of frame B relative to frame A, as defined below [35].

$$ {}^{\mathrm{A}}_{\mathrm{B}}q = {}^{\mathrm{B}}_{\mathrm{A}}q^{*} = [q_0, -q_1, -q_2, -q_3]^{\mathrm{T}} \tag{5.11} $$

The orientation after a series of rotations can be found by multiplying the quaternions and the quaternion product is defined as follows:

$$ p \otimes q = \begin{bmatrix} p_0q_0 - p_1q_1 - p_2q_2 - p_3q_3 \\ p_0q_1 + p_1q_0 + p_2q_3 - p_3q_2 \\ p_0q_2 - p_1q_3 + p_2q_0 + p_3q_1 \\ p_0q_3 + p_1q_3 - p_2q_1 + p_3q_0 \end{bmatrix} \tag{5.12} $$

The quaternions can apply rotations to 3D vectors. If a vector is referred to a frame A and the relation between frames A and B is known, the vector can be transformed to be referred to frame B:

$$ {}^{\mathrm{B}}v = {}^{\mathrm{B}}_{\mathrm{A}}q \times {}^{\mathrm{A}}v \times {}^{\mathrm{B}}_{\mathrm{A}}q^{*} \tag{5.13} $$

The same concept can be expressed by a rotation matrix 3x3 (DCM) which is derived from the relative quaternion as follows:

$$ R({}^{\mathrm{B}}_{\mathrm{A}}q) = \begin{bmatrix} q_o^2 + q_1^2 - q_2^2 - q_3^2 & 2(q_1q_2 - q_0q_3) & 2(q_1q_3 + q_0q_2) \\ 2(q_1q_2 + q_0q_3) & q_0^2 - q_1^2 + q_2^2 - q_3^2 & 2(q_2q_3 - q_0q_1) \\ 2(q_1q_3 - q_0q_2) & 2(q_2q_3 + q_0q_1) & q_0^2 - q_1^2 - q_2^2 + q_3^2 \end{bmatrix} \tag{5.14} $$

The formulation of the quaternions as descriptor of orientation is redundant since the quaternion q represents the same rotation of -q, because rotating of α around the axis $n$is equivalent to rotate by -α around -n.

The use of quaternions enables some advantages. Indeed, despite they are not easily intuitive, they are largely used in orientation estimation, also in human motion analysis. They do not suffer from any singularity such as gimbal lock, as the Euler angles do. As the opposite of the DCM, trigonometric operations are not involved, allowing a decreased computational time required, and the parameters can be only four instead of nine [35].

Chapter 6

Orientation estimation

As anticipated in the previous chapters, the MIMU can be used to estimate the orientation of the body on which it is attached. The sensors in the MIMU taken individually are not sufficient to provide an accurate estimate in every possible situation. The principle limits and characteristics of the sensors contained in the MIMU are the following:

- The gyroscope suffers from important biases which would lead to drift in estimates. It provides a 3D angular velocity with respect of course to MIMU coordinate system which can potentially be integrated to achieve the orientation variation with respect to the initial instant. Hence, anyway the gyroscope could not lead to an absolute orientation. As a matter of fact, using only the gyroscope to estimate the orientation is not practicable, especially if the used gyroscope is low-cost, since the signals are affected by biases and white noise, which are responsible for a drift error that increases more and more with time. The biases cause estimate errors that grow linearly with time. The white noise leads to errors which can be characterised by the noise specification of the angle random walk. The latter describes the average deviation occurring when the angular velocity signal is integrated, so the error between the expected angle and the found one. Its standard deviation grows with the square root of time. Hence, the gyroscope can provide relative estimation of orientation whose accuracy becomes worse as the integration time increases.

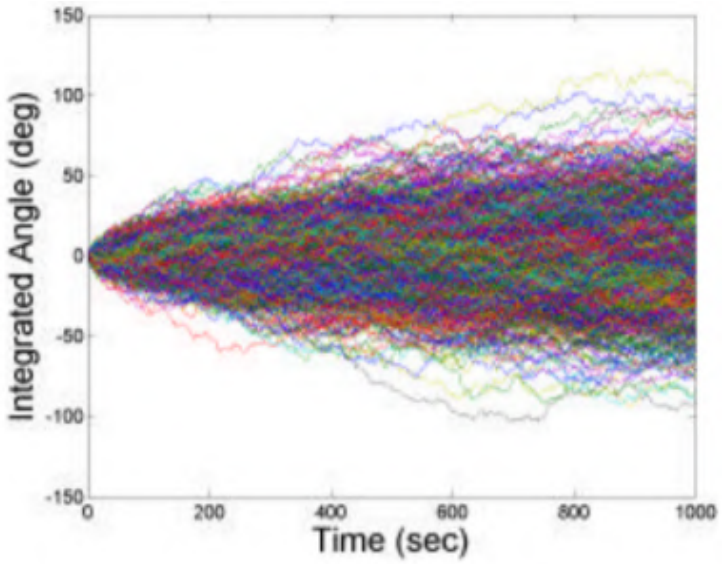

Figure 6.1: *This figure shows the result of the integration of 1000 trials, integrating the noise rate for 1000 seconds. Credits to: Walter Stockwell, 'Angle Random Walk', Crossbow Technology, Inc*

- The accelerometer does not distinguish between the gravity acceleration and the external acceleration applied to the body. It follows that the accelerometer can provide the information of the sensor inclination only if the gravity is the unique acceleration, so if the body is at rest or if it is moving with constant velocity. Furthermore, since accelerometer's information is based on gravity direction, this sensor cannot sense a rotation around the vertical axis. Fusing the information of gyroscope and accelerometer can be done firstly integrating the angular velocity but taking the information of the initial (static) condition from the accelerometer.
- The magnetometer is heavily sensitive to ferromagnetic or electrical disturbances which would lead to unreliable information. If this problem is not present, the sensing of the Earth's magnetic field represents the complementary information that enables a complete absolute orientation estimation. Indeed, magnetometers provide the heading estimation, which the accelerometer is not able to give. Only at Earth's magnetic poles the gravity and the magnetic field directions coincide and the heading information cannot be added.

It follows that all the information coming from MIMU sensors has to be merged purposefully to overcome all the limitations of the single sensors. Algorithms that perform this fusion of information are called sensor fusion algorithms.

6.1 Sensor fusion algorithms

Sensor fusion algorithms allow to estimate the relative orientation between GCS and the MIMU coordinate system. If the Local Coordinate System (LCS) and MIMU coordinate system are aligned, the found orientation between the GCS and MIMU coordinate system coincides with the one between the GCS and the LCS, as it is assumed in this study. If this hypothesis is not valid, thus the relative orientation between the MIMU and the LCS must be known.

The fundamental idea which is at the base of sensor fusion algorithms is to integrate the bias-free angular velocity from the gyroscope and then correcting this value with the readings

from accelerometer and magnetometer. The weight given to the sensor information depends on the motion and environmental conditions: for example the accelerometer's readings are more reliable and so more weighted if the body is in statics, the magnetometer's signals are more considered if there are not magnetic disturbances superimposed to the Earth's magnetic field. Trying to remove the bias is hard in particular if the gyroscope is low-cost, so the adjustments to the integration of the angular velocity, which would bring to a higher and higher drift over time, become of crucial importance. Accelerometers and magnetometers are used to bound the drift errors.

There are two main ways through which the orientation can be estimated: the deterministic filters and the optimal filters. The former use a minimal set of data and solve the problem of the orientation with non-linear equations, the latter use more than one minimal set and obtain the orientation minimizing a cost function.

6.1.1 Deterministic approach

The deterministic approach finds its basis in 1965 to solve the problem proposed by Whaba. This problem consisted in obtaining the orientation using the observation of at least two distinct vectors at a single instant of time, constructing the rotation matrix from the LCS to the GCS [5]. This can be done exploiting at a certain instant the vectors of the Earth's magnetic field from the magnetometer and the Earth's gravity acceleration from the accelerometer, without the need of knowing the state of the sensor at previous instants. In literature many solutions have been proposed, among which three-axis attitude (TRIAD) and the optimal quaternion estimator (QUEST) ca be cited [36]. Since these methods consider only the vector observations, they exclude the gyroscope information. Because of the reasons explained in previous sections, all the MIMU data should be use to guarantee an accurate estimate and so nowadays these solutions are not so common. The information of the gyroscope is considered as crucial in the orientation estimation and all MIMU data are combined together with complementary filters (CF), which are the most widespread deterministic approach.

6.1.1.1 Complementary Filters

CFs use an analysis in the frequency domain that consists in filtering to high frequency the gyroscope signal, since it is affected by low-frequency disturbance (biases) in the attempt to reduce its drift problem, and filtering to low frequency the signals of accelerometer and magnetometer to reduce the high-frequency noise. As a matter of fact, the difference among CF algorithms consists of how the accelerometer and the magnetometer signals are exploited to correct the orientation drift due to the angular rate integration. To guarantee that the filtered combination of signals covers the entire range of frequencies, the cut-off frequency is the same for both filters, so the choice of the it must be a trade-off between the bandwidths of both signals.

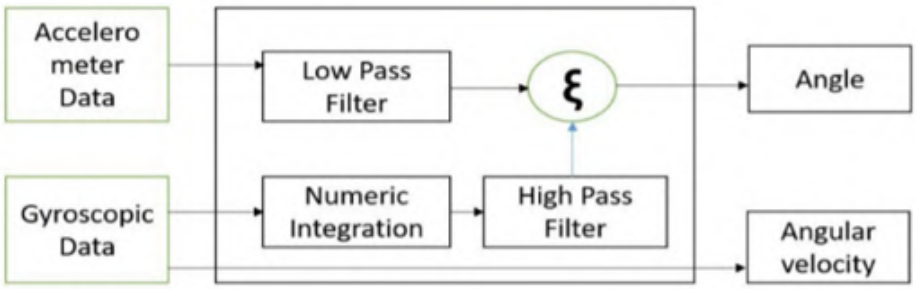

Figure 6.2: *Block diagram of a generic complementary filter, [47]. ξ is the parameter that has to be set.*

Anyway, the deterministic approach, as the name suggests, refers to mathematical models which describe a system and, given a model, the found result will be always the same, thus the fusion of the data does not comprise a stochastic description. This leads to some advantages, as well as to some drawbacks of this approach. It requires low computational cost, is generally characterised by relative simplicity, such as for the reduced number of setting parameters, and can be implemented on microprocessors embedded with MIMU [5]. On the other hand, since they are based on mathematical approximation of reality, they contain certainly some errors.

6.1.2 Stochastic approach

Kalman filter (KF) has been named in this way because of the publication of Kalman in 1960, where he proposed an innovative stochastic approach of sensor fusion applicable in many fields [48].
KFs use a probabilistic determination of the result through a stochastic approach. This approach tries to overcome the deterministic limits, in fact mathematical models are never perfect but only approximation of reality, thus since some parameters are associated to a certain degree of uncertainty, then the disturbances cannot be deterministically described. Furthermore, the sensor measurements introduce distortions, so even they do not describe the actual state of the system without unpredictable errors. Hence, this approach aims at replacing the systems deterministic variable with probability distribution functions.
The KF works correlating iteratively the current states with the predicted ones. The current state of the system is used to guess the future one. Since the dynamic systems continuously change, the KFs can be a proper solution to achieve an educated guess of the incoming state. Since the filter predicts future states based on the previous ones, the initial first state must be known. To make an evaluation of the prediction error the filter applies a correlation between what has been predicted and what actually happens, reading the MIMU data.

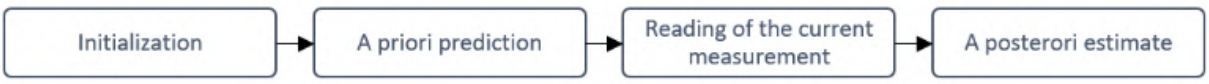

Figure 6.3: *Diagram of Kalman filter main steps*

More specifically, the KF is a particular type of analytically determined Bayesian filters,

which are the recursive estimators of a posteriori probability distribution function and are based on the Markov chain. The latter is a stochastic model defining a sequence of possible events whose probability to happen depends only on the just previous state and not on the sequence of events that preceded it. For the sake of clarity, the Bayesian filter is based on the Hidden Markov model, which is a Markov chain with not directly observable or hidden states. If x are the observable states and z are the measurements, Markov property can be modelled as follows:

$$p(x_k|x_{1:k}, z_{1:k-1}) = p(x_k|x_{k-1}) \tag{6.1}$$

$$p(z_k|x_{1:k}, z_{1:k-1}) = p(z_k|x_k) \tag{6.2}$$

where it is stated that the probability of the true state x at the instant k depends only on the just previous state $k-1$ and the probability of the measurements depends only on the state of the same instant. The model of the state is time-discrete and at the instant k it is:

$$x_l = f_{k-1}(x_{k-1}, w_k) \tag{6.3}$$

where f is a non-linear function which provides the model predicted by considering the previous state $x_k - 1$ and the process noise w. While the measurement model at the instant k is:

$$z_k = h_k(x_k, v_k) \tag{6.4}$$

where h is a non-linear function which enables to obtain the measurement state from the state model at the same instant k and v, which is the measurement noise. The noises have to be taken into account to consider the variation of the dynamic model and electrical sensor corruptions. The main hypotheses are that the process noise and measurement noise are white with known probability distribution functions, and the uncorrelation between them, which are also independent from the initial state. Goal of all the Bayesian filters is to achieve the estimation of the model state at a certain instant k from all the previous measurements $z_{1:k}$ and the posteriori probability distribution function $p(x_k|z_{1:k-1})$. 'A posteriori' indicates a distribution function at the instant k after knowing the measurement at the considered instant.

The main steps are:

1. The prediction: in this step the a priori probability distribution function $p(x_k|z_{k-1})$ knowing the a posteriori probability distribution function at the previous instant $p(x_{k-1}|z_{k-1})$. The equation which enables to calculate it is integration of the product of two probability distribution functions:

$$p(x_k|z_{1:k-1}) = \int_{-\infty}^{+\infty} p(x_k|x_{k-1})p(x_{k-1}|z_{1:k-1})dx_{k-1} \tag{6.5}$$

2. The update: after that the current measurement is available, this is used to modify the estimation done before, so the above a priori probability distribution function. The formulation of the a posteriori probability distribution function is:

$$p(x_k|z_{1:k}) = \frac{p(z_k|x_k)p(x_k|z_{1:k-1})}{p(z_k|z_{1:k-1})} \tag{6.6}$$

6.1.2.1 Linear Kalman Filters and Extended Kalman Filters

KFs are based on a recursive algorithm that aims to reach the optimum minimizing the covariance error. All the assumptions done in the section above treating the Bayesian filters are still valid, since the Kalman Filter is equal to a Bayesian one if the functions of the a posteriori probability distributions are multivariate Gaussian. Thanks to this assumption, the mean and variance of the noise processes completely describe the distribution.

In the case of the linear KF, the models of the system is a linear functions of x_{k-1} and w_k, while the measurement model is a linear function of x_k and v_k. The choice to use linear functions derives from the higher simplicity to handle this type of functions. If the model is not appropriate, since there are high non-linearities, the filter is 'extended' to linearize the problem around the point of interest and find the state of a system perturbed by a non-linear noise.

To formulate the equations of KFs, first of all we have to define the following variables:

- x_k is the process state vector at the instant k;
- F_{k-1} is the transition matrix, which links the previous state with the current one, without considering any input or process noise;
- u_k is the vector whose elements are the control inputs;
- B_{k-1} is the input control matrix, which links the elements of u_k to the state vector;
- z_k is the vector of the measurements at the instant k;
- H_k is the matrix which links the current state vector with the measure vector;
- w_k is the process white noise with Gaussian distribution;
- Q_k is the covariance matrix of the process noise;
- v_k is the measurement white noise with Gaussian distribution;
- R_k is the covariance of the measure noise;
- P_k is the error covariance associated to the prediction step, which depends on the covariance matrix of the process (Q), and one for the measurements (R);
- K_k is the Kalman gain.

The symbol $^-$ states that the relating variable at instant k is considered before knowing the kth measurement. The state and measurement models are defined discretizing the equations 6.3 and 6.4:

$$x_k = F_{k-1}x_{k-1} + B_{k-1}u_k + w_k \tag{6.7}$$

$$z_k = H_k x_k + v_k \tag{6.8}$$

As explained for the generic Bayesian filter, also for the KF the main steps are the prediction and the update. Indeed it provides an estimate of the state at the instant k and then it receives the information of the noisy measurement of the same instant.

1. In the prediction phase, the state variables and uncertainties (error covariance) are estimated: a priori estimation of the current state and the covariance based on the knowledge of the previous state and the inputs. The equations related to this step are listed below:

$$\widehat{x}_k^- = F_{k-1}\widehat{x}_{k-1} + B_{k-1}u_k \tag{6.9}$$

$$P_k^- = F_{k-1}P_{k-1}{F^{\mathrm{T}}}_{k-1} + Q_{k-1} \tag{6.10}$$

2. Then the new noisy measurement becomes available and it is compared with the prediction;

3. In the update step, the error between what was expected and what happened is used to correct the a priori estimate. The a posteriori state and covariance are calculated and the predicted value is now updated. The update is practically done by means of a weighted average between the a priori state estimate and measurement relative to the same instant k. The weight given to the addends is related to their level of uncertainty associated. The purpose of this operation is to reduce the uncertainty with respect to the one which it would be found considering only the a priori state or only the measurement. The weights are defined by the principal parameter of the KF, the Kalman gain (K), which varies every instant. Since the dimension of the measured vector does not coincide with the one of the expected state, an appropriate matrix H is used to make them equal. The gain of the KF depends on the covariance matrices and it is related to the percentage of uncertainty due to the prediction with respect to the total one, therefore it is:

$$K = \frac{prediction\ uncertainty}{prediction\ uncertainty + measurement\ uncertainty} \tag{6.11}$$

The equations that characterise this step and so the computation of the Kalman gain and the a posteriori evaluation of the updated value of the state vector and its error covariance matrix are listed below:

$$K_k = P_k^{-} H^{\mathrm{T}}{}_k (R_k + (H_k P_k^{-} H^{\mathrm{T}}{}_k))^{-1} \tag{6.12}$$

$$\widehat{x}_k = \widehat{x}_k^{-} + K_k(z_k - H_k \widehat{x}_k^{-}) \tag{6.13}$$

$$P_k = (I - K_k H_k) P_k^{-} \tag{6.14}$$

Besides the Linear Kalman filers, there are the Extended Kalman filters (EKF). They are necessary since there are a lot of processes that could not be described by linear models. In these cases a possible solution consists of the linearization of the process and/or measurement model. If we linearize a model about a nominal trajectory non dependant on the measurements, the method takes the name of Linearized Kalman filter. If we linearize a trajectory at every instants exploiting the measurements, we consider an Extended Kalman filter. In EKF, the models are not linear. The linearization is done taking into account the mean and the covariance of the current state and it is actually performed by a Taylor expansion. In case of EKF, the fundamental steps are visible in Figure 6.4.

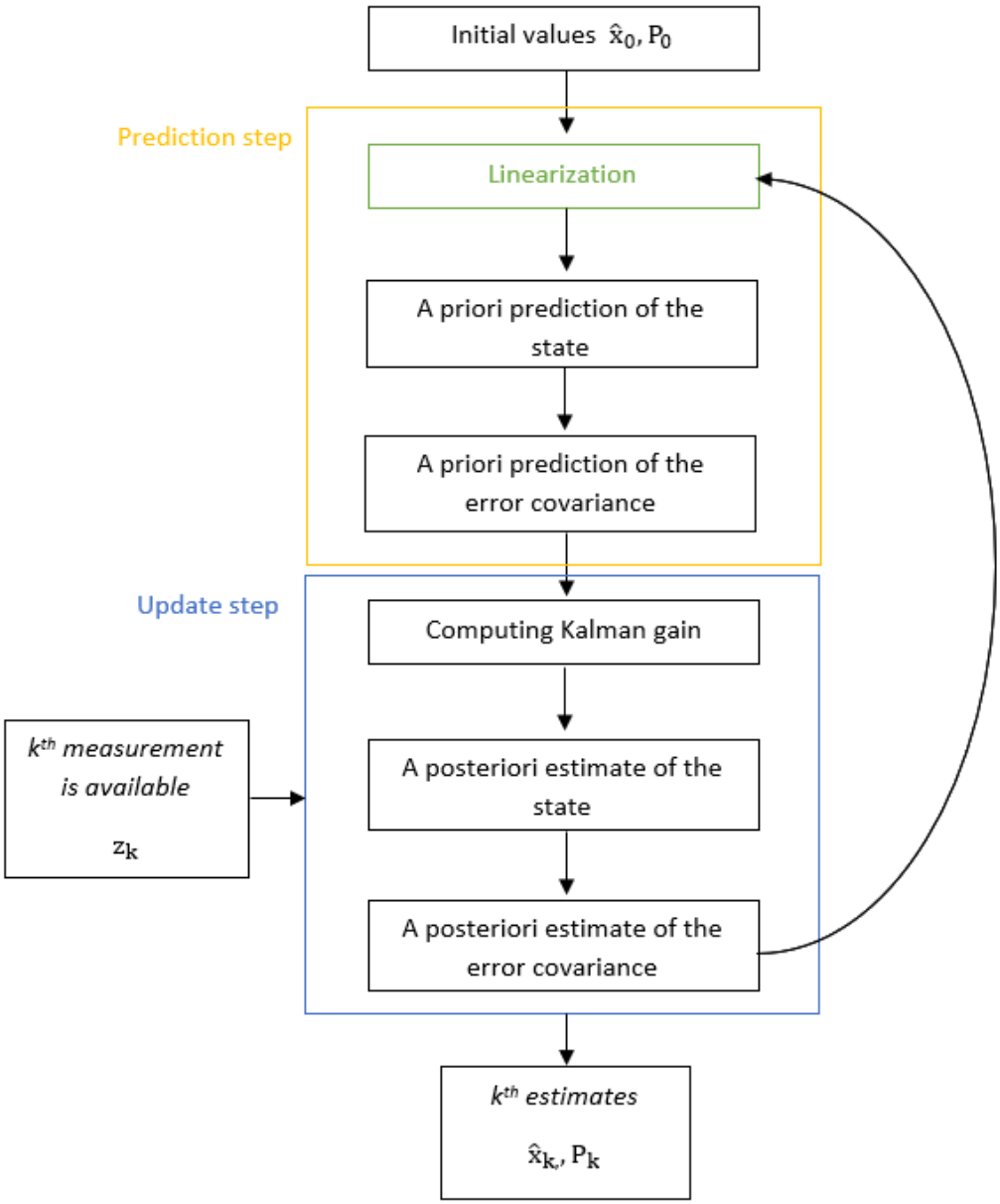

Figure 6.4: *Kalman filter fundamental steps: the green box (linearization) is present only in the Extended Kalman filter.*

6.1.3 Comparison between Complementary Filters and Kalman Filters

As stated in [50], the main advantages of CFs are the lower computational cost and the tuning of only one or few parameters, while the strengths of KFs are related to the flexibility of the algorithm that enables more freedom in creating the state and noise models. Furthermore, Kalman filters, as recursive filters, are appropriate in situations which require an estimate at every instant in which a new measurement is available. Since the data are processed in a sequence, it is not necessary to store all the information and once a data is processed, then it can be forgot. Hence, an advantage of the Kalman filter is to save nothing but the previous value, thus they require very low memory, and in many applications they are more accurate than CFs [47]. On the other hand, KFs involve high complexity, high computational cost and tuning of many paramters. Thus CFs seem to be a valid alternative with the strengths of easier implementation and less computation cost, which make them preferable in case of embedded systems [47].

Chapter 7

Estimation of spatio-temporal gait parameters

The assessment of spatio-temporal parameters of gait has a crucial importance in clinical evaluations. The principal parameters are defined in Part I, Section 3.2. The description of severity of movement disorders or of a precise gait pattern is based on the quantification of some predefined and measurable features of walking.

Step length, stride length and stride width can be evaluated using different methods and devices and each of them requires adjustments in the definitions of the parameters according to the way exploited to calculate them. Simple definitions (reported in Section 3.2), related to distances of the same point of the foot at a certain gait event to the next one, are not sufficient in many situations. If the walking is not assumed to be linear, as Huxham *et al.* [30] highlighted, the definitions of stride length, step length and step width have to be more general. First of all, the direction of progression (DoP) must be redefined at any stride, considering the DoP as the direction with the highest linear acceleration or normal to the direction with highest angular velocity (which indeed is the highest in mediolateral axis). Once the DoP is re-defined and the reference axes are changed, the usual definition of stride length can remain identical. As the step can overlap two strides with different directions of progression, the step length can be more generally redefined as 'the measured parallel to the direction of progression for the ipsilateral stride of which it is the second part' [30]. Indeed, the stride width can be considered as the distance, perpendicular to the stride, between the line of stride length, that is the line connecting two ipsilateral foot contact events, and contralateral foot contact during those events. For the sake of clarity, Figure 7.1 shows graphically the spatial parameters.

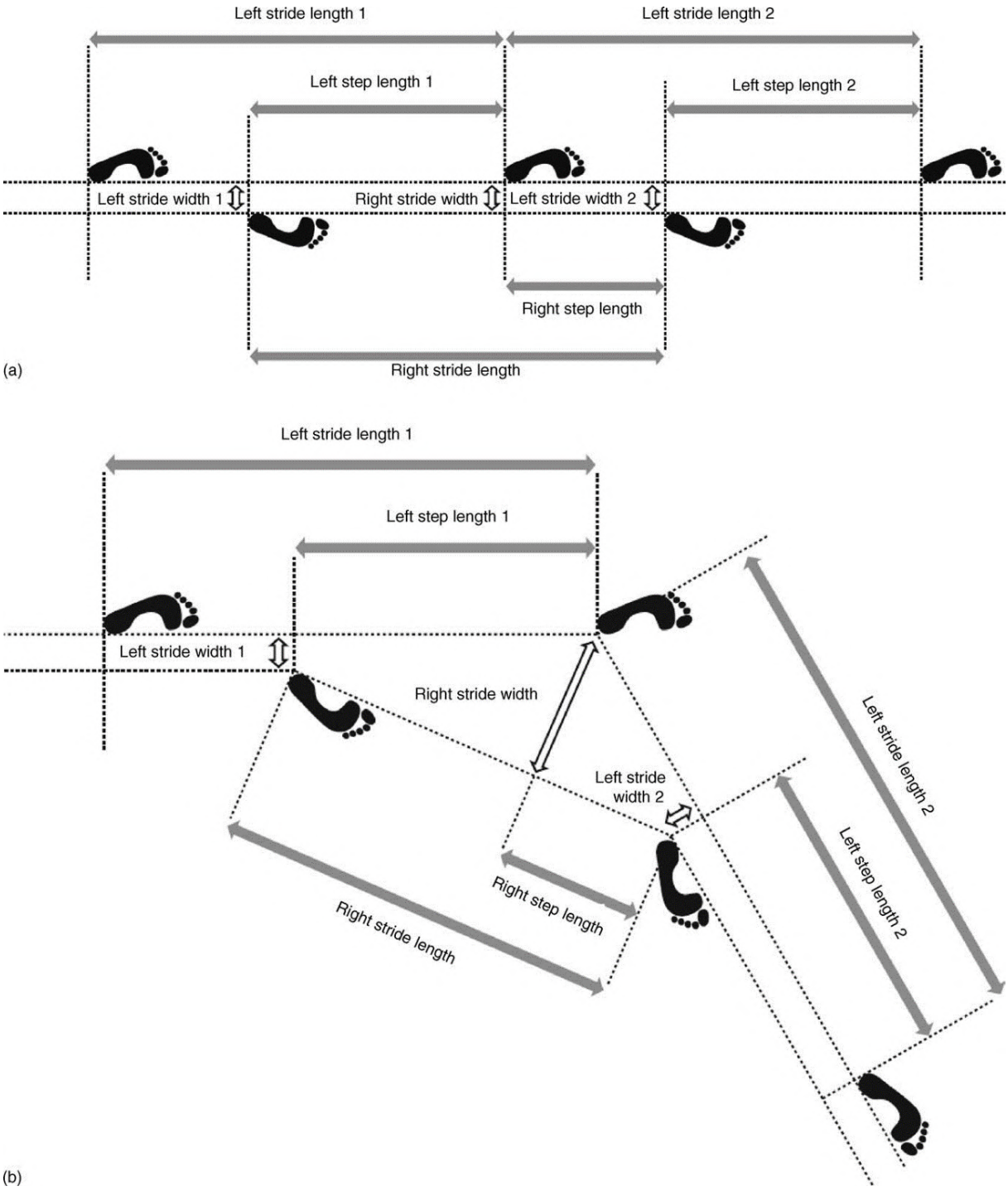

Figure 7.1: *Stride length, step length and stride width parameters in a) linear and b) non-linear walking, [30]. In this work it is assessed that stride width or step width are two different interchangeable names.*

The gold standard method in gait analysis (the SP) easily calculates the stride length with the distance between the positions in two equal subsequent gait events of the same marker attached on whatever point of the foot. Also step width and length definition depend on the position of the markers. For example in [10], the stride width is described as the lateral distance between the metatarsal marker of the stance foot and the heel marker of the swing foot at the instant of heel contact with the ground and the step length is calculated as the anteroposterior

distance between the heel markers of stance and swing foot at heel contact [10].
Furthermore, using the force plates, those spatial parameters are evaluated through the center of pressure positions, as it can be seen in Figure 7.2. In fact, as stated in [10], the step length is described as the difference between the most backward center of pressure position and the center of pressure position at rearfoot clearance, set as the second plateau of the mediolateral centre of pressure trace during gait. The step width, instead, is the difference between the most lateral position of the mediolateral center of pressure trace, obtained with its first plateau, and the mediolateral center of pressure position at rearfoot clearance. As Figure 7.2 shows, the center of pressure position along the anteroposterior axis is initially shifted backward and then steeply forward. While along the mediolateral axis the center of pressure position reaches two plateaus: one corresponding to the first stance phase, and the other corresponding to the second swing phase.

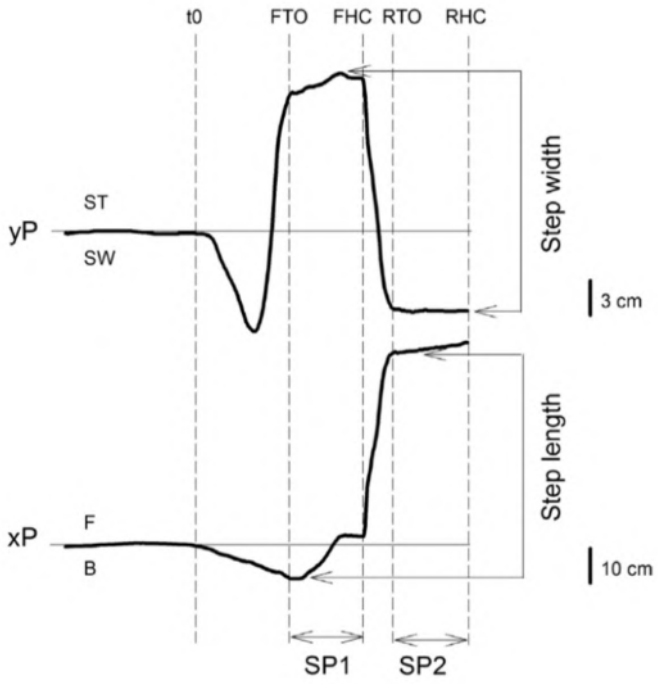

Figure 7.2: *Example of anteroposterior (xP) and mediolateral (yP) center of pressure traces during gait initiation, taken from [10]. FTO= forward toe off, FHC= forward heel contact, RTO= rear toe off, RHC= rear heel contact, SP1= first single support phase, SP2= second single support phase, F= forward, B= backward, ST= stance, SW= swing.*

In literature methods based on the use of MIMU to estimate the gait spatio-temporal parameters are more and more widespread. These MIMU-based approaches generally propose the attachment of a single MIMU on the trunk or on each lower limb. With this setup, it has found that the GE of initial and final contacts (ICs and FCs) with the ground (which are the basis information on which the estimation of parameters can be done) could be detected through specific patterns of trunk accelerations and shank/ foot sagittal angular velocity, [62]. As a matter of fact, the ICs and FCs are the basis of any other gait parameter estimation, since they enable to segment the gait cycles and the principal phases within a single gait cycle. The methods thanks to which they are estimated are mainly signal-based or machine learning-based. The estimation of temporal parameters in an already segmented gait cycle precedes the estimation of the spatial ones. Once the instants or period of interest are obtained, as stated in [62], the spatial parameters can be found using one of these different approaches: direct integration, human gait

model, machine learning. The following section deals with the state of art about the estimation of spatio-temporal parameters techniques which enable to obtain the BoS or parameters related to the estimation of BoS (stride length and step width). In Figure 7.3, taken from [62], an overview of some methods to estimate spatio-temporal gait parameters is shown.

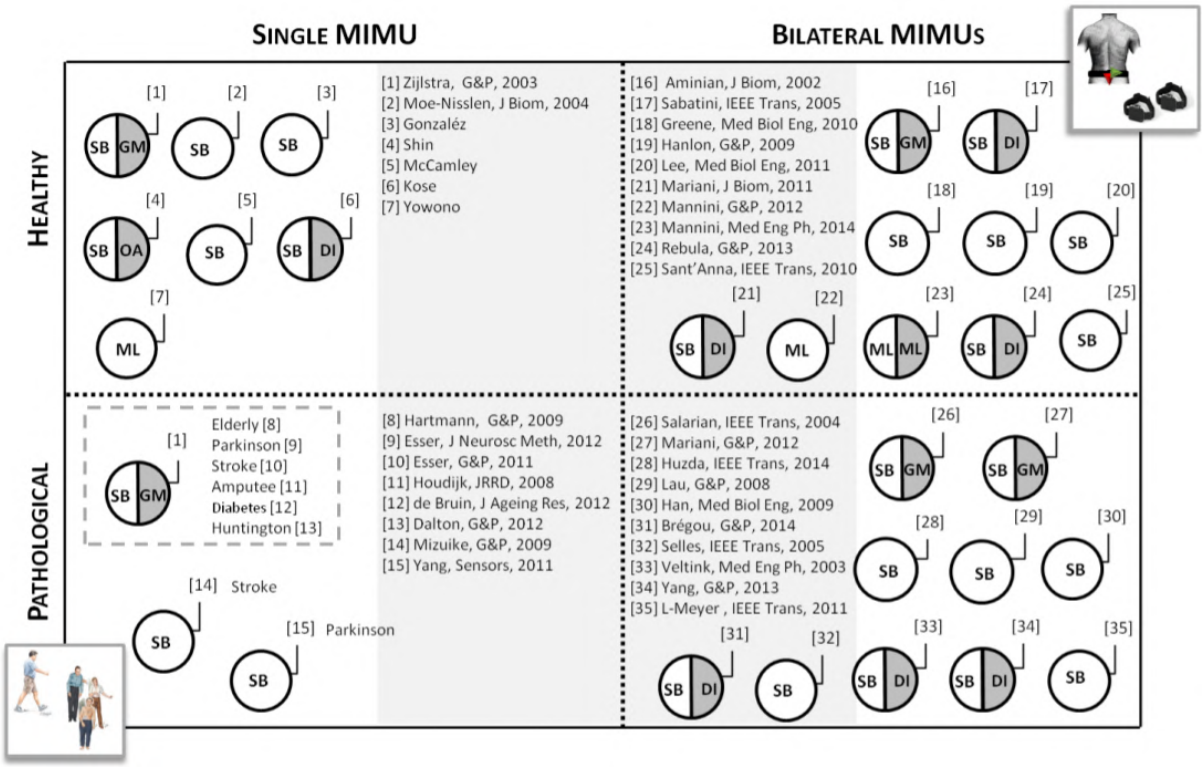

Figure 7.3: *Overview of some methods gait-spatio-temporal parameters estimation methods divided according to the number of used MIMU and the subjects on which they were tested (healthy people or pathological people), taken from [62]. 'White circles represent gait temporal parameters estimation methods (SB: signal-based analysis, ML: machine learning); grey circles represent gait spatial parameters estimation methods (DI: direct integration, GM: human gait model, ML: machine learning, OA: other approaches)' [62].*

7.1 Overview of the estimation of spatio-temporal gait parameters using MIMU

According to the position of the body on which the MIMU is attached, the sensors' signals vary significantly, both in amplitude and in frequency content. Thus the location of the wearable sensors plays a crucial role in the accuracy of the detection of ICs and FCs and the estimation of the subsequent spatial parameters. Hence, different numbers and locations of MIMUs have been studied in literature with the aim to find the most robust method to evaluate the spatio-temporal parameters. Existing single MIMU-based methods propose lower limbs, feet, shanks, thighs or waist for positioning the inertial unit [62] [27] [28] [29]. If MIMU is attached on the waist, with a single unit we can detect events of both feet but, since the distance between the sensors and the point of impact with the ground is high, the probability of properly detecting the GEs decreases. On the other hand, if a bilateral method is chosen, the same places on the legs/ feet cited above are considered. In this case, literature suggests that the most suitable place where MIMU can be fixed is the shank, which allows the sensors to be more rigidly still

and the signals to be less variable among different subjects [62].

As for the GEs identification, the signal-based methods usually consist of using thresholds (fixed or adaptive) and identification of peaks in time and/or frequency domain [62]. While machine learning methods are based on stochastic approach and the training data set influences the performances. An example of machine learning applied to gait events identification can be find in [63].

Spatial parameters estimation is closely related to the displacement estimation, which is further investigated in the following chapter. As for the human gait model based methods, the most common is the inverted pendulum, which, although, can describe quite well a healthy gait but only partially a pathological one. Another type of method to estimate the spatial parametrs is the machine learning. The main drawback of this method is that it suffers from high inter-subject variability that suggests that it requires a certain individualisation [62]. Thus, the most used technique to estimate the displacement of the MIMU is the double integration of the gravity-compensated accelerometer signals. Thus, the stride length estimation is ruled by the following equation:

$$stride\ length\ =\ \iint_{T_{c1}}^{T_{c2}} a(t)dt \tag{7.1}$$

where T_{c1} and T_{c2} are two consecutive initial contacts, a is the gravity-compensated acceleration.

However, it is not so easy as it can seems, since the drift integration errors lead to unreliable estimates, corrupting the position estimation more and more with the increasing of integration time. El-Sheimy in [64] showed how the gyro biases cause position drift proportial to the cube of the time:

$$\Delta d = \int_0^t \Delta v\ d\tau = \int_0^t (a\Delta\theta)d\tau = \int_0^t (\frac{1}{2}a\Delta\omega\tau^2)d\tau = \frac{1}{6}a\Delta\omega t^3 \tag{7.2}$$

where $\Delta\omega$ is the gyro bias, $\Delta\theta$ the angular rate error, Δv the velocity error, and Δd the position error.

Some expedients are needed to improve the result of the double integration. First of all the repeatability of the gait cycles is exploited to reduce the integration to a single gait cycle. It follows that the values of velocity at the initial instants of first integration of accelerations must be known.
The cyclical nature of gait helps also in the common technique of the zero velocity update (ZUPT), which imposes to zero the velocity during every foot flat phase of the considered foot [52]. Thus the velocity can be initialise to zero if the boundary instants of integration of the acceleration are within two consecutive stance phases.
Furthermore some de-drifting functions can be implemented to counteract to the drift [56]. Indeed, the drift can be attenuated through interpolation methods subtracting to the velocity and position curves their linear interpolations or a sigmoidal curves. This is carried out as follows, for example with the linear case:

$$v\,(t) = v\,(t) - \frac{t - t_s}{t_e - t_s} v\,(t_e) \tag{7.3}$$

$$x\,(t) = x\,(t) - \frac{t - t_s}{t_e - t_s} x\,(t_e) \tag{7.4}$$

Where t is comprised between t_s and t_e, which limit the time interval that we want to consider, such as the period between two subsequent initial contacts with the ground.
The last method to limit the drift error is the smoother-based trajectory estimation, which

consists of smoothing the integrating process with a backward update [57], thus it cannot be implemented in on-line application.

Since a MIMU allows to know the orienatation of a rigid body with respect to a global reference with a not fixed origin, it is not able to correlate the two feet. Thus MIMUS cannot provide the step width parameter. This issue can be overcome adding sensors which measure the IFD. Weenk *et al.* [17] presented a method to evaluate the step length and width through the use of the MIMU and US sensors, which are needed to find the relative distance of the feet. The MIMUs are positioned on the metatarsal part of the feet and the ultrasound receiver and transmitter on the internal upper limit of the forefeet. In this case the previous definitions of Huxham *et al.* [30] are taken into account, but the points considered in the measurement of the distances are not the centers of heels but the points where the US sensors are, as Figure 7.4 shows.

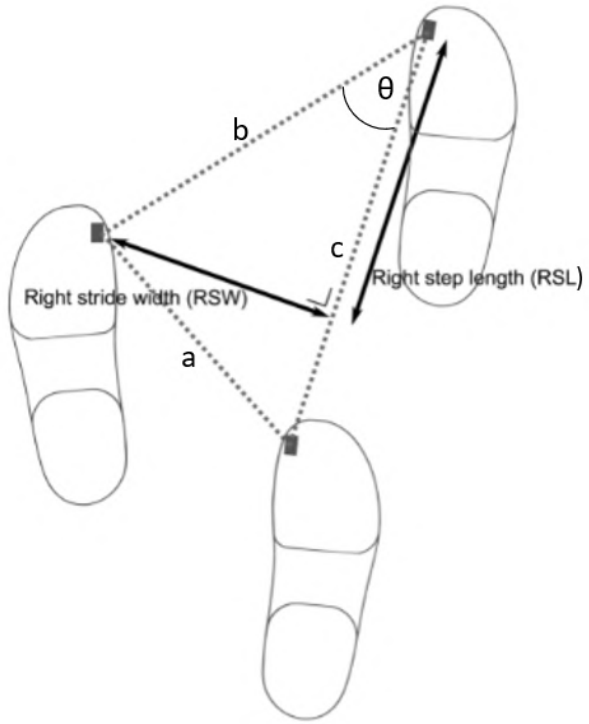

Figure 7.4: *Configuration of stride width and step length in Weenk et al. study, adapted from [17]. The distances are calculated from the positions of ultrasound transducers during stance phase.*

Considering in Figure 7.4 a, b (which are distances of the same point in both feet at the initial contacts), c (stride length), and θ the equations of step width and step length are the following:

$$step\ length\ (SL) = \ b\ cos\theta = \ \frac{b^2 + c^2 - a^2}{2c} \tag{7.5}$$

$$stride\ width\ (SW) = \ \sqrt{b^2 - SL^2} \tag{7.6}$$

Part II

Implemented methods

Chapter 8

Experimental setup and workflow of the implemented methods

The estimation of the BoS requires information which is obtained in different steps. The instrumentation consists of a MIMU and two IR ToF sensors attached on the internal lateral side of a single foot, as illustrated in Figure 8.1. The positiong of these sensors to estimate the IFD is based on the experimental setup proposed by Bertuletti *et al.* [45]: the DSs must not be positioned too close to the ground to avoid that the non-instrumented foot is not well detected in case of high clearence of the subject's instrumented foot. The measurement range of detected distances should be set properly: it has to be set high enough to consider a significant external foot rotation, but the higher the range the lower the resolution and the lower the maximum possible output data rate [45]. Therefore the range distance is set to 0-200 mm and the sampling frequency is 50 Hz. The MIMU used in this experimental setup is the one of the multi-sensor system called INertial module with DIstance Sensors and Pressure insoles (INDIP), which integrates an inertial module, up to two distance sensors and up to one pressure insole [66]. The INDIP MIMU has the following technical specifications: 3D accelerometer range is up to ±16 g, 3D gyroscope range is up to ± 2000°/s, 3D magnetometer range is up to ±50 Gauss. The output data rate range is 100 Hz. More information can be found in the datasheet [66].
While the subject is walking, the MIMU records the accelerometer, gyroscope and magnetometer data and the DSs record the distances from the opposite foot when the feet face to each other. In a gait cycle, a foot passes in front of the other twice. This estimation of the BoS is done when the non-instrumented foot is in stance and the instrumented foot is in swing phase. Thus, one estimate is carried out at each gait cycle.

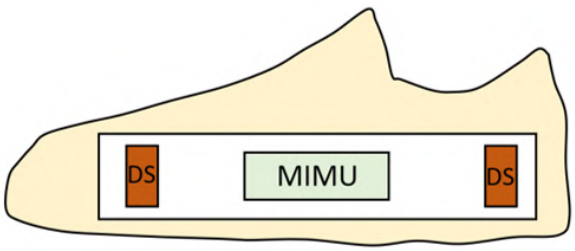

Figure 8.1: *Configuration of the instrumentation setup. A MIMU and two distance sensors (DS) are attached on the same support on the lateral internal side of a single foot.*

To calculate the area of support, the position of both subject's feet must be known and

described with the same coordinate system. Thus, a global reference system has to be defined at every stride of the instrumented foot. Then the estimation of the orientation and displacement from this chosen origin of the instrumented foot must be obtained. To provide a reliable position, the accelerometer data cannot be directly integrated, but the gravity acceleration must be removed and the accelerations must be filtered. The integration is carried out adopting strategies to reduce the drift.
The DS data are fitted to create a linear model of the detected surface of the non-intrumented foot. This model is placed in 3D space with respect to a common coordinate system knowing the orientation and position of the DSs while they are 'scanning'.
Once both feet are modeled and described in a common frame, the spatial gait parameters can be obtained.
In the next chapters the implemented methods for:

1. orientation estimation,
2. position estimation,
3. identification of a common coordinate system

are described.

Chapter 9

Sensor fusion algorithm

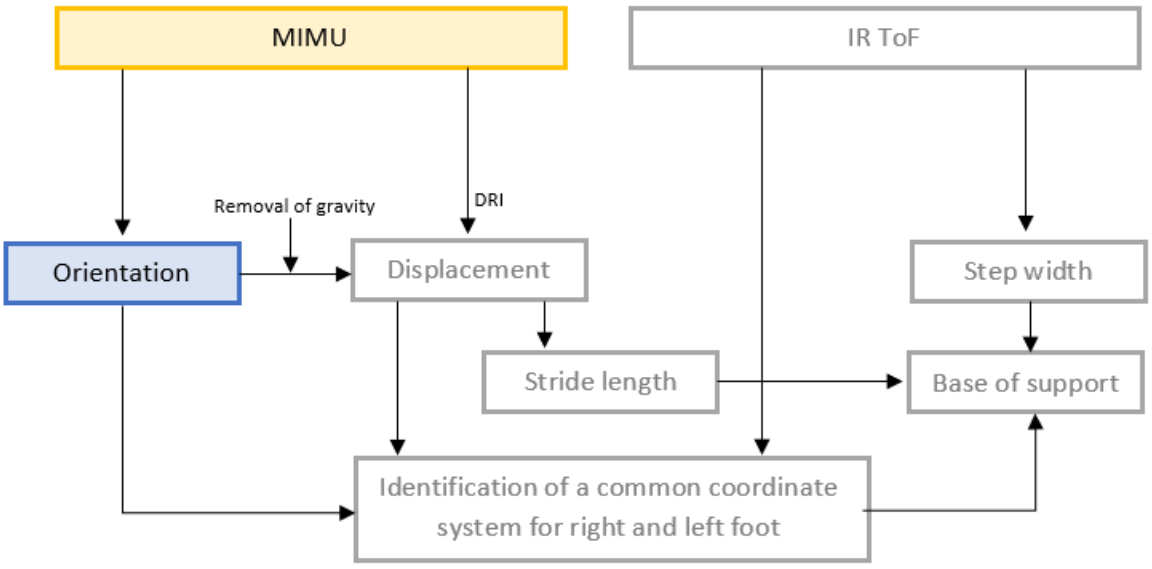

Figure 9.1: *Overview of the thesis: the necessary data (yellow) and the implemented method (blue) in this chapter are colored.*

Because of the advantages described in Section 5.3, the chosen way to represent the orientation are the quaternions. From Section 6.1.3, comparing the complementary filters (CFs) and the Kalman filters (KFs), it emerges that CFs are preferable if the application requires easier implementation, a lower computational cost and a fewer number of parameters.
The article on which the implementation of this algorithm is based is the one presented by Madgwick in 2010, [36]. This is a complementary quaternion-based orientation filter applicable both on IMUs and also on MIMUs, giving the possibility to choose to estimate the orientation only with the accelerometer and gyroscope or also with the help of the magnetometer. The incorporation of the magnetometer signal leads to merge possible magnetic distortions but, on the other hand, also to a gyroscope bias drift compensation. As declared in cited above reference article [36], this filter is effective also at low rate, e.g. 10 Hz, and allows to adjust only one (in the case of IMU data) or two (in the case of MIMU data) parameters. Since the usual method to choose the parameters of a sensor fusion algorithm is the 'trials and errors', having a

few parameters to set is a great advantage. The implication of the low computational cost and the possibility to work also at low sampling rates are that the supplied power can be reduced and this is a great strength for a wearable and lightweight motion tracking system that must function for extended periods of time and also for real-time applications.

9.1 Madgwick's Filter

The base idea to find the orientation from the (M)IMU data consists of integrating the angular rate and then correcting this value thanks to the readings from accelerometer (and magnetometer). More specifically, the accelerometer and magnetometer data are used in an 'optimised gradient-descent algorithm to compute the direction of the gyroscope measurement error as a quaternion derivative' [36]. The main parameter (β) is related to the zero mean gyroscope measurement errors. As a matter of fact, it establishes how much weight to give to the information of the Earth's vectors (gravity and magnetic field), being a multiplicative factor of the gyroscope measurement error. Hence the higher β the higher the weight given to accelerometer and magnetometer signals.

The final estimate, which describes the orientation of the Earth's coordinate system (ECS) with respect to the MIMU coordinate system that coincides with the LCS, merges together two quaternion found separately: one is obtained from the angular velocity provided by the gyroscope and the other one from the accelerometer and magnetometer signals. The main passages are the following:

1. Quaternion estimate from the integration of angular rate:

$$ {}^{E}_{L}\hat{q}_{\omega,t} = ({}^{E}_{L}\hat{q}_{est,t-1} + \frac{1}{2}{}^{E}_{L}\hat{q}_{est,t-1} \otimes \omega_t^L)\triangle t \tag{9.1} $$

   where ω_t^L is the angular measurement at time t, $\triangle t$ is the sampling period and ${}^{E}_{L}\hat{q}_{est,t-1}$ is the previous estimate of orientation.

2. Optimal estimate of the Earth's vector-based quaternion, obtained aligning the gravity and the magnetic field expressed in ECS with their observations referred to LCS and minimising an objective function that is defined as the difference between the components of the Earth's vector expressed in LCS and the ones rotated in ECS. The objective function is defined as the intersection of two objective functions derived from accelerometer and magnetometer signals separately.

$$ \nabla f = {J_{g,b}}^T({}^{E}_{L}\hat{q}_{est,t-1}, \hat{b}^E) f_{g,b}({}^{E}_{L}\hat{q}_{est,t-1}, \hat{a}^L, \hat{b}^E, \hat{m}^L) \tag{9.2} $$

   where f is the objective funciton, $\hat{m}^L$ and $\hat{a}^L$ stands for $\hat{s}^L$, while $\hat{b}^E$ for $\hat{d}^E$. Indeed $\hat{m}^L$ is the normalised magnetometer measurement expressed in LCS, $\hat{a}^L$ is the normalised accelerometer measurement, $\hat{b}^E$ is the magnetic field in ECS.

3. Sensor fusion step in which the two previous estimates are merged in a weighted mean. The final orientation estimate is the following:

$$ {}^{E}_{L}\hat{q}_{est,t} = {}^{E}_{L}\hat{q}_{est,t-1} + \triangle t({}^{E}_{L}\dot{q}_{\omega,t} - \beta\frac{\nabla f}{||\nabla f||}) \tag{9.3} $$

   and β is the factor related to the divergence rate of the quaternion coming from the integration of the angular rate, so the gyroscope measurement errors with null mean.

4. Magnetic distortion compensation limiting the magnetic disturbances to the heading component.

5. Gyroscope bias drift compensation obtaining the bias estimate low-filtering the error in the rate of change of orientation.

The complete mathematical formulation from the sensor data to the orientation estimate can be found in Appendix A.

The derivation of the filter has the limit to initially assume that accelerometer and magnetometer measure only the gravity and the Earth's magnetic field. However external accelerations and magnetic distortions corrupt this hypothesis. Although a method for compensation of gyroscope bias and magnetic inclination errors are implemented. In particular, the magnetic distortion compensation eliminates the need of a priori knowledge of the direction of the magnetic field, which was predefined by the designer [55]. The key advantages of the adoption of this filter are the need of tuning only one parameter (β), defined by gyroscope measurement errors, and the significant reduction of computational load (due to the adoption of an analytically derived Jacobian matrix for the computation of errors).

9.2 Quaternion initialisation

The algorithm described above is based on a loop in which for every time step a new orientation is calculated from the one of the previous step. Hence it is important how to choose the first initial quaternion, which let the loop to begin. This choice influences the period of initial convergence of the filter: the higher the difference between the initialized value and the real orientation, the higher the period of convergence in which the estimated orientation cannot be considered, because it is unreliable. To not initialise the quaternion with an arbitrary one, in this study we want to implement a further sensor fusion algorithm that provides the initial quaternion q_0. A reasonable assumption is that initially the body portion on which the MIMU is attached is stationary, before the motion. This hypothesis leads to the adoption of a method for quaternion initialization which must not consider the gyroscope data. Indeed, if the gyroscope is static it cannot detect any relative difference of orientation through angular velocity. However, in static conditions, accelerometer and magnetometer provide useful information for the orientation estimation through the Earth's vectors sensing. Furthemore, it can happen that also the magnetometer could be an unreliable source of information because of the ferromagnetic disturbances. Therefore, a method to provide a first orientation estimate accurate enough to allow a short convergence must be implemented considering accelerometer and magnetometer data or, in case, only the accelerometer.
Valenti *et al.* in 2015 [35] proposed a sensor fusion algorithm considering only the Earth-field observations. The algorithm considers two independent fields, gravity and magnetic field, and is based on finding the inverse rotation that enables the measured quantities, accelerometer signal a^L and magnetometer signal m^L, expressed in LCS, to be referred to ECS, where the x axis is aligned with the magnetic north and the z axis with the gravity. The resolution equations are the following:

$$R({}^E_L q)\ a^L = \ g^E \tag{9.4}$$

$$R({}^E_L q)\ m^L = \ h^E \tag{9.5}$$

These equations mathematically express the fundamental idea of rotating the sensor vectors readings into the ECS. The system, however, is overdetermined so it cannot be solved. With

some expedients, we can impose predefined global components so that the rotation matrix which performs the transformation becomes known, and so the quaternion too. A constraint must be imposed to reduce the degree of freedom: the magnetic reading h^E is forced to lie on the half plane ${}^E\Pi_{zx^+}$ containing the points of xz plane with non-negative x.

$$R({}^E_L q)\ m^L = \ h^E \ \in {}^E\Pi_{zx^+} \tag{9.6}$$

Thus ${}^E_L q$ can be decomposed into two quaternions, q_{acc} and q_{mag}, where the first produces a rotation from the sensor frame to the horizontal plane of ECS and the second produces a rotation around the z axis of ECS.

$$R\left({}^S_E q\right) = \ R(q_{acc})\ R(q_{mag}) \tag{9.7}$$

In other words, observing the gravity and magnetic vectors in the two reference frames allows us to find the quaternions that perform the transformation between the two representations, q_{acc} and q_{mag} respectively.

$$R({}^L_E q)\ g^E = \ a^L \tag{9.8}$$

Since the gravity has only z component, the expression can be simply as follows:

$$R(q_{acc})\ \begin{bmatrix}0 & 0 & 1\end{bmatrix}^T = \begin{bmatrix}a_x & a_y & a_z\end{bmatrix}^T \tag{9.9}$$

Thanks to the previous equation, q_{acc} is found and used to rotate m^L.

$$R^T(q_{acc})\ m^L = \ h^E \tag{9.10}$$

Assuming that h^E has non-null components only in x and z, the rotation derived from this quaternion does not affect also pitch and roll components. Hence, in presence of magnetic disturbances, their effect is limited in the heading, not corrupting the roll and picth.

$$R^T(q_{mag})\ \begin{bmatrix}h_x & h_y & h_z\end{bmatrix}^T = \begin{bmatrix}\sqrt{h_x^2 + h_y^2} & 0 & h_z\end{bmatrix}^T \tag{9.11}$$

Once formulations for both quaternions are chosen among the possible existing solutions in order to not introduce any singularity problem, the initial quaternion of the algorithm described in the previous section is obtained through quaternion product of the two quaternion coming from accelerometer and magnetometer respectively.

$${}^L_E q = q_{acc} \ \otimes \ q_{mag} \tag{9.12}$$

While Madgwick's filter uses the quaternions which provide the rotation from LCS to ECS, while Valenti's discussed algorithm treats the inverse quaternion (from ECS to LCS). It follows that the above found quaternion must be conjugated (${}^L_E q^*$) before it feeds Madgwick's first iteration. If there are not ferromagnetic disturbances, q_0 is the quaterion obtained in Equation 9.12; vice versa, if they are present q_0 is only q_{acc}.

9.3 Optimization of the parameter of the filter

Once implemented the complementary fiter, it is optimised to improve the accuracy of orientation estimation having the purpose of estimating the spatial gait parameters. There are certain situations in which one or many sensors of MIMU are less reliable. In a dynamic system, the accelerometer is not able to distinguish from an external acceleration and the gravity, while, in presence of magnetic disturbances, the Earth's magnetic field is not properly detected. Thus the

base idea for improving the performance of the sensor fusion algorithm is to give more weight to the most reliable data from MIMU in a certain time. Indeed, in static condition, the gyroscope does not bring any useful information, while the accelerometer measures only the gravity and no other accelerations. If there are important ferromagnetic disturbances, the magnetometer is totally not reliable. So some checks are added to find out if there is a condition of statics or of magnetic disturbance or both. The implemented method to segment the signal in intervals of different features is based on thresholds and peaks detection. The thresholds that have to be set are: one for describing the maximum acceptable difference between the gravity acceleration value and the norm of the accelerometers readings to define the state as statics, the other for describing the maximum acceptable difference between the theoretical unitary norm and the actual one of the magnetometer readings to define the state as non-disturbed. So we can define four possible conditions:

- The instrumented foot is in motion and there are no ferromagnetic disturbances and so the algorithm maintains a unique the filter gain β and considers all the MIMU sensor data;
- The instrumented foot is stationary and there are no ferromagnetic disturbances and so β is increased to weight more data from the accelerometer and the magnetometer;
- The instrumented foot is in motion and there are ferromagnetic disturbances and so the magnetometer information is deleted, considering only the gyroscope and the accelerometer;
- The instrumented foot is stationary and there are ferromagnetic disturbances and so β is increased to weight more the accelerometer data, but the magnetometer readings are excluded as in the previous point.

The thresholds can be difficult to be set since they closely depend on the experimental conditions, so in this study also the envelopes of the MIMU data have been considered. Wanting to do the derivative of the signals, a strict low-pass filter of the absolute values is adopted and the thresholds are set according to this less variable data. Anyway the cyclical nature of gait can be exploited and so in the interval of foot flat period, in which ZUPT can be applied, a higher filer gain is adopted. The definition of the optimal value of β is achieved by trials and errors.

9.4 Comparison with a reference

Once estimated the orientation of the rigid body, we have to test if the results are acceptable through the comparison with a gold standard. Usually it is the orientation derived from SP. Putting three non collinear markers of the SP aligned with the MIMU plane, it is guaranteed that the local coordinate systems are the same, while the globals do not coincide (G_1 and G_2). The quaternions, thus, have to be rotated to another system that has to be equal for the SP and the orientation estimated with the algorithm descripted above. It is exploited the fact that the local coordinate systems are aligned to refer the quaternions to the one of the first time frame. In this study, the performance of the orientation estimation is not tested with SP, since it was not the aim of the thesis and the implemented algorithms are based on filters that have been proved to work in gait analysis [55][35]. Anyway a test to define if the orientation estimation is good enough for the application on this study is needed. As it can be seen in Part III, the orientation of static conditions is evaluated to check that it was always constant. The algorithms are used on the sensor data coming from Xsens MIMU (MTi and MTx User Manual and Technical Documentation- Xsens Technologies B.V., [43]). Xsens manufacturer

provides quaternions based on a Kalman filter and this orientation is used as reference (ref) for a comparison, referring both orientations to their first frame.

$$ {}^{MIMU,1}_{MIMU,t}q = {}_{MIMU,1}{}^{G_1}q^* \otimes {}_{MIMU,t}{}^{G_1}q \tag{9.13} $$

$$ {}^{ref,1}_{ref,t}q = {}_{ref,1}{}^{G_2}q^* \otimes {}_{ref,t}{}^{G_2}q \tag{9.14} $$

Once expressed both the quaternions in the same reference coordinate system, the orientations can be compared.

Chapter 10

Position estimation

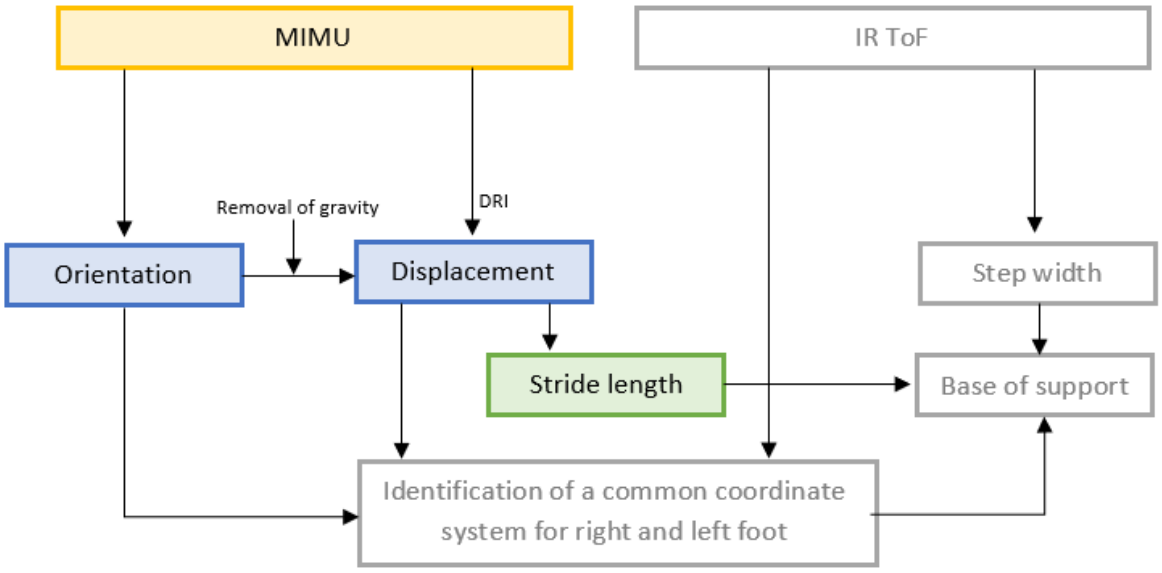

Figure 10.1: *Overview of the thesis: the necessary data (yellow), the implemented method (blue) and the obtainable results (green) in this chapter are colored.*

To describe in 3D space the position of both feet with respect to the same reference system, firstly the displacement estimation from MIMU data must be done and then the non-instrumented foot can be positioned knowing the inter feet distance and the positions of the distance sensors when they see the foot. So the displacement estimation is crucial for the BoS estimate.

10.1 Displacement estimation from MIMU accelerations

A reason why MIMUs are used to estimate gait spatial parameters is that they can exploit the accelerometer readings and, through double integration over time, the position can be found. The accelerometer signals depend on both external accelerations and the gravity. So the latter has to be removed. To do this, an estimation of the orientation of the sensors with respect to the global frame is needed [56]. This entire procedure is complicated by a drift which is commonly present when integrating the accelerometer signals, mostly due to thermal–mechanical and electronic noise, which leads to an error in the displacement estimations nonlinearly related to the

integration time [23] [64]. Since the drift increases with time, it is useful to segment the signal to not integrate it all over its length. The detrimental effects of the drift are, thus, reduced by exploiting the cyclical nature of gait, so it is preferable that the interval of integration time is reduced, for example to a gait cycle. On the other hand, this requires the detection in the cycle of an instant of known velocity to be used as initial condition in the integration of the acceleration [23].

10.1.1 Gravity compensation

The first step is to remove the gravity from the acceleration components. Since the accelerometer signals are referred to the sensor coordinate system, they have to be expressed with respect to the Earth's reference so that we can subtract the vector gravity knowing its components. For example the gravity is easily described as a vector with 9.81 as z component, in a global coordinate system with the z vertical axis pointing downwards. The accelerometric data, thus, are rotated with the orientation quaternions, found with the algorithm described above, to be referred to the global reference.

$$A^G = R({}^L_G q^*)a^L + \begin{bmatrix} 0 & 0 & 9.81 \end{bmatrix} \tag{10.1}$$

where A^G is the gravity-free acceleration referred to the global frame and a^L is the accelerometric readings referred to the local coordinate system. It is preferable to describe the position of the instrumented foot with respect to the first instants of every stride in the BoS estimate application. So in the BoS estimation A^G is re-rotated in the MIMU frame at a certain flat foot instant.

10.1.2 Acceleration filtering

A^G contains biases and noise that have to be removed. The easiest way to do that is the removal of the mean. In this thesis both the mean removal and an optimal filter are implememted. Zok *et al.* [51] presented a method to filter the accelerations in which the acceleration signals (after the subtraction of the gravity) are high pass filtered in a filter that chooses the cut off frequency according to the sensor data. Thus, to choose the optimal cut off frequency, the effect of different frequencies is evaluated. The investigated range of frequencies must exclude the range of movement. For every chosen frequency, the accelerations (already gravity-compensated) are filtered with Butterworth filter, then the filtered signals are integrated to obtain the velocities. The difference between consecutive samples of velocities is the information used to establish which cut off frequency is the most suitable: minimizing the velocity difference for each step, three frequencies (one for each axis) are chosen. The filtered gravity-compensated accelerations are A^G_f.

10.1.3 Double integration

A^G_f is double integrated to obtain displacements:

$$v(t) = v_0 + \int_{t_b}^{t} A^G_f(\tau)\ d\tau \tag{10.2}$$

$$x\,(t) = x_0 + \int_{t_b}^{t} v\,(\tau)\,d\tau \tag{10.3}$$

However, these estimates are corrupted by a drift. Some experiments are performed to evaluate the accuracy of the direct double integration and reported in Chapter 13. To limit the drift three adjustments are added:

- the acceleration is not integrated all over the entire period of recording but only over a limited interval (a gait cycle), whose limits are detected by thresholds on accelerometric and gyroscopic data;
- the velocity is updated imposing that it has to be zero during each interval of flat foot period. This third adjustment is known as zero velocity update (ZUPT) and consists in detecting the epochs where the velocity can be forced to be zero to reduce the error in the position [52].
- all the integrations are perfomed considering the actual sampling interval between every couple of consecutive samples. This is done to reduce an error which would be occur if the sampling frequency would not be exactly constant.

10.1.4 Zero-Velocity Update

The zero-velocity assumption is based on the fact that if we assume negligible the foot roll during stance in level walking from the outer edge to the inner edge [58] and the difference of the movements of the forefoot and heel both in shape and time [59], the velocity can be set to zero at the beginning of every integration interval [60], [61], [56]. As reported in [23], the foot velocity can be assumed to be zero throughout the stance phase or during a portion of it or only in a specific instant. As [52] reported, there are many possible detectors of the epoches in which the velocity can be imposed to zero: the acceleration-moving variance detector, the acceleration-magnitude detector, the stance hypothesis optimal detection detector, and angular rate energy (ARE) detector.

The type of detector used in this thesis is ARE, based on [52]. Only the energy of the gyroscope signal is taken into account, since it contains a fundamental information to establish if the MIMU is stationary or not. The equation on which this method is based is the following:

$$T = \frac{1}{N} \sum_{j} ||\omega_j||^2 \leq \ \gamma \tag{10.4}$$

where $||\omega||$ is the norm of angular velocity. T is a function that has to be compared with a threshold γ: if it is below the threshold, then the ZUPT can be applied.

10.1.5 Identification of integration instants and gait events

The identification of the integration instants depends on the identification of significative events during the gait cycle. Within the ZUPT intervals the instants of integration (FF_i) can be selected. Indeed two consecutive flat-foot phases are separate from a gait cycle and guarantee that the velocity is null within them. Therefore, the beginning and final instants of integration are defined in this thesis as the instants within two consecutive ZUPT interval in which the magnitude of the acceleration readings is closest to the gravity. So they are instants in which there is the highest probability that the instrumented foot is actually stationary. The sensibility to the choice of the integration instants is analysed in a preliminary experiment, which can be found in Chapter 13.

Furthermore, to check if the BoS is calculated considering the feet in the right phases of gait cycle, the identification of gait events to segment the gait cycle is useful. To identify them, first of all an algorithm which divides the static from the dynamic moments is needed. Setting some thresholds on the accelerometric and gyroscopic signals or their envelopes, we can separate the periods when the foot is stationary and the ones when it is moving. Distinguishing between static and dynamic phases is only a preliminary step. For an accurate detection of GEs, the method proposed by Trojaniello et al [53] can be followed. The algorithm begins with the identification of swing and stance phases and then finds the instants of initial and final contacts of the feet with the ground. The detection starts with finding the swing phase, knowing that:

- the maximum angular rate is at half of the swing and the swing interval is defined as the period with angular rate around the vertical axis that is equal to or higher than the 20% of the maximum;
- the minimal swing interval is set to 100 ms;
- two following swing interval of the same foot is distant at least 200 ms;
- if the angular rate around the vertical axis crosses the threshold many times in a restricted period, thus we consider only the first and final crosses.

The stance phase is considered to be the interval between two consecutive swing phases. To avoid error induced by the high variability of the MIMU signals, the minimum duration of the static detected phase is set to be 50 ms. Furthermore, a check on the standard deviation in this interval is evaluated, in case, to modify and enlarge the phase. The intervals between the swing and the stance of the same foot are called interval of initial contact and final contact (T_{IC} and T_{FC}) and they are the periods where we search for the actual instants of IC and FC with the ground. IC is also definable as heel strike (HS) and FC coincides with the toe-off (TO). The IC is defined as the instant with the minimum value of angular rate around the vertical axis in T_{IC} before the time of the local maximum of acceleration. The FC is defined as the moment with the minimum of acceleration in T_{FC} before the last local maximum of acceleration. In Figure 10.2 the gait events detection described above is graphically explained in an example.

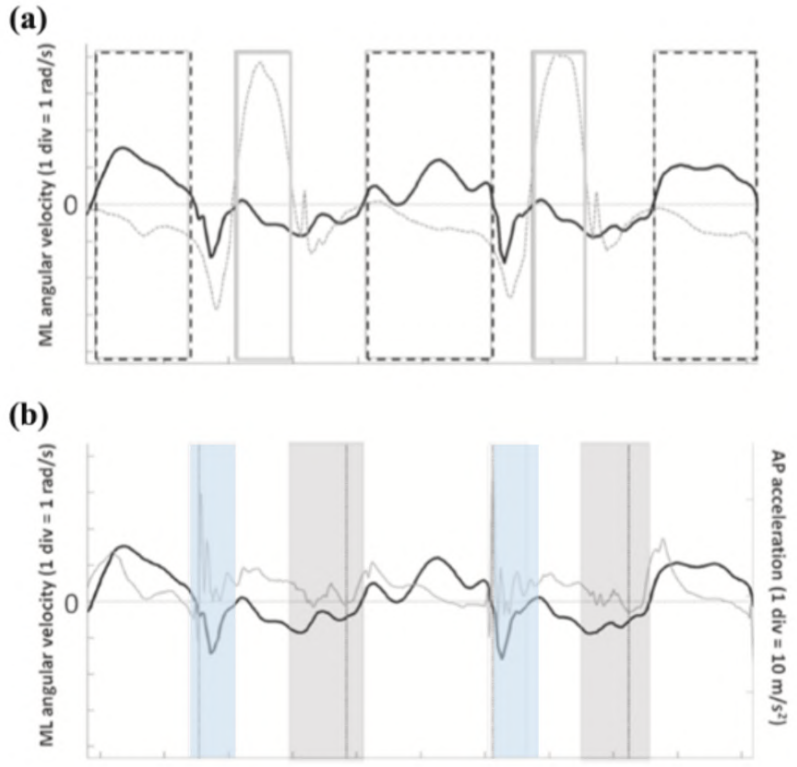

Figure 10.2: *Gait events detection, taken from [53]. Figures represent the mediolateral angular velocity and the anteroposterior acceleration. (a) Rectangular frames represent trusted swing (dotted line) and trusted stance (solid line) intervals. (b) Colored boxes represent time intervals for the IC (light blue) and FC (gray) search; dotted vertical lines represent the GEs timings.*

10.1.6 Direct and Reverse Integration

The drift problem in the estimation of displacement could be heavily detrimental. Due to this drift, the position estimate at the end of the considered interval is usually overestimated, so an improvement in the accuracy of the double integration is required. The velocity is zero at the begin of the integration and at the end of it. Therefore, this can be exploited to impose non only an initial but also a final condition of integration. The implemented method is based on the one proposed by Zok *et al.* [51]. It performs not only the direct integration but also a time-reversed integration (named reverse integration). Thus this integration technique is called Direct and Reverse Integration (DRI). The acceleration signals used in this step are gravity-compensated and filtered. The DRI is made up of three phases:

1. the direct double integration of the signals ($d(t)$);
2. the reverse double integration ($r(t)$), through which the original signal is integrated reversely in time using the final conditions as initial ones;
3. weighting, when the two previously obtained signals are sum up weighted by a time-dependent function $w(t)$ which varies between 0 and 1.

Thus the final integrated displacements are:

$$DRI(t) = r(t)w(t) + d(t)(1 - w(t)) \tag{10.5}$$

where w is the weighting function which is forced to vary from 0 to 1 as follows:

$$w(t) = \frac{s(t) - s(t_b)}{s(t_e) - s(t_b)} \tag{10.6}$$

$s(t)$ is a function chosen so that the corresponding value of the middle of time interval t_e-t_b is 0.5 and is symmetric with respect to that central point such that the weight is evenly distributed between $d(t)$ and $r(t)$. This should enable that the most reliable values (the closer to the beginning of the time interval of integration where the drift is lower) are more weighted. The simplest $s(t)$ is linear, $s(t) = t$, but in [52] it is shown that a s-shaped function, as the one in Equation 10.7, improves the result.

$$s(t) = atan(\frac{2t - t_e}{2\beta t_e}) \tag{10.7}$$

where β controls the steepness of the curve. The suggested value by the author is 0.1, trade-off between the discontinuous step function occurring for β similar to zero and the quasi-linear function relating to β higher than 1.

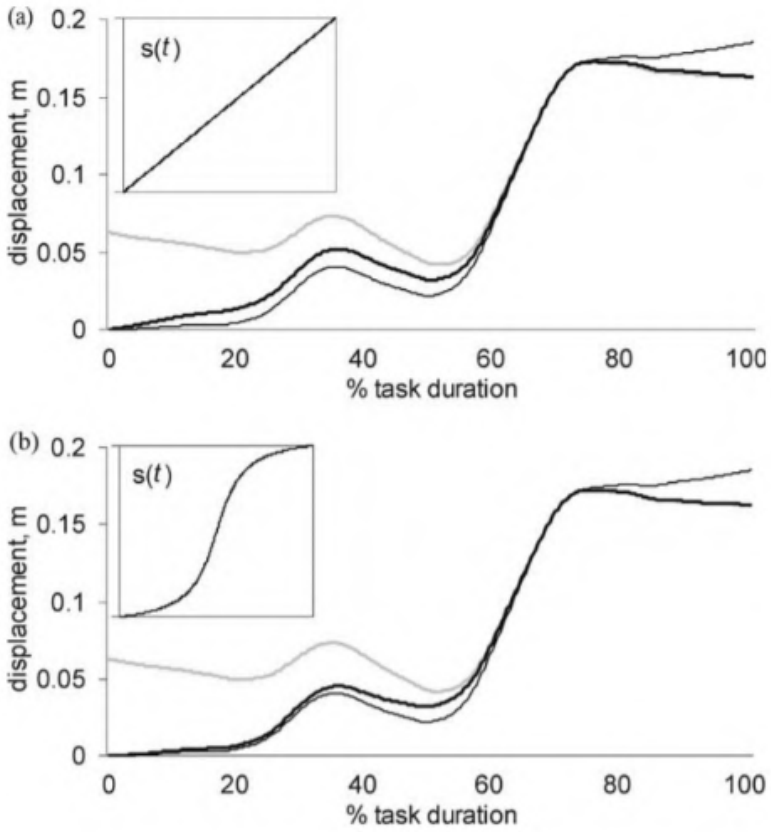

Figure 10.3: *This figure, taken from [52], shows the curves of displacements of the center of mass. The thin black line derives from direct double integration, the grey line from the reverse double integration and the thick black line from the weigthed sum of them. A) the weigh function is linear, b) the weigth function is 's-shaped'.*

10.1.7 Stride Length estimation

In conclusion, the stride length (SL) is achieved by the integration of the velocity between two flat-foot phases:

$$SL = \int_{FF_i}^{FF_{i+1}} v_{DRI}(t)\, dt \tag{10.8}$$

where v_{DRI} is the velocity obtained from accelerations with the DRI and FF_i and FF_{i+1} are the instants of two consecutive ZUPT intervals with the acceleration magnitude closest to the gravity.

Chapter 11

Method for reconstructing the length of a rigid body using infrared time-of-flight sensors

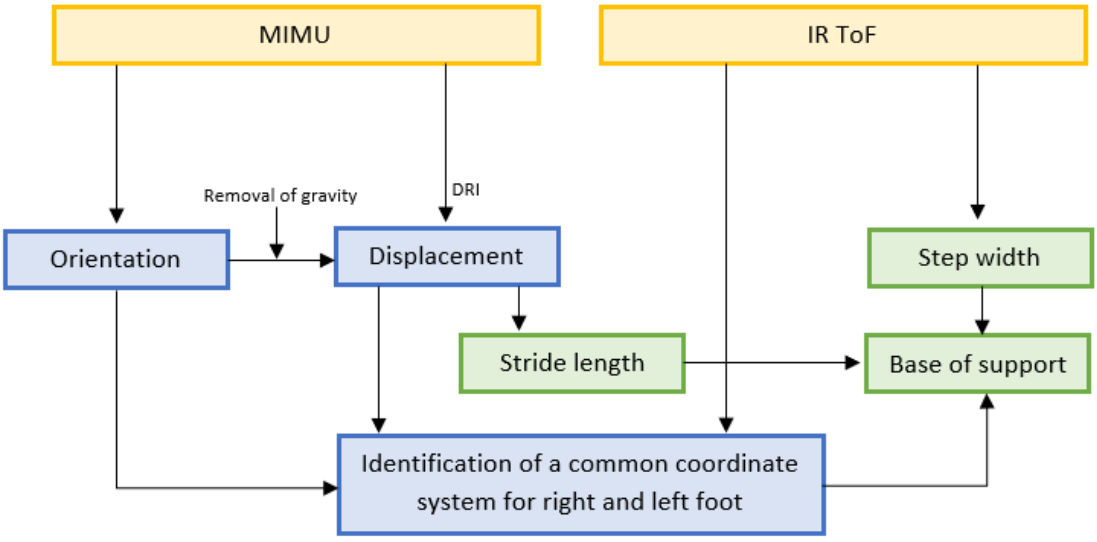

Figure 11.1: *Overview of the thesis: the necessary data (yellow), the necessary implemented methods (blue) and the obtainable results (green) in this chapter are colored.*

To estimate the inter-feet distances and so the step width, the infrared time-of-flight (IR ToF) sensors are the main source of information. It follows that also in the estimation of the base of support they have an important role. What we have to investigate is a method for modelling and positioning in a global coordinate system the body that the distance sensors detect.

11.1 Infrared time-of-flight working principle

To briefly describe the IR ToF sensor functioning, an explanation of its working principle is provided. Detailed information are reported in the datashhet of VL6180X proximity, gesture

and ambient light sensing module [65].
IR ToF sensors measure the time an electromagnetic wave needs to cover a distance, or better a phase shift. As [6] reported, the method through which the distance is estimated is based on the measurement of the phase shift ϕ between the radiated and the reflected IR waves.

$$s(t) = sin(2\pi ft) \tag{11.1}$$

$$r(t) = R\ sin(2\pi ft - \phi) = R\ sin(2\pi f(t - \frac{2d}{c})) \tag{11.2}$$

where s(t) is the radiated wave, r(t) is the reflected wave, f is the frequency of both s(t) and r(t) signals that can be modulated, R is the reflection coefficient, d is the distance between the emitter and the target, c is the light speed.
Thanks to a phase comparator circuit the phase ϕ can be measured and used to obtain the distance d, which is the wanted output, through the following equation:

$$d = \frac{c}{4\pi f}\phi \tag{11.3}$$

The range of the distance measured data can be at the maximum of 0-600 mm. The IR waves are emitted and received through two different holes that create an illumination cone and a view cone. The latter is of 25°, as reported in [65]. The maximum sampling frequency allowed is 50 Hz, thus it is the one used in this study. Figure 11.2 illustrates the IR ToF working principle.

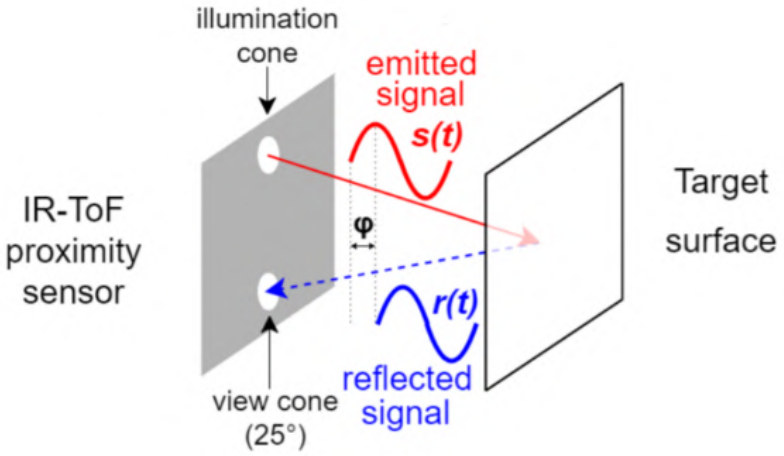

Figure 11.2: *IR ToF sensors measure the phase shift angle between the emitted (s(t)) and received (r(t)) signals to provide the distance between the sensor and the target. Taken from [6].*

11.2 Identification of a common coordinate system for the infrared wave emitter and the target surface

While the non-instrumented foot is detected by the distance sensors, it is stationary and the sensors (IR ToF and MIMU) pass in front of it with a certain velocity. Through the information of the relative distance between the feet, it is possible to refer the non-instrumented foot to a predefined global coordinate system. The reasonable assuption about the direction of the emitted IR wave is that it is perpendicular to the support on which the distance sensor is attached. In the experimental setup, it should be noticed that the distance sensors must be attached on the same rigid support of the MIMU, to satisfy the assumption that the emitted IR wave lies on a coordinate axis of the MIMU coordinate system. The main steps to do are the following:

1. The distance data are used to create vectors with an unique non-null component in the direction perpendicular to the support on which the sensors are attached. For example it is hypothised that the principal motion of the foot occurs in x direction and the non-null components are in y axis:
$$d^L = \begin{bmatrix} 0 & IRToF_{data} & 0 \end{bmatrix} \tag{11.4}$$
where $IRToF_{data}$ are the IR ToF sensor recordings and d^L is a matrix cointaing all the distance vectors expressed in the LCS.

2. The distances are rotated to be expressed in the ECS. This can be done thanks to the quaternions, provided by the sensor fusion algorithm, which describe the orientation of the MIMU in every time step.
$$d^E = {}^E R_L \; d^L \tag{11.5}$$

3. The MIMU displacement is described with respect to LCS at the first frame of the every stride of the instrumented foot, so that at the beginning of the movement the displacement is zero. Thus, the distance expressed in GCS must be re-rotated until it reaches the orientation of the LCS at FF_i instant (L_1CS).
$$d^{L_1} = {}^{L_1} R_G \; d^G + O_{L_1} \tag{11.6}$$
After the rotation, the distance sensor is expressed in a coordinate system which is aligned with L_1CS, but with the fixed origin in the origin of the global system O_G. To traslate the reference frame to the origin of L_1CS, the components of O_{L_1} are added. Now the detected points of the non-instrumented foot and the MIMU positions are expressed in the same coordinate system.

To better explain these steps, an illustration can help. Since the final aim of this thesis is the estimation of the BoS, the graphical example in Figure 11.3 shows the case in which the right foot is instrumented with a MIMU and a distance sensor and has to detect the left foot.

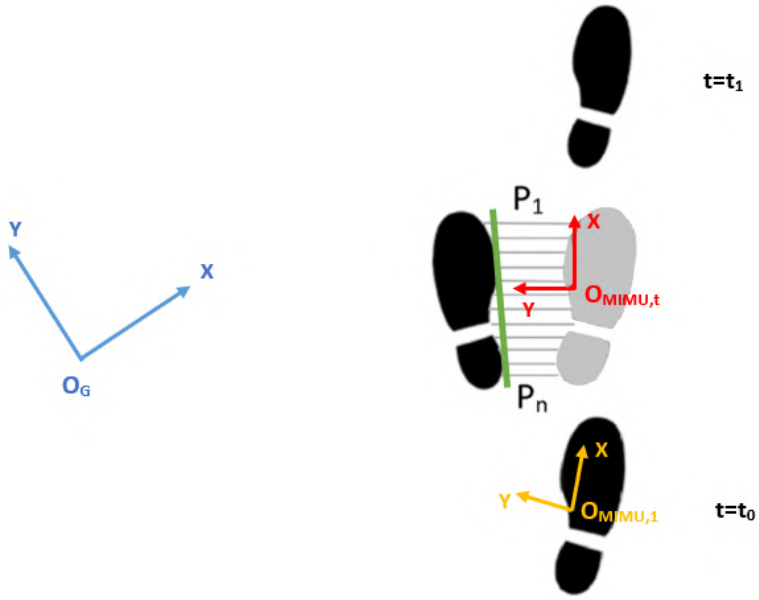

Figure 11.3: *Illustration showing the footprints in black and the moving foot during swing phase in grey. IR waves emitted by proximity sensors are represented by grey lines from P1 to Pn, the sensors coordinate frame (LCS) is figured by the red systems. The yellow coordinate system is the one of the MIMU at the first instant of the analysed stride of the right foot. The green line is the plane, perpendicular to the ground, on which the model of the lateral side of the foot lies. The blue coordinate system is GCS.*

11.2.1 Rigid body length reconstruction

Once the points detected by the distance sensors are referred to the common chosen reference coordinate systems, they must be fitted to create a model line. This line must approximate the lateral internal surface of the non-instrumented foot. Furthermore, the length of this linear model has to be equal to the length of the foot. Some preliminary experiments were performed to evaluate the accuracy of the length reconstructed knowing the velocity of the instrumented foot, the sampling frequency and the interval in which the distance sensors have non-null readinds. They can be found in Chapter 14. The most accurate method is to impose the known foot length to the model. To achieve a linear segment approximating the lateral foot surface, the following steps are followed:

1. The outliers, due to the view cone of 25° of the IR ToF sensors, are removed imposing a threshold on the distance data;

2. The center of mass (CoM) of the points detected by the DSs, p_i, is calculated:

$$CoM = \frac{1}{N}\sum_i p_i \tag{11.7}$$

3. The mean square errors minimization is used to linearly fit the data: the foot lateral side model is a line passing through the CoM of the distance dataset.

4. The actual length of the detected rigid body is imposed. To do that a local system whose x axis coincides with the model line is defined and the limits of the model segment are imposed.

In this way the green segment in Figure 11.3 and 11.4 can be expressed in reference system.

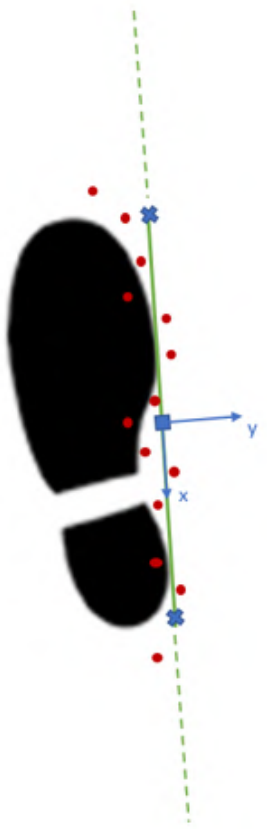

Figure 11.4: *Drawing showing the footprint of the non-instrumented foot in black, the points detected by the distance sensors in red (considering their imprecisions), the fitted line in green. The center of mass of the red points is the blue square. The blue coordinate system is used to impose the limits of the segment (blue crosses) to obtain the actual length of the foot.*

11.3 Step width and base of support estimation

Even if the feet face to each other twice in a gait cycle, the BoS can be estimated with the proposed method just after the swing of the instrumented foot, because it is necessary that the detected foot is stationary to estimate its position in the 3D space. On the other hand, the step width (SW) can be calculated every time the DSs detect the non-instrumented foot. The SW is defined as the IFDs measured by the IR ToF sensors. If a single value of SW for every swing of the instrumented foot is wanted, the mean is computed:

$$SW = \frac{1}{N} \sum_{i=ID_b}^{ID_f} IRToF_{data}(i) \tag{11.8}$$

where ID_b and ID_f are the beginning and the final instants of detection of the non-instrumented foot within the considered swing of the instrumented foot.

In this thesis BoS is defined as the area of the feet and the area between them. Thus the BoS can be calculated as the area of an irregular quadrilateral, if we know the absolute positions of its vertices. Then, given the heel and toe points and the area of the feet, the entire support

area can be geometrically obtained.
The BoS definition used in this study considers the feet in two different instants. In fact, since the BoS is the area surrounded by all the contact points during the double support phase, it is more convenient to assume that both feet are completely on the ground than consider dynamic changes of the portion of contact during the gait cycle. It would be feasible with force plates, but in this study only MIMUs and DSs are used. Under this assumption, the position of the stance non-instrumented foot is considered at its foot flat phase (t_0) and the position of the instrumented foot at its subsequent foot flat phase (t_2), after the swing in which the opposite foot is detected. In other words, the footprints are taken into account. The analysed period of time is equal to an entire swing interval from a foot flat phase to its next one of the foot instrumented with MIMU and IR ToF sensors. Assuming the floor to be flat, the problem is bidimensional. Figure 11.5 t_1 indicates the foot flat instant of the left foot.

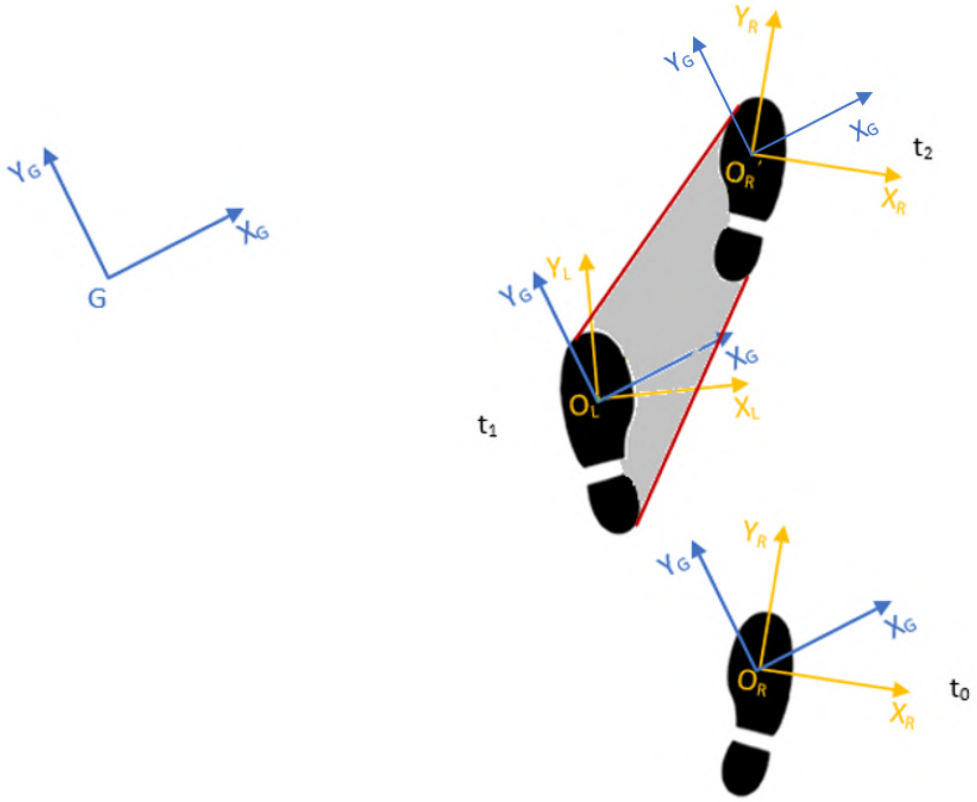

Figure 11.5: *Schematic illustration showing footprints during a stride of the right foot. On the right foot and the left foot the coordinate systems are shown. The yellow frames are the local ones, which follow the MIMU orientation during time, the blue frames are the ones parallel to the chosen global frame. The period between t_0 and t_2 is the swing interval of the right foot. t_1 is the instant of mid-stance of the left foot. The grey area is part of the BoS together with the feet area.*

The footprint shape can be modeled with different degrees of complexity and the easier way is to approximate it with a rectangle. The equation through which the BoS is calculated exploited the Bretschneider formula to achieve the area of an irregular quadrilateral. Considering the

Figure 11.6, the BoS total area is:

$$BoS_{area} = \frac{1}{4}\sqrt{4m^2n^2 - (a^2 + c^2 - b^2 - d^2)^2} \; + \; Area_{foot} \tag{11.9}$$

where $Area_{foot}$ is a rectangle.

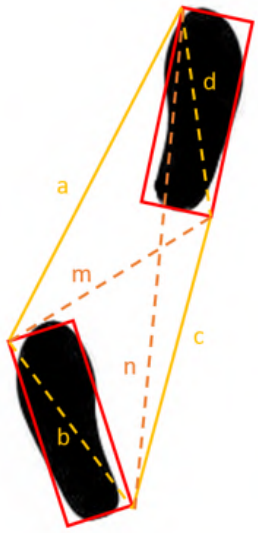

Figure 11.6: *Schematic illustration showing the BoS area. The feet are approximated with the red reactangles.*

Part III

Procedures for validation

Chapter 12

Orientation estimation

For every step of my thesis, some experiments have been done to ensure good perfomance of every part that will influence the estimate of the base of support.

First of all the orientation had to be estimated. The chosen algorithm for sensor fusion was Madgwick's filter [36] with some improvements that are explained in Part II, Chapter Orientation Estimation 9. The performances are firstly tested with a simple experimental setup. A MIMU of Xsens Technologies [43] was moved along a straight path. What we want to discover with the graphical results is whether the estimated orientation remains constant for the entire period of the movement. Since Xsens MIMU are used, we can consider the quaternions provided directly by Xsens manufacturer as a reference to understand how good the estimate is. This assumption is reasonable due to the good perfomances of these MIMUs assessed by [67] [68]. Furthermore, Xsens MIMUs are able to properly track the ferromagnetic disturbances [69].

As it is a very prelimirary test check of the sensor fusion performances, four trails have been performed. It follows an example of results, expressed in Euler angle for a more immediate understanding.

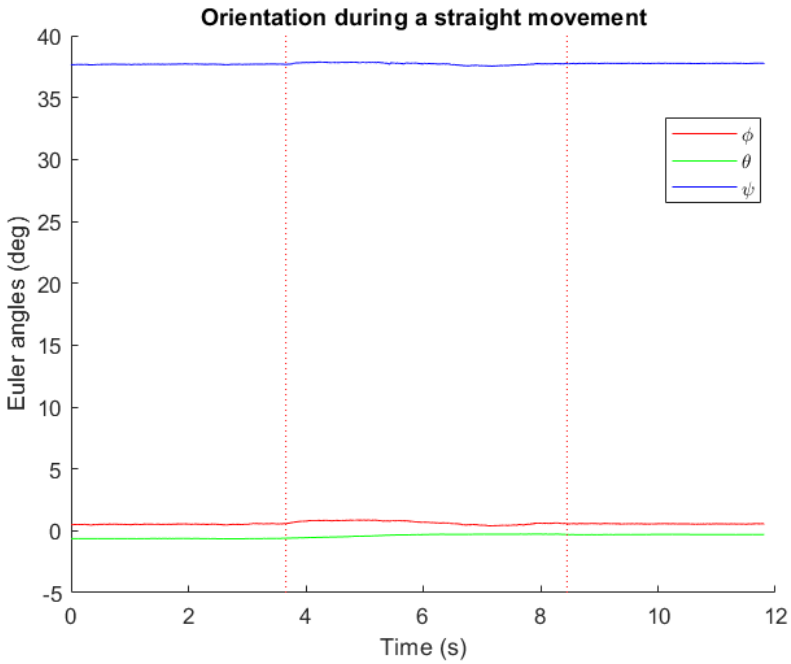

Figure 12.1: *This figure shows the Euler angles (respectively roll, pitch and yaw) of a trial in which the MIMU slithers along a straight path. The vertical dotted red lines distinguish the initial and final static phases and the central dynamic phase.*

To express the differences betweeen the Euler angles found by the method adopted in this thesis and the ones provided by Xsens, Figure 12.2 illustrates them.

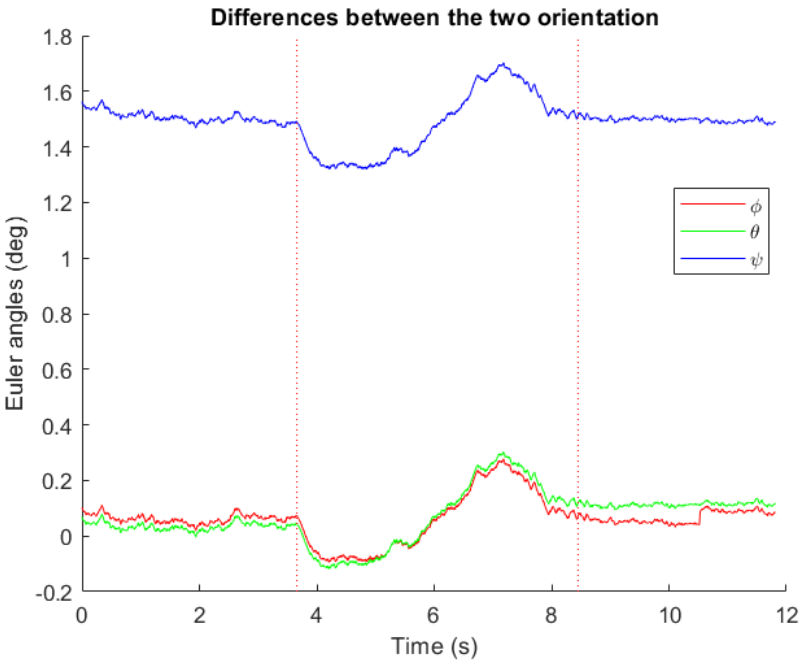

Figure 12.2: *This figure shows the absolute differences between Euler angles (respectively roll, pitch and yaw) obtained by the sensor fusion algorithm implemented in this thesis and Euler angles obtained from the quaternions provided directly by manufacturer filter from Xsens. The vertical dotted red lines distinguish the initial and final static phases and the central dynamic phase. These results are relative to the same trial of the previous image.*

The Euler angles differences are quantitatively described by Table 12.1, which shows the RMSd (Root Mean Square deviation).

Trial	**Roll** (deg)	**Pitch** (deg)	**Yaw** (deg)
1^{st}	0.2	0.3	1.8
2^{nd}	0.1	0.1	1.5
3^{rd}	0.1	0.1	1.3
4^{th}	0.2	0.1	0.5
RMSd	0.1	0.1	1.3

Table 12.1: *RMSd of absolute differences between found Euler angles and Xsens Euler angles.*

As Table 12.1 shows, generally the differences on yaw are higher, as expected, since the only way to compesate the drift on yaw is the magnetometer information, which is not always reliable due to ferromagnetic disturbances. Anyway, since the differences are below 1.8°, the performance of the implemented sensor fusion algorithm are considered acceptable for the purpose of this thesis.

Chapter 13

Displacement estimation

The second fundamental issue for the estimation of the base of support was the displacement estimation. In Part II, Chapter 10 the theory at the basis of the double integration of accelerations is explained. The accuracy of the integration had to be tested and some experiments were performed to evaluate it. The simple double integration of accelerations (gravity-compensated and filtered) seemed to be not accurate enough and its performance were compared to the ones of the Direct and Reverse Integration (DRI), which enables to reduce the typical time-dependant drift of position estimate implementing also the time-reverse integration of the acceleration signal.

To make the results more understandable, all the displacements are not shnown with respect to the ECS adopted in sensor fusion algorithm, but with respect to the MIMU LCS defined at the first frame of te movement.

First type experiment

The first experiments done for the evaluation of the displacement estimation consisted of moving along a straight path of known and defined lenght the MIMU. During the experiment, the MIMU coordinate system had x axis pointing to the positive direction of the movement and the vertical axis (z) pointing downwards. The instants of integration had been chosen manually to avoid further errors caused by the implemented algorithm for distiguishing static and dynamic epoches. Once the interval of movement was decided, the other samples are imposed to zero to not influence the displacement estimation.

Acceleration, velocity and displacement of a straight movement of 0.55 m

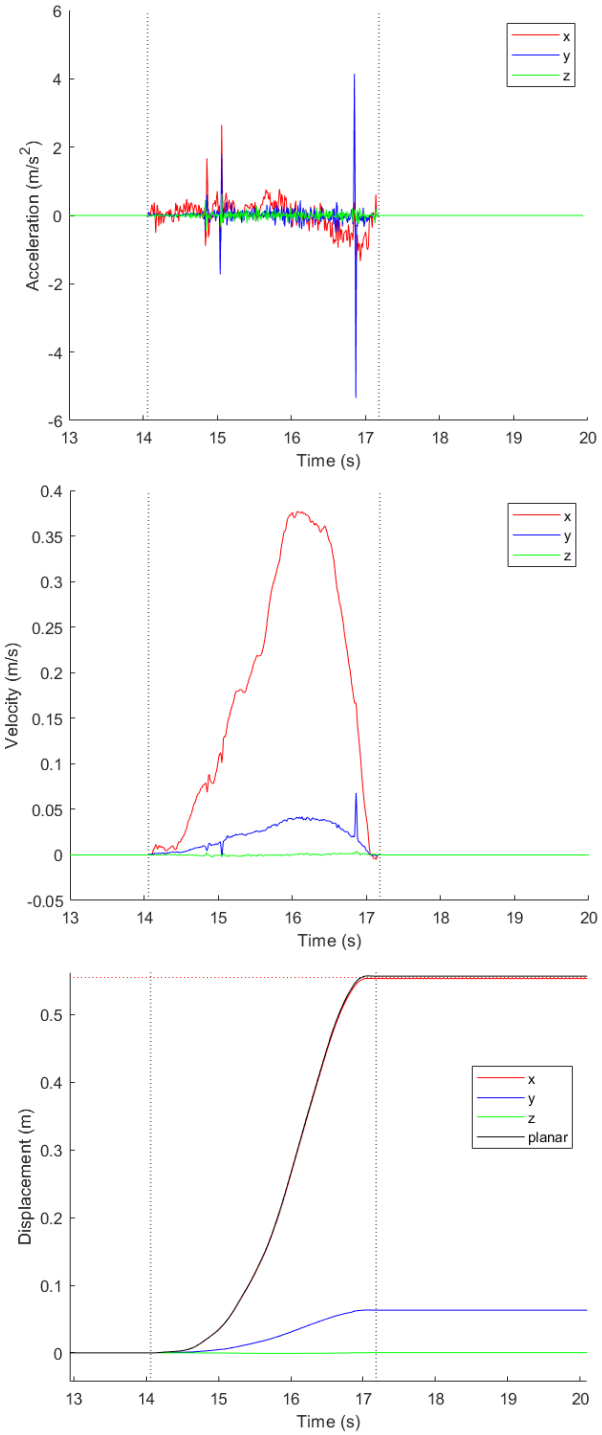

Figure 13.1: *These figures illustrate the acceleration, the velocity and the displacements along a straight path of 0.55 m of a Xsens MIMU. The horizontal dotted line corresponds to the actual measured displecement. Since the movement was along x direction, it is clear that the integration suffers from a drift especially in y direction. The planar displacement refers to the total displacement on the plane of the movement (xy). The time axis is zoomed to the interval of the movement.The vertical dotted lines segment the static and dynamic phases: the integration is done in the central dynamic phase.*

Anyway, the direct double integration suffers from a drift due to the possible uncomplete gravity compensation, which leads to a residual portion of gravity in the integrated accelerations. The less accurate the calibration of accelerations, the higher the drift is.

To quantitatively express the errors between the actual length of the displacement and the obtained one, the absolute errors and the RMSd values are taken into account. The error is calculatd as follows:

$$error \ = \ nominal \ distance \ - \ obtained \ final \ distance \tag{13.1}$$

Trial	**x error** (m)	**y error** (m)	**z error** (m)
1^{st}	0.037	-0.002	0.003
2^{nd}	0.082	-0.091	≈ 0
3^{rd}	0.012	-0.020	≈ 0
4^{th}	-0.003	-0.063	≈ 0
RMSd	0.045	0.056	0.001

Table 13.1: *Absolute errors and RMSd values of differences between found displacement estimate and the actual length of the displacement.*

In Table 13.1 if the value has the minus sign, it is relative to an overestimated displacement. Thus the displacement along y axis is alwalys overestimated, while the displacement along x axis is underestimated in the first three cases and overestimated in the fourth. Some modifications to the algorithm of double integration can be adopted to try to reduce these errors. The causes of errors are many:

- the drift is already present even if the accelerations are high-pass filteres for removing the biases;
- the choice of the initial and final samples of the integration interval influences the results leading to both underestimating and overestimating the displacement;
- the noise of the measured sensor signals.

The sensibility to this choice is further evaluated in the second type experiment to better understand the influence of chosing the initial and final instants of integration. Furthermore, since DRI can improve the estimate accuracy in those cases in which the inital and final values of velocity are known (in this case they are set to zero), a comparison between the direct double integration and the reverse-time double integration is carried out. Figure 13.2 shows an example of velocities obtained by DRI and the weighted functions that are summed to achieve the final signal.

Velocities of a straight movement of 0.55 m obtained by DRI

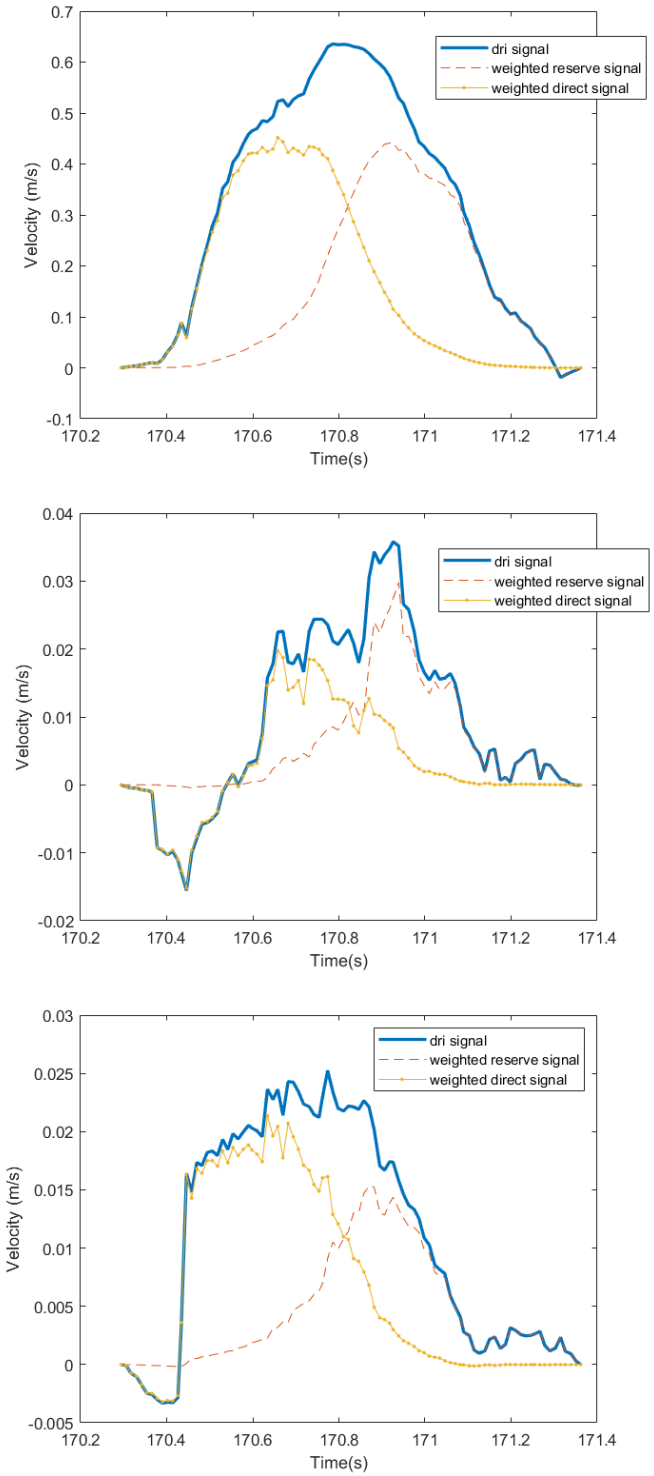

Figure 13.2: *Example of velocities (respectively along x, y and z directions of MIMU coordinate systems at the first frame of motion) obtained by DRI. The yellow line and the red line are respectively the reverse and direct integrated signal, weighted with a s-shaped function. The time axis is zoomed on the integration interval (dynamic phase).*

Second type experiment

The second experimental setup consists of a case in which three INDIP MIMUs and a Xsens were attached. This experimental setup enableed to evaluate the performance of different hardware on the same trial to assess if a specific hardware could negatively influence the displacement estimation with higher noise.
Since there were four MIMUs, they had to be synchronized to allow a comparison among them to be possible. To do that a recognizable event that could be detected in all the MIMU recordings was needed. Thus some knockings to the case were done before performing the movement of interest. Also in this preliminary experiment the trajectory of the MIMUs consisted of a straight path of known length. In Figure 13.3, the experimental setup is shown.

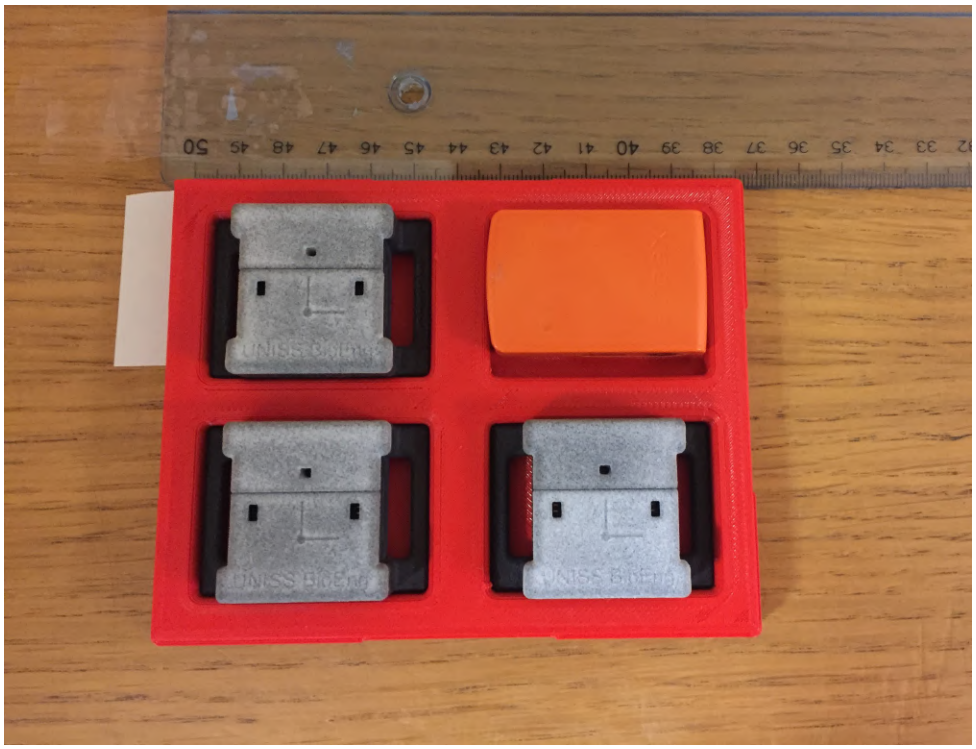

Figure 13.3: *For this experiment four MIMUs (three INDIP and a Xsens) are attached on the same case. The trajectory is linear (following the direction of the ruler) and of known length.*

For the sake of clarity, the results showed coherency among the displacements obtained by the different hardware. Thus, a systematic comparison between the performances of the single MIMUs was not deeply investigated. It follows that the results obtained by one INDIP can be shown to present the algorithm accuracy.

The sensibility of the displacement algorithm on the interval integration choice is analysed. The intervals of integration change at every analysed case: starting from the selected interval, we enlarge it considering from one to ten more samples. To segment the movement, the manually selected interval is $[s_b \ s_f]$, where s_b is the beginning sample of integration and s_f is the final sample of integration. We consider a single reference trial of an INDIP. The errors are again estimated as the difference between the actual length and the obtained one.
To understand Table 13.2 and 13.3:

- a: $[s_b \ \ s_f]$;

- b: $[s_b - 1 \quad s_f]$;
- c:$[s_b - 2 \quad s_f]$;
- d:$[s_b - 3 \quad s_f]$;
- e: $[s_b - 4 \quad s_f]$;
- f: $[s_b - 5 \quad s_f]$;
- g: $[s_b \quad s_f + 1]$;
- h: $[s_b \quad s_f + 2]$;
- i: $[s_b \quad s_f + 3]$;
- l:$[s_b \quad s_f + 4]$;
- m: $[s_b \quad s_f + 5]$;
- n:$[s_b - 1 \quad s_f + 1]$;
- o: $[s_b - 2 \quad s_f + 2]$;
- p:$[s_b - 3 \quad s_f + 3]$;
- q: $[s_b - 4 \quad s_f + 4]$;
- r:$[s_b - 5 \quad s_f + 5]$.

Case	**Absolute error** (m)	**Percentage error** (%)
a	0.040	10.70
b	0.038	10.30
c	0.037	10.00
d	0.036	9.70
e	0.035	9.60
f	0.035	9.30
g	0.042	11.30
h	0.045	11.90
i	0.047	12.50
l	0.049	13.00
m	0.051	13.60
n	0.041	11.00
o	0.042	11.20
p	0.043	11.60
q	0.045	12.00
r	0.046	12.30
Mean±std	0.042±0.005	/
95% Confidence Interval	[0.039 0.045]	/

Table 13.2: ***Direct double integration****: Absolute errors, percentage errors and mean±stardard deviation values of differences between found displacement estimate and the actual length of the displacement. The actual length was 0.37 m.*

Case	**Absolute error** (m)	**Percentage error** (%)
a	0.041	10.88
b	0.041	11.00
c	0.037	9.93
d	0.036	9.79
e	0.037	10.09
f	0.036	9.54
g	0.032	8.51
h	0.036	9.57
i	0.038	10.21
l	0.040	10.68
m	0.043	11.71
n	0.029	7.86
o	0.031	8.25
p	0.032	8.72
q	0.034	9.12
r	0.36	9.52
Mean±std	0.036±0.004	/
95% Confidence Interval	[0.034 0.038]	/

Table 13.3: ***DRI double integration****: Absolute errors, percentage errors and mean±stardard deviation values of differences between found displacement estimate and the actual length of the displacement. The actual length was 0.37 m.*

The above tables show that DRI enables more accurate estimates, even if the reported confidence intervals show that the obtained errors are really similar. The difference between the mean values is 6 mm. This occurs even in those cases in which the displacement is underestimated, thus this method not only helps to remove the possible drift but also to generally improve the displacament estimation.

The percentage error helps to quantitatively evaluate the sensibility to the initial and final instants of integration. We can deduce from the above results that the length of the interval influences the estimate even if the maximum number of added samples is ten (case r). On the other hand, this variation does not significantely affect the results, since the percentage error in all the analysed cases is between 7.50% and 12.50%. It is not straightforward that the longer the interval the higher the estimate is.

Chapter 14

Preliminary investigation on the use of infrared time-of-flight sensors for object length reconstruction

IR ToF sensors are used to detect the presence of the non-instrumented foot and create a model of it in 3D space. Thus, a preliminary experiment in which the performances of those proximity sensors are evaluated is required. Since we want to assess how IR ToF sensors performe in presence of a generic body which lies within their range of sensing (imposed to be 0.2 m), first experiments were carried out positioning an object of known dimensions in a fixed point on a plane and moving the MIMU with an attached IR ToF in front of this object. The investigated cases were the following:

- a: the trajectory of the sensors was parallel to the side of the object. The distance between the object and the MIMU trajectory is 0.12 m (Figure 14.1);
- b: the object was inclined with a certain angle α with respect to the horizontal MIMU trajectory (Figure 14.2);
- c: the 2D trajectoy of the sensors was not linear (Figure 14.3).

One of the aspects that had to be investigated is the 'border effect'. This consists of the detection of the rigid body by the IR ToF before that the DSs are in front of it. This is due to the opening of the view cone of the DSs, which is 25°, as reported in the datasheet [65]. It follows that the geometry of the detected body has an impact on the distance data and this could be a problem in the detection of the non-instrumented foot to estimate the BoS. Thus, the border effect leading to outliers in distance data must be at least qualitatively evaluated in these preliminary tests. Two different geometries were analysed using a parallelepiped (with length of 0.19 m, height of 0.05 m and depth of 0.14 m) and a flat screen (with length of 0.30 m, heigth of 0.05 m and depth of 0.004 m). The experiments with the inclined object were performed with and without a flat screen on the parallelepiped.

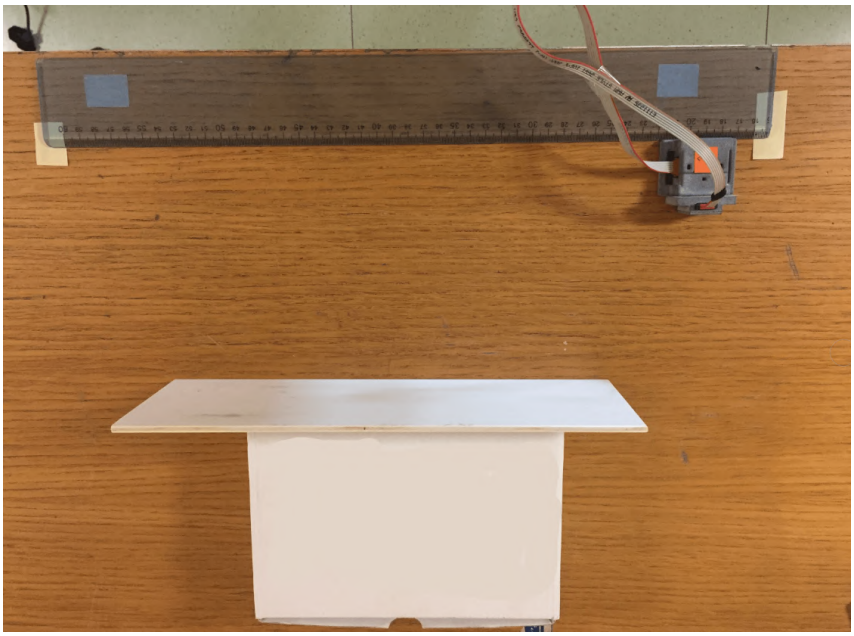

Figure 14.1: *First type of experimental setup. An INDIP with an IR ToF sensor attached on it is moved straight on.*

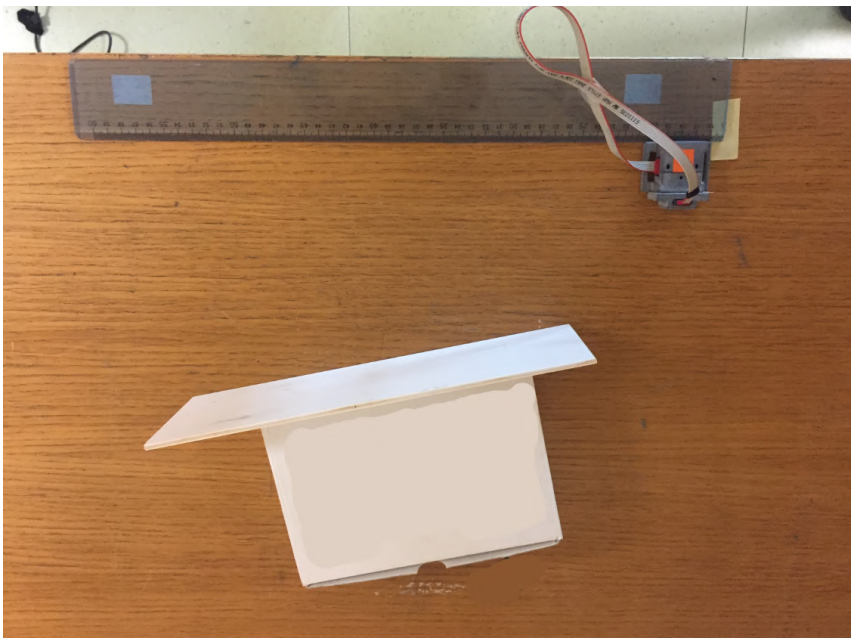

Figure 14.2: *Second type of experimental setup. An INDIP with an IR ToF sensor attached on it is moved straight on, but the object is inclined on the horizontal plane with an angle α. The experiment is performed both with and without the flat screen on the parallelepiped.*

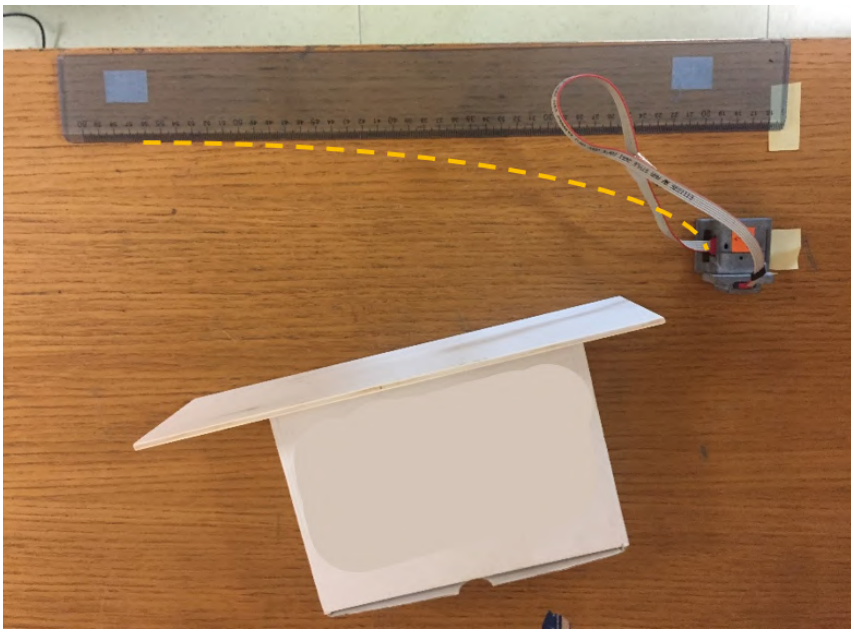

Figure 14.3: *Third type of experimental setup. An INDIP with an IR ToF attached on it is moved following a non-linear trajectory (yellow dashed line). The experiment is performed both with and without the flat screen on the parallelepiped.*

An example of result of 'scan' in every type of experiment is shown in Figure 14.4, Figure 14.5 and Figure 14.6.
From the distance data we have to extract the information of the model in the space of the detected object. Since the data are affected to some variability, a proper way to define the model of the detected body is minimizing the square mean errors. In the following figures the red lines are achieved by this method and they represent the model of the detected profile of the object.

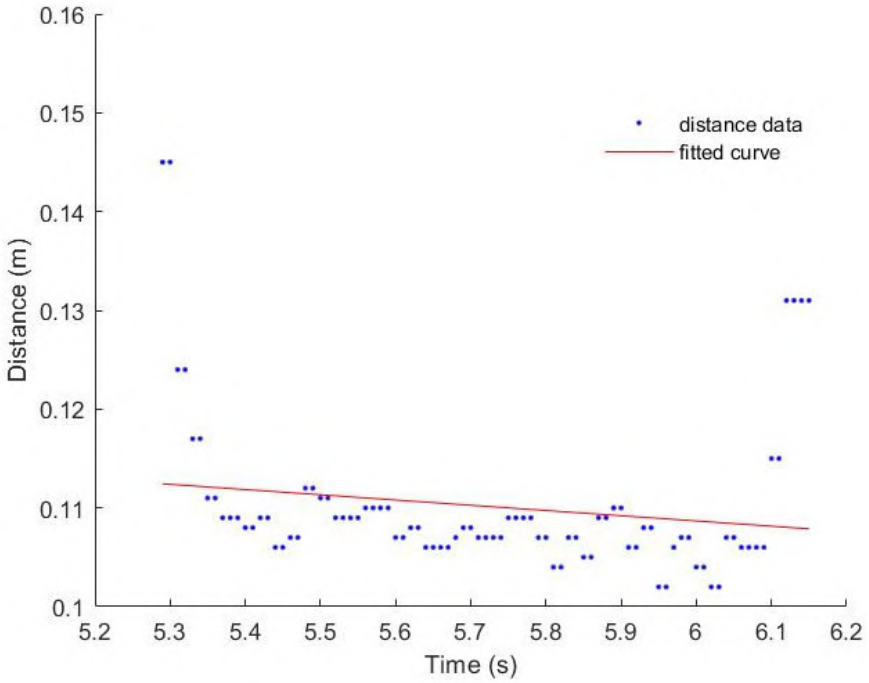

Figure 14.4: *Distance data recorded in the experiment of type a.*

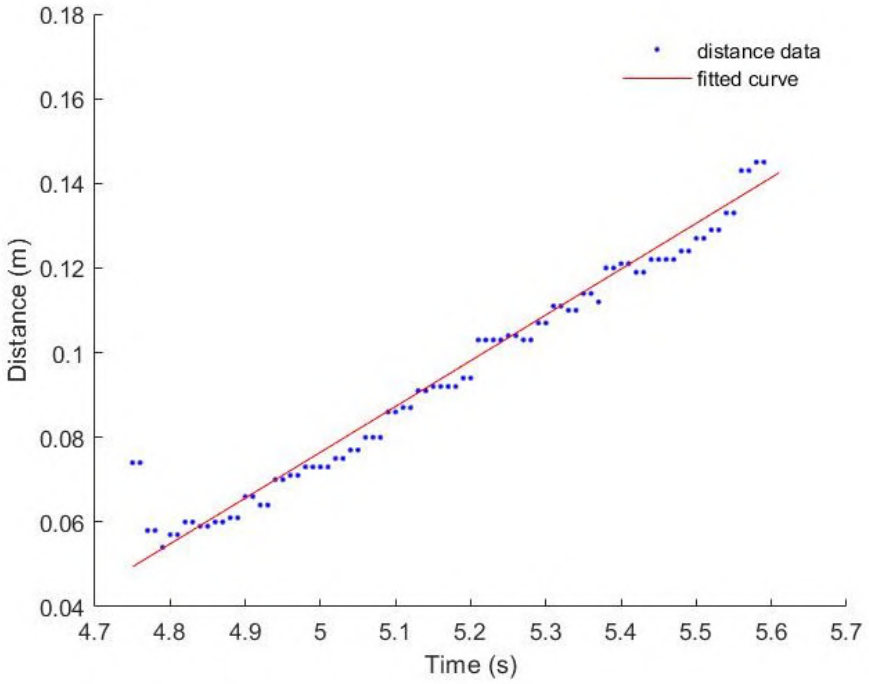

Figure 14.5: *Distance data recorded in the experiment of type b.*

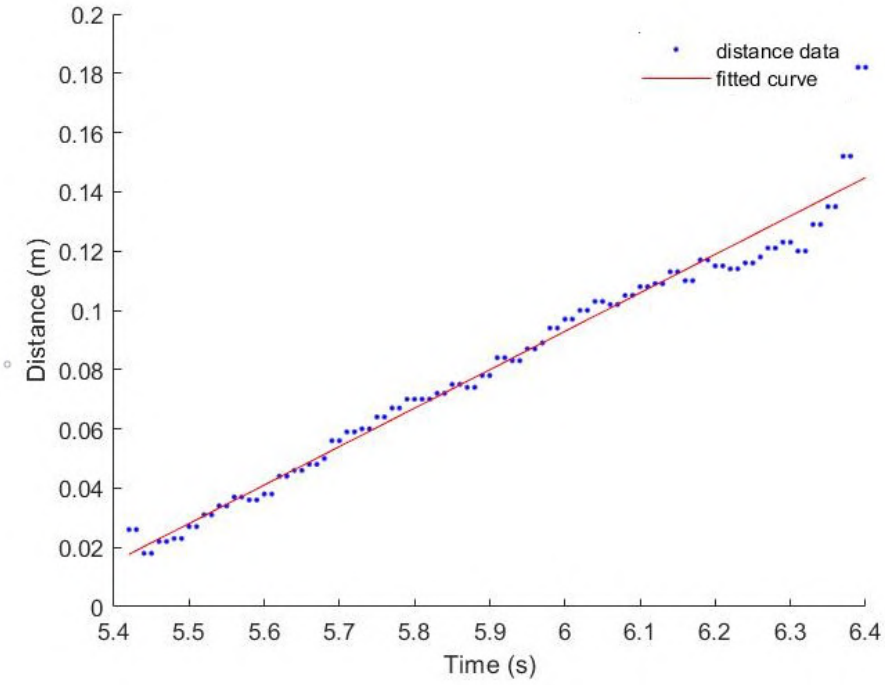

Figure 14.6: *Distance data recorded in the experiment of type c.*

What we can conclude relatively to the outliers at the beginning and at the end of the detected side is that this border effect is always present, but of course it strongly depends on the experimental data and the velocity of the distance sensors. A solution to reduce these errors consists in imposing thresholds to exclude those outliers. The thresholds can be defined as a percentage of the mean value of the points or of the linear model.

Every type of test is performed three times. The further evaluated aspects are the following:

- the length of the detected side of the object knowing the instantaneous velocity (through the integration of MIMU accelerations) along the direction of the movement and the time interval between two consecutive samples, as follows:

$$Scan\ length = \sum_i v_i \triangle t_i \tag{14.1}$$

  where i is the considered sample belonging to the interval of non-null distance data ('scan' interval).

- the angle of inclination of the model of the side of the detected object with respect to the horizontal axis, calculated as the arctangent of the angular coefficient of the model line.

Table 14.1 and Table 14.2 show the errors of the two above calcuted quantities with respect to the measured ones. The RMSd value is calculated for errors coming from the same type of trial. The actual object side was 0.30 m in cases a, b and c (cases with the flat screen), while it is 0.19 m in b' and c' (cases with only the parallelepiped).

Experimental setup	**Absolute length errors** (m)	**Percentage length errors** (%)
a	0.039	13.20
a	0.060	20.40
b	0.044	14.91
b	0.032	10.98
b	0.030	10.13
c	0.065	21.75
c	0.014	4.88
c	0.011	35.92
RMSd	0.056	/
b'	0.003	14.62
b'	0.004	21.33
b'	0.117	15.59
c'	0.079	21.02
c'	0.083	20.15
c'	0.087	0.67
RMSd	0.033	/

Table 14.1: *Absolute and percentage errors between found length and the actual one. Letters symbolise the experimental types and a, b and c refer to cases with the flat screen, b' and c' to the box without the flat screen.*

The results of Table 14.1 show more than 35% of percentage error in the estimation of the length of the detected object. This error includes inaccuracy in the velocity estimation from the acceleration integration (which cannot be quantitatively evaluated without a reference in this experimental setup), imprecision derived from the distance data values, and the presence of outliers due to the view cone. Hence, the length of the detected object is imposed in the further steps of this thesis, since it is always known (in the BoS estimation it is the length of the foot of the subject, which can be easily measured) and not obtained as described in Equation 14.1.

Experimental setup	**Actual angles** (deg)	**Obtained angles** (deg)	**Absolute angle errors** (deg)
a	0	-6.0	6
a	0	3.0	3
RMSd	/	/	/
b	15.6	37.0	21.4
b	15.6	19.6	4.0
b	15.6	19.3	3.7
c	15.6	31.9	16.3
c	15.6	18.7	3.1
c	15.6	16.2	0.6
RMSd	/	/	7.4
b'	10	15.9	5.9
b'	10	18.2	8.1
b'	10	31.5	21.5
c'	10	7.8	2.2
c'	10	26.1	16.1
c'	10	6.3	3.6
RMSd	/	/	11.8

Table 14.2: *Actual and obtained values of angles of inclination of the object. Letters symbolise the experimental types and a,b and c refer to cases with the flat screeen, b' and c' to the parallelepiped without the screen.*

The results above summarized in Table 14.2 show an RMSd of 7.39° for the cases with the flat screen and of 11.83° for the ones without it. For the sake of clarity the RMSd values are

relative to the angle of inclination errors between the model fitted on the distance data and the actual inclination of the object with respect to horizontal axis. This result suggests that the depth of the object is detected by the DSs at the beginning and at the end of the 'scan', but a a further experiment was done to prove this hypothesis. Ten 'scans' of the parallelepiped and ten 'scans' of the flat screen were performed with the same angle of inclination (15°) and moving the sensors along a straight path. The results of the comparison are reported in Table 14.3.

Geometry	**Mean ± std**	**95% Confidence Interval**	**Unit**
Parallelepiped	7.2 ± 4.2	[4.9 9.5]	deg
Flat screen	2.9 ± 1.7	[2.2 3.6]	deg

Table 14.3: *Obtained angle errors with the investigated geometries. The actual angle was 15 °.*

From Table 14.3, it follows that higher number of outliers leads to a higher imprecision in the creation of the fitted model, thus the inclination of the model line has an angular coefficient which departs from the actual one. In fact, the confidence intervals do not overlap and the mean value of the flat screen is lower of 4.3 ° than the parallelepiped mean value.
This highlights the importance to detect the outliers and exclude them in the creation of the model line. For the estimation of the BoS, this is an important expedient to reduce errors in the positioning of the non-instrumented foot in the plane.

Figure 14.7 illustrates a comparison between the distance points and model line obtained with and without the removal of the outliers, considered as all the data which depart from the mean value of more than its 30%.

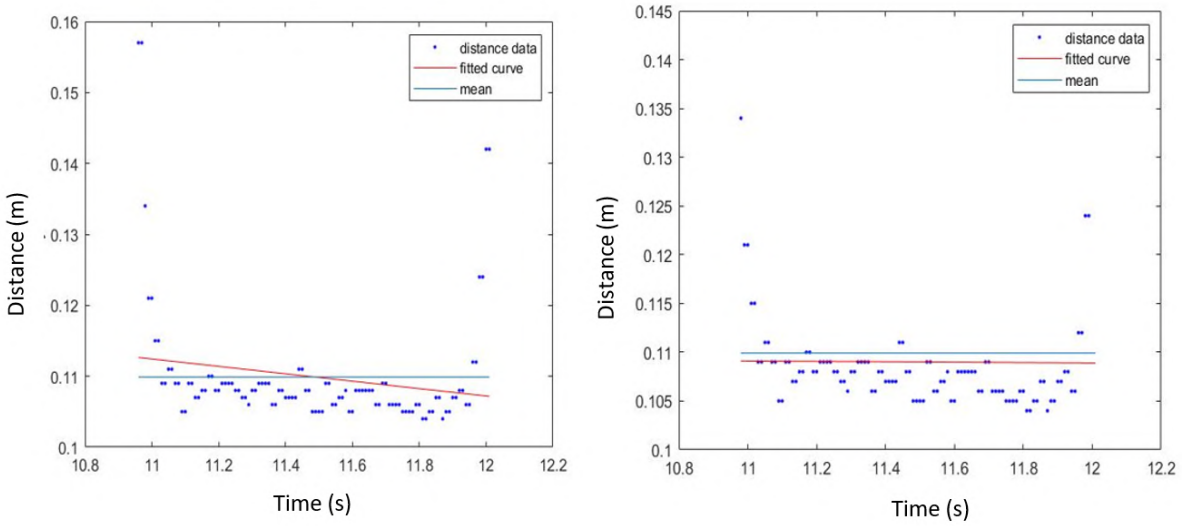

Figure 14.7: *Left: all distance data and relative model line. Right: distance data which are not considered outliers by the imposed threshold and the relative model line.*

Removing the outliers, of coursethe model fits better the data set and the line is nearer to the mean value.

The accuracy of the distance estimates is analysed in Chapter 15, dealing with the step width estimation.

Chapter 15

Gait spatial parameters

After having evaluated the performance of the orientation and displacement and having qualitatively described the IR ToF sensors' performances, the estimation of the gait spatial parameters can be done. The BoS in this thesis is defined as the area of the feet and sorrounded by both of them during a double support phase (Figure 15.1). Thus, the linear spatial parameters of interet for the BoS are the stride length and the step width. Definitions and methods to achieve those parameters are treated in Chapter 10 and 11.

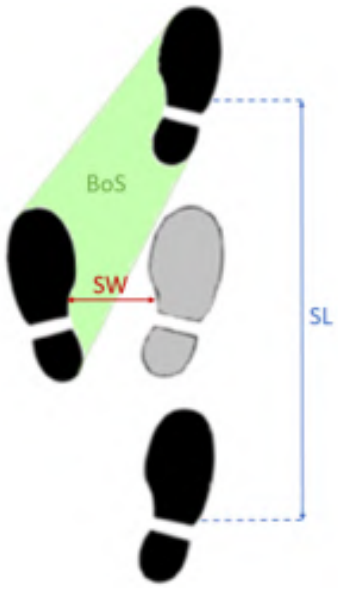

Figure 15.1: *Schematic illustration of the analysed spatial gait paramters (SL= stride length, SW= step width, BoS= base of support). The grey foot shape indicates that the foot is not in contact with the ground.*

15.1 Experimental setup

For the evaluation of both parameters, the experiments have been carried out in a human motion laboratory instrumented with SP (Vicon System) and force plates. The SP is taken as reference for the calculation of the displacements of the points on which the reflective markers are attached. The subject was a healthy person. A rigid support with a INIDP MIMU and two DSs is attached on the internal lateral side of the right foot, while on the left foot (the one that must be detected) is attached MIMU on the upper part. The experiments were performed in

two diffent ways: with and without a flat screen aiming to uniform the left foot internal profile. Figures 15.5 15.4 show the subject's feet.

The required instrumentations consist of:

- 12 x Vero cameras (100Hz),
- 3 x Bonita Video (100Hz),
- 11 fixed markers and 9 added only in the static acquisition,
- 2 INDIP MIMUs,
- 2 IR ToF sensors.

Since the maximum inter-feet distance is generally less than 200 mm, as reported in [6], the distance range of IR ToF was set to 0-200 mm.

The experimental setup is the following:

- Right foot instrumented with INDIP and two proximity sensors attached on a single support, which has the INDIP in the center and the two proximity sensors on the sides. The support is placed on the inner side of the foot (Figure 15.2);
- Left foot instrumented only with the INDIP positioned on the upper part of the foot.
- The experiments are repeated with and without a rectangular flat screen on the inner side of the left foot.
- In statics: 6 markers are placed on the right foot (heel, toe, ankle and two other markers in the area between the heel and the external medial side of the foot), four markers on the left foot (heel, toe and two markers in the area between the heel and the medial external side of the foot), a marker on each INDIP and, in addition, the temporary markers, which are: a marker on each proximity sensor, three markers on the support on which there are the sensors of the right foot. If the flat screen is present, then also four temporary markers are placed at the top of it, but if absent, four markers are placed on the inner side of the left shoe. The three markers on the rear part of the feet create a rigid body. This is exploited to have a reference frame following the foot movement. The temporary markers have the purpose to identify, with respect to the local system given by that rigid body, the plane of the lateral internal side of the left foot and and the plane of the rigid support (on which the INDIP and the two DSs are attached). Once these points and plans of interest are identified through a static acquisition, the markers can be removed. The rigid body considered as a reference consists of the heel marker and the two markers on the external medial side of the foot.
- In dynamics: only the heel, toe, ankle, and INDIP markers are placed on the right foot, and only the toe, heel and INDIP markers on the left. Temporary markers are removed.

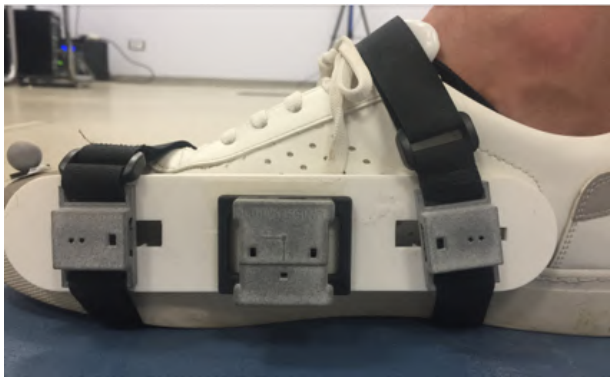

Figure 15.2: *Set up of the MIMU and the two DSs attached on the same planar support.*

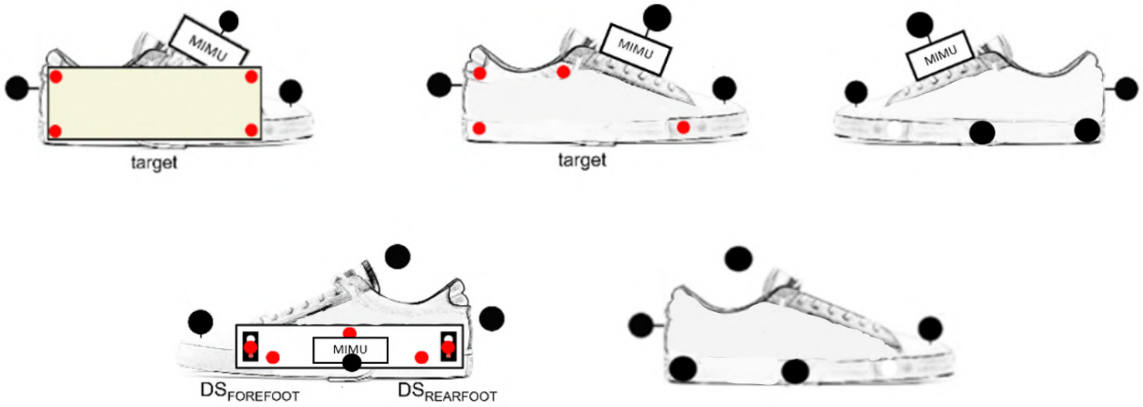

Figure 15.3: *Schematic illustration of the feet with the reflective markers. The upper figures show the left feet (from left: internal side with flat screen, internal side without flat screen, external side) and the other figures show the right foot (from left: internal side, external side). The red markers are temporary (just for static acquisition). The MIMU attached on the left foot is used just to check that the foot is stationary while the IR ToF sensors detect it.*

The protocol was the following:

1. 10 minutes of warm-up of inertial sensors;
2. Preliminary acquisition in static condition of 5 minutes of the inertial sensors to estimate the bias of the gyroscope;
3. Preliminary acquisition of the IR ToF sensors at a known distance to estimate the offset;
4. To synchronize the INDIP and Vicon data, an initial impact is used on the force platform, firstly with a foot and then with the other one;
5. The subject walks, at a self-selected speed, reaching the starting point of the experiment path and stops for about 10 seconds;
6. Straight path for a length of about 5 meters;
7. Static phase of about 10 seconds;
8. The subject returns to the initial point, always with a self-selected speed;

9. Repeat until reaching 5 trials (the same path is done 10 times);
10. Further impact to the platform by both feet for the purpose of synchronization;
11. End of registration.

Figure 15.4: *Right foot of the subject during the experimantal session aiming at estimating the spatial gait parameters with the SP refence.*

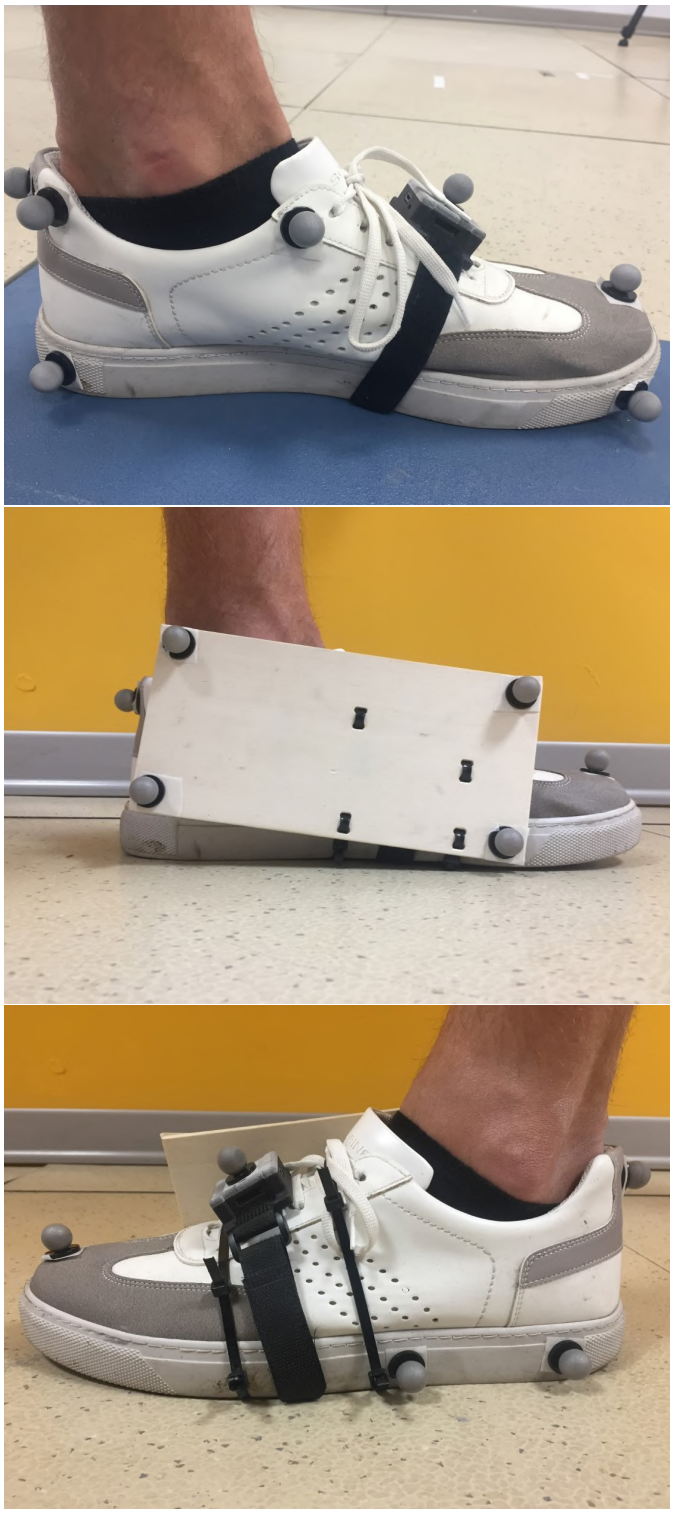

Figure 15.5: *Left foot of the subject during the experimantal session aiming at estimating the spatial gait parameters with the SP refence. The first figure referers to the case without the schield, the second shows the attached flat screen.*

15.2 Alignment of stereophotogrammetric and MIMU coordinate systems

The aim of the experiment is to compare the performances of INDIP in estimating spatial gait parameters to the ones of the Vicon system. Thus, the SP displacement of the MIMU marker has to be taken into account. Indeed, the INDIP-based displacements are of course relative to the point in which the MIMU lies.

The displacement provided by the SP and the displacement obtained with the DRI integration of the g-compensated and filtered accelerations from MIMU are referred to two different coordinate systems. Indeed, the Vicon system at each experiment has to be calibrated and a new fixed reference is imposed. This coordinate system does not coincide with the one describing the MIMU sensor data. The latter are expressed with respect to the first frame of the movement taken into account. Thus, one coordinate system must be rotated to be aligned with the other. The orientation of MIMU is known thanks to the sensor fusion algorithm that provides the quaternions at every time step. It follows that those quaternions can be used to rotate the Vicon coordinate system to make it to coincide with the first local frame of MIMU. Also the origins of the two reference systems are not equal, thus the Vicon displacement, after having been rotated, is also translated to the position of the MIMU marker at the fist instant of motion.
To do that a description of the orientation of the MIMU with respect to the Vicon system must be achieved. The mathematical formulation of the method is the following:

1. The three markers applied on the posterior part of the feet which creates a rigid body are used to describe a local coordinate system which rigidilly follow the foot motion. Thus a rotation matrix (${}^{L}R_{G_v}$) which enables the Vicon global system (G_vCS) to coincide with this local system (LCS) of the right foot is obtained. This is done for the static acquisition, when also all the temporary markers are attached;

2. The distance vector between the origin of the LCS and each temporary marker of the rigid support, of the IR ToF sensors, and of the target plane is calculated (d^{G_v}). This is a vector expressed in G_vCS. This vector is rotated into the LCS by the static rotation matrix found at the previous point:

$$d^{L}_{statics} = {}^{L}R^{statics}_{G_v}\ d^{G_v}_{statics} \tag{15.1}$$

   Thus the relative distances between the temporary markers and the origin of LCS is known. These are always constant since the LCS follows the foot movement.This infomation enables to provide the positions of those markers even when they are not anymore present in dynamics.

3. ${}^{L}R_{G_v}$ is calculated at every FF_i instant of the right foot. Then, the distance vector described in LCS can be re-rotated into G_vCS:

$$d^{G_v} = {}^{L}R'_{G_v}\ d^{L}_{statics}\ +\ O_L \tag{15.2}$$

   The origin of LCS, O_L, is added to always refer the displacements to the fixed origin of G_vCS.

4. Once we have obtained the position of three non collinear points of the support on which lies the MIMU, we assume that the MIMU has the same orientation of the support on which it is attached. So the wanted relation between the coordinate systems is picked out, since these positions are described in the G_vCS. The easiest way is to calculate the inclination of the support on the horizontal plane and use this angle α to create a rotation matrix R_α.

5. Vicon data are rotated with this rotation matrix:

$$Displacement^{L} = R_{\alpha}\ Displacement^{G_v} \tag{15.3}$$

15.3 Stride length

The stride length (SL) is defined as the the distance of the same point of the same foot between instants within two consecutive ZUPT intervals with the acceleration magnitude closest to the the gravity (FF_i and FF_{i+1}). Chapter 10 describes the followed method to estimate this parameter. Stride lenghts can be evaluated from displacement obtained by MIMU through the DRI method and the displacement provided by Vicon rotated so that the coordinate systems of both signals are the same.
An example of comparison between those displacements is provided in Figure 15.6.

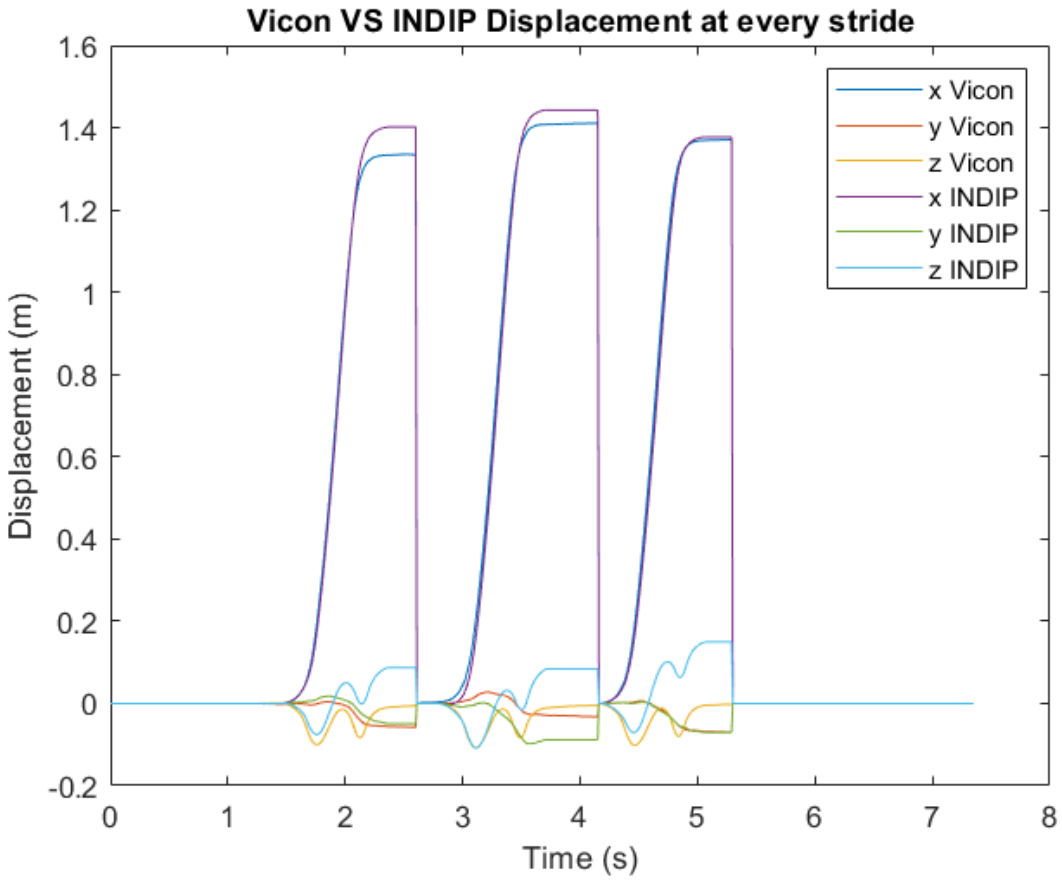

Figure 15.6: *Displacements expressed with respect to MIMU local coordinate systems at the first instant of every gait cycle. In this figure it can be seen that the subject made three strides and it is reset to zero at every FF instant.*

To evalute the accuracy in the estimation of stride length, only the displacement along the direction of progression is considered (x direction in the case of Figure 15.6). Table 15.1 sums up the differences betweeen the found stride lenghts and the ones calculated with SP. The errors were again calculated as the gold standard distance minus the obtained distance. Thus a negative error indicates an overestimation.

$$error\ =\ SL_{SP}\ -\ SL_{MIMU} \tag{15.4}$$

	Mean	Standard Deviation	95% confidence interval
SL errors (m)	-0.037	0.064	[-0.054 -0.019]

Table 15.1: *Stride length errors expressed as mean±standard deviation value. These results are achieved analysing 52 strides.*

The value of RMSd shown in Table 15.1 suggests that the absolute errors of 0.037 ± 0.064 (mean±standard deviation) are acceptable, since the range of the evaluated stride lengths was about 1.3-1.6 m. The estimation of stride length provided by the MIMU displacement is generally higher than the SP one due to the integration drift, which is not totally eliminated by the DRI. However, few cases in which the MIMU underestimates the stride lengths occur.

15.4 Step width

The step width (SW) in this experiment is defined as the mean value of IFDs in a step and calculated when the feet face each other. This is beacuse inter-feet distance is mesaured by the IR ToF sensors when they see the left feet. It happens twice in a gait cyle.

The IR ToF sensors were calibrated before the experiments, thus their offset was estimated. This procedure consists of positioning the IR ToF at a distance of 0.05 m to an object that is built exactly for this purpose (Figure 15.7). It has a circular part to which the cone of vision the IR ToF must point. The distance sensors record for about 30 seconds, while it is stationary and in front of this object, so the offset is estimated, knowing the actual distance. Hence, all the experimental distance data are corrected by substracting the offset.

Figure 15.7: *Object modelled for the estimation of the offset of the IR ToF sensors. The actual distance that they would measure is 0.05 m.*

The IFD must be compared to the distance between feet calculated with SP displacements of the markers. The markers on the DSs are present only in the static phase, since they could interfere with the IR emitted or received waves. The same steps described in Section 15.2 are followed to provide the positions of DSs, the rigid support plane, and the target plane. This is done exploiting the refence given by the three rear markers of the rigid body on the feet. Then the perpendicular distance from the DSs positions to the target plane can be evaluated. To do that, it has to be found the intersection between the target plane and a line starting from the

DS position and perpendicular to the rigid support plane [45]. Then the SW estimate of SP is achived by doing the mean value of the IFDs for every foot oscillation. The target is the flat screen or the internal side of the left foot.

Figure 15.8 shows graphically and schematically the principal points and entities that must be taken into account.

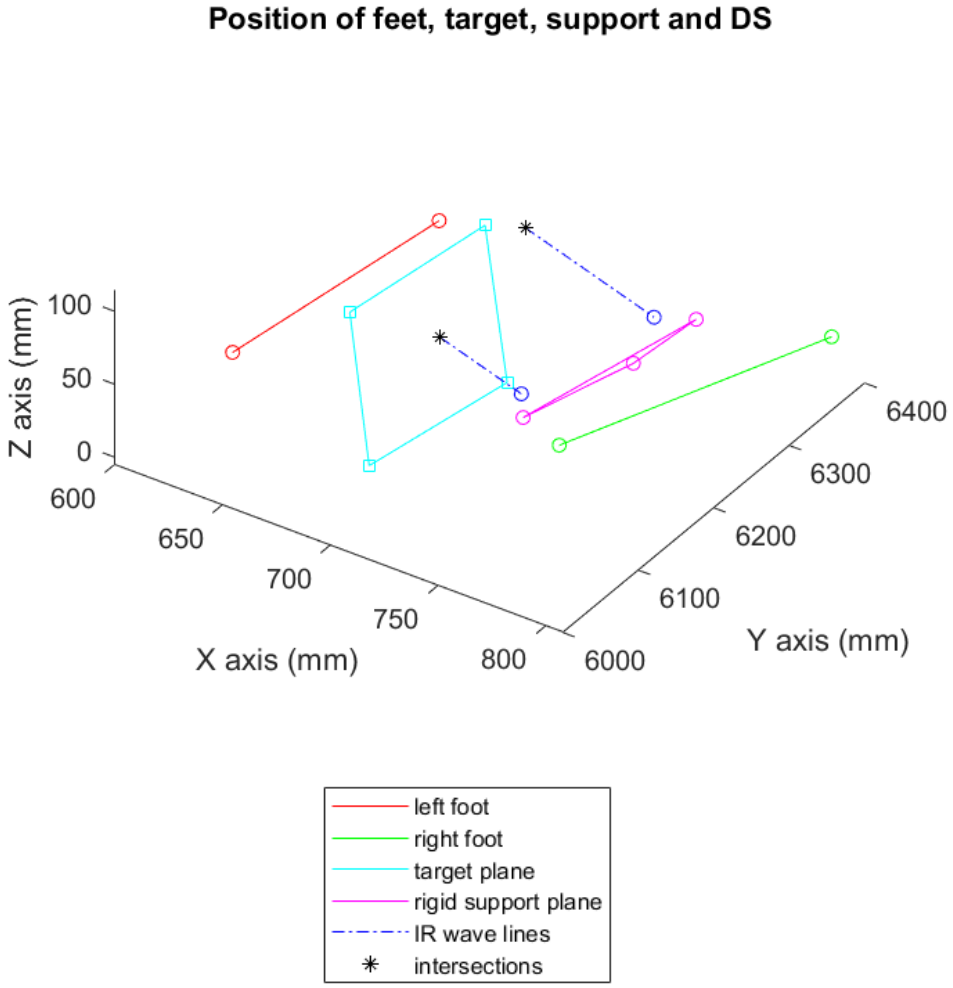

Figure 15.8: *The blue lines are the perpendicular distances from the IR ToF sensors to the target plane (distances between the emitters of IR waves and the target). The legend of the figure follows. Green: heel and toe markers of the right foot, Red: heel and to marker of the left foot. Light blue: the quadrilateral identified by the target markers. Pink: three markers of the support on which the sensors are attached. Black asterisk: intersections between the target plane and the IR waves lines.*

The inaccuracy in step width estimation is evaluated. In particular, the inter-feet distance error is evaluated by distinguishing the performance of the distance sensor nearer to the toe (DS FRONT) and the one nearer to the heel (DS REAR). Figure 15.9 shows the occurrences of error values in a trial of 5 m. The reported errors were obtained as follows:

$$error = distance_{IR\ ToF} - distance_{SP} \tag{15.5}$$

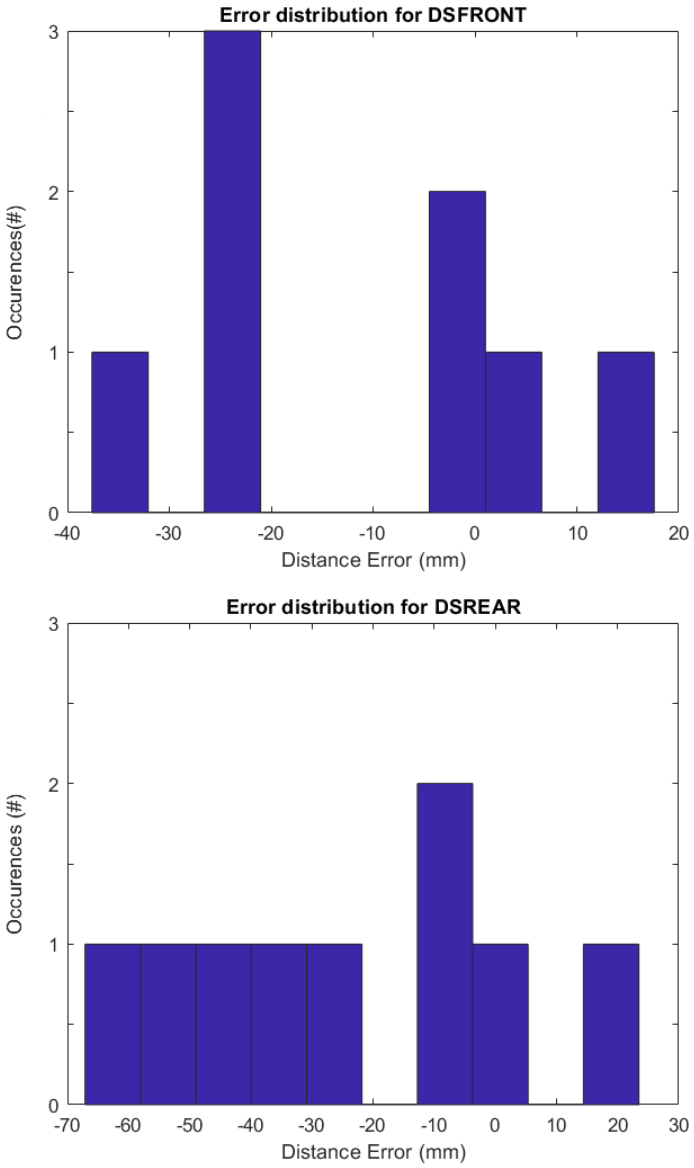

Figure 15.9: *Error distribution in a trial of walking for 5 m. The graphics show the occurrences of errors in mm, defined as the difference between the IR ToF data (DS FRONT and DS REAR) and the distance inter-feet calculated with SP.*

Generally, the DS FRONT better detects the left foot, as Figure 15.9 confirms. It follows that the IR ToF sensors must be positioned in the anterior part of the foot, if only a DS can be used. For the sake of completeness, the mean±standard deviation of the absolute SW errors of all the analysed steps was 0.015 ± 0.017 m for DS REAR and 0.031 ± 0.022 m for DS FRONT.

The errors were calculated for the cases with and withuout the flat screen attached on the left foot. The results are reported in Table 15.2 and Table 15.3.

	Mean	Standard Deviation	95% Confidence Interval
SW errors (m)	-0.023	0.021	[-0.027 -0.018]

Table 15.2: ***Case with the flat screen****: Step width errors described by mean, standard deviation and RMSd. These results are achieved analysing 92 steps.*

	Mean	Standard Deviation	95% Confidence Interval
SW errors (m)	-0.027	0.032	[-0.034 -0.019]

Table 15.3: ***Case without the flat screen****: Step width errors described by mean and standard deviation. These results are achieved analysing 69 steps.*

As expected, the errors are higher if the detected surface of the left foot is not flat. The difference between the errors in the case with and without the flat screen is of 4 mm in mean value. Although, the confidence intervals partially overlap, so that the two analysed SW errors are not statistically affected by the experimental setup. In any case the errors are below 3 cm, thus they are considered acceptable for the application of this thesis.
This error cannot be compensated in the estimation of the BoS. Indeed, the left foot is positioned in the same common coordinate system of the right foot through the information derived from the DSs. Thus, it should be noted that this error definitely influences the BoS estimates accuracy.

15.5 Base of support

The evaluation of the errors in the estimation of the stride length and step width are necessary to define the accuracy that the estimation of the BoS can have. Indeed, the error of the estimation of the area of the BoS depends on the errors that affect both the MIMU and the IR ToF measurements.

The method to obtain the BoS, described in Chapter 11, is based on the assumption that the BoS is the area of the feet and between the feet when both are completely in contact with the ground. If this does not occur, the BoS is calculating considering the 'footprints'. The feet are approximated as rectangles imposing the length of the rectangle as the foot length. Figure 15.10 represents both feet in the same common reference system.

The BoS estimation is validated with the SP, as the aforementioned linear parameters. The feet are approximated with rectangles. The latter are constructed from the toe and heel markers. It is assumed that the markers are at the half of the width of the feet. Figure 15.11 shows a BoS estimated with Vicon data.

The errors of BoS, which is a 2D parameter, are multiple:

- both feet are not positioned correctly, since it is a mediolateral and anteroposterior error in the displacement estimation by MIMU of the right feet;
- the IR ToF values introduce an error in the SW, which is mirrored by a further imprecision in the positioning the left foot in the common reference system. Furthermore the IR ToF data contain outliers, due to view cone of the DSs, which may not have been completely removed;

Figure 15.12 shows a comparison of the BoS found by MIMU and DSs and the BoS calculated with Vicon data.

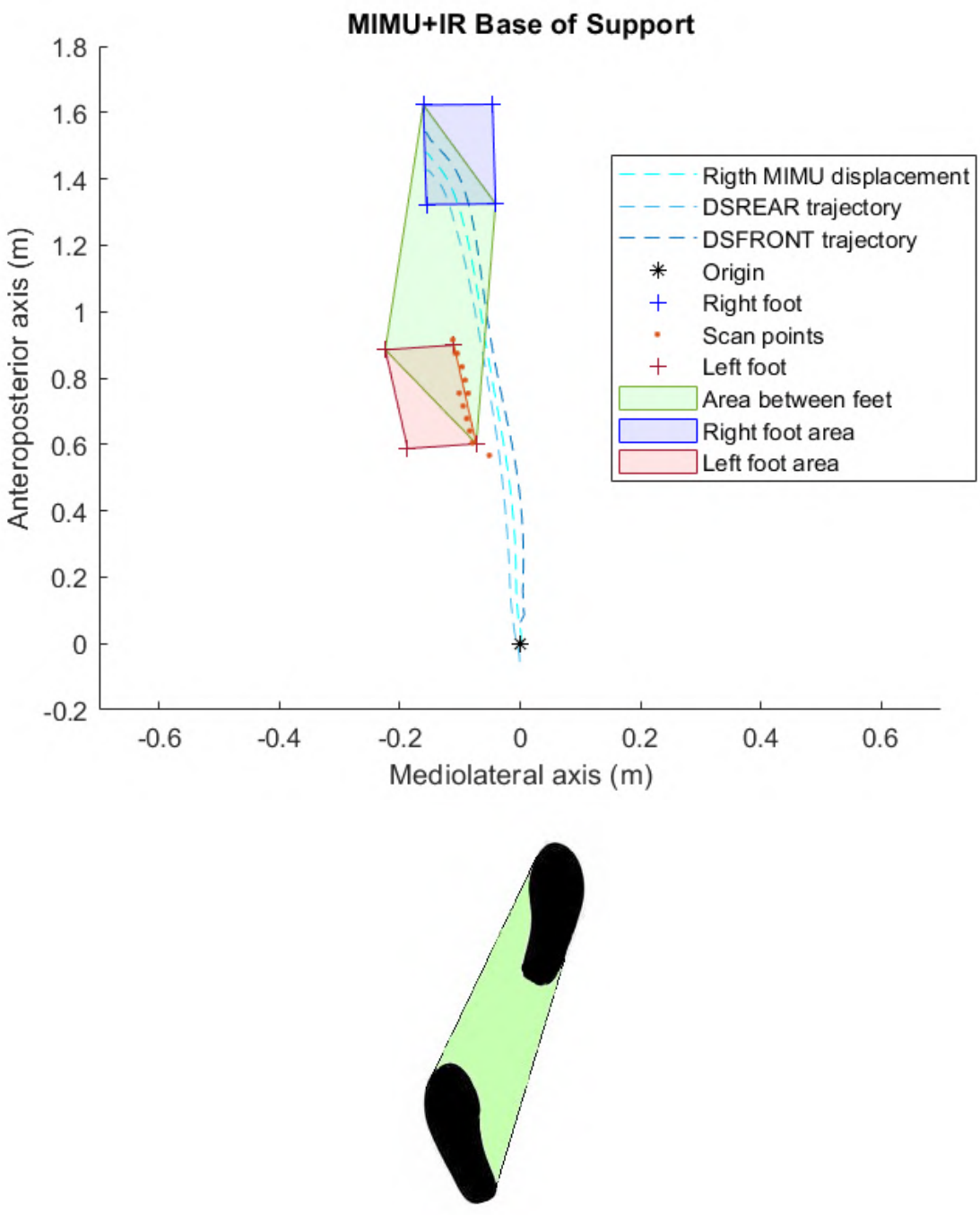

Figure 15.10: *First figure shows both feet position expressed in a common coordinate system (which coincides with the MIMU coordinate system at the first instant of this stride). Thus the origin is the position of the MIMU at the beginning of the stride, while the blue rectangle symbolizes the right feet again in contact with the ground, at the end of its swing. The red rectangle is the left foot in stance phase. The orange points are the points detected by the distance sensors. Second figure illustrates the meaning the of first one.*

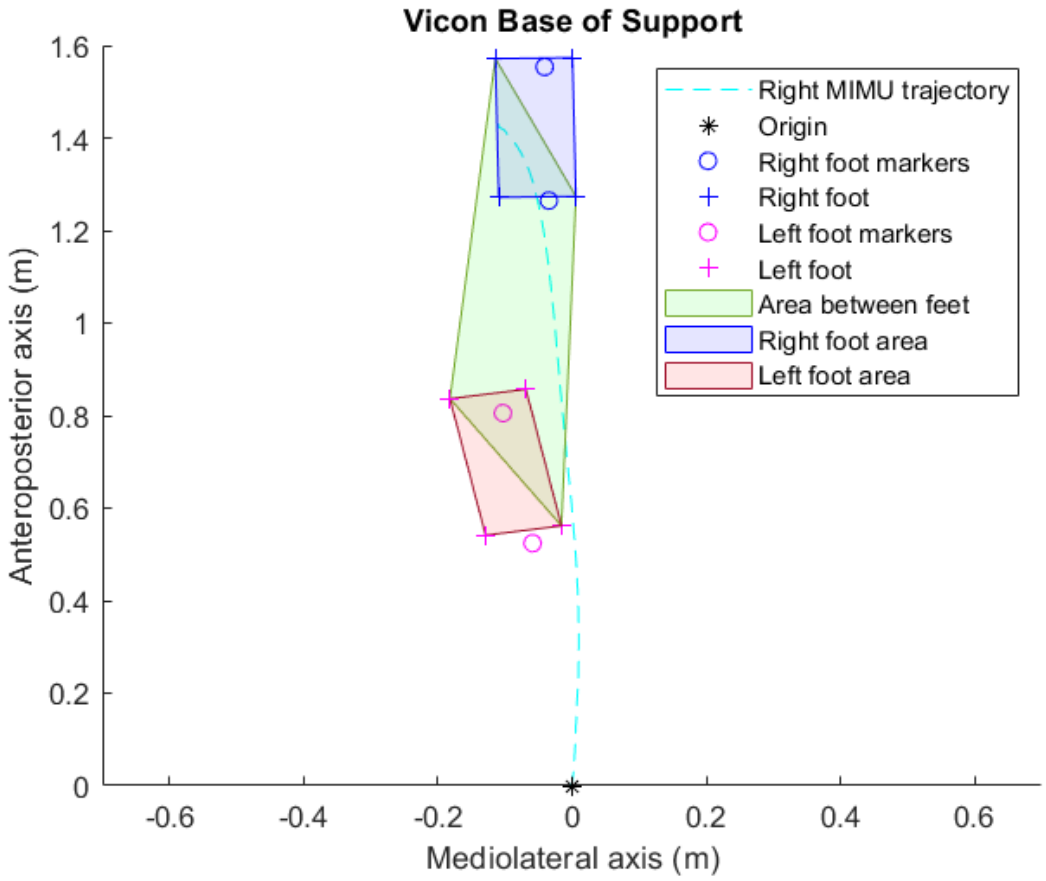

Figure 15.11: *This figure shows both feet position expressed in a common coordinate system (which coincides with the MIMU coordinate system at the first instant of this stride). The displacement of right foot is provided by Vicon and rotated as the MIMU local system. Thus the origin is the position of the MIMU at the beginning of the stride, while the blue rectangle symbolizes the right feet again in contact with the ground, at the end of its swing. The red rectangle is the left foot in stance phase. The circles are the toe markers and heel markers of both feet.*

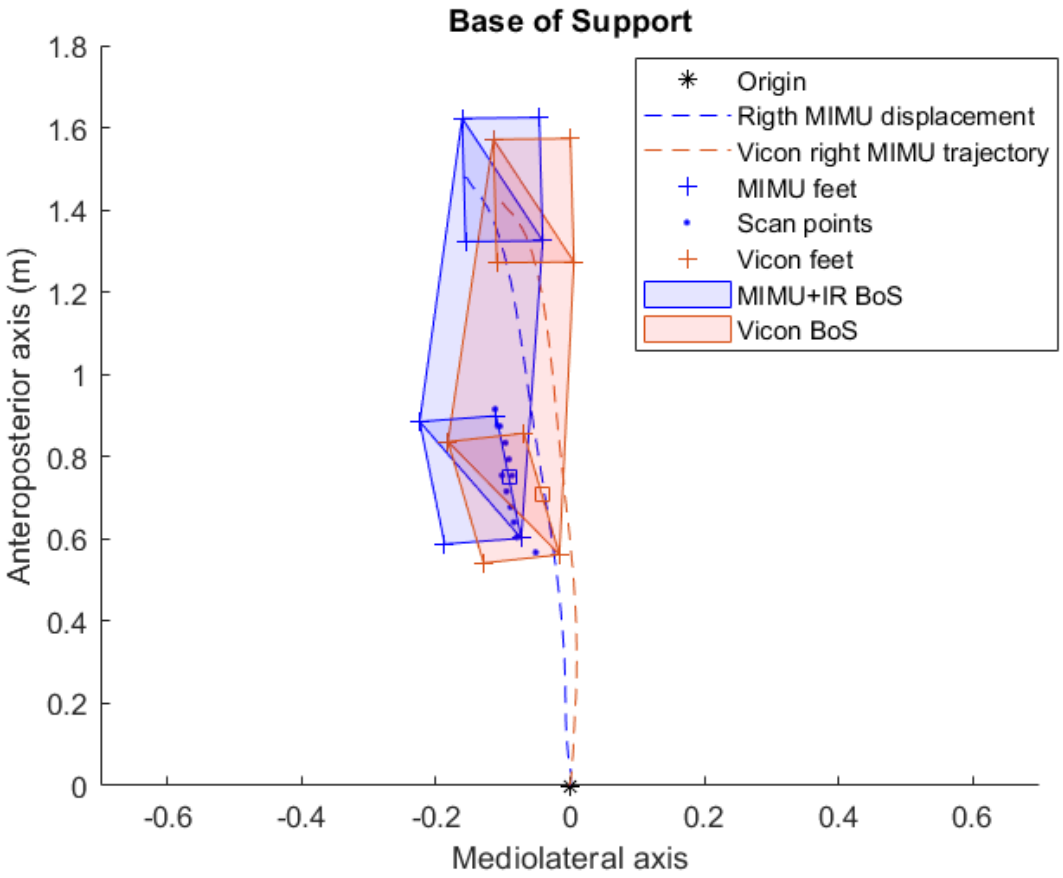

Figure 15.12: *This figure shows the base of support obtained with Vicon and with MIMU and distance sensors. The two bases have similar dimansions but the position of the feet in the same coordinate system does not coincide. The little squares indicate the center of mass of the internal side of the left foot.*

The quantitative description of the BoS errors must take into account two aspects:

- the extension of the BoS area, which is evaluated considering the error in m^2 with respect to the area found with the stereophotogrammetry:

$$error_{area} = AreaBoS_{MIMU} - AreaBoS_{SP} \tag{15.6}$$

- the position of the BoS area, which is evaluated as the distance between the center of mass of feet calculated with MIMU and with SP. These errors are called right foot shift and left foot shift.

$$error_{position} = distance\ between\ CoM_{MIMU}\ and\ CoM_{SP}$$

The aforementioned errors were both calculated in case with and without the flat screen attached on the left foot (Table 15.4 and Table 15.5).

Error type	Mean	Standard Deviation	95% Confidence Interval
Area Error (m^2)	-0.0041	0.0063	[-0.0069 0.0013]
Left Foot Shift (m)	0.055	0.024	[0.045 0.065]
Right Foot Shift (m)	0.067	0.032	[0.053 0.081]

Table 15.4: ***Case with the flat screen****: BoS errors expressed in area errors (the difference in m^2 with the SP BoS area), right and left foot shift (the differences in m between the CoM of the right and left foot estimated with MIMU and SP). These errors are obtained analysing 20 BoS estimates.*

Error type	Mean	Standard Deviation	95% Confidence Interval
Area Error (m^2)	- 0.0125	0.0345	[-0.0276 0.0026]
Left Foot Shift (m)	0.062	0.027	[0.050 0.074]
Right Foot Shift (m)	0.094	0.046	[0.074 0.114]

Table 15.5: ***Case without the flat screen****: BoS errors expressed in area errors (the difference in m^2 with the SP BoS area), right and left foot shift (the differences in m between the CoM of the right and left foot estimated with MIMU and SP). These errors are obtained analysing 20 BoS estimates.*

It can be deduced from Figure 15.12 that the BoS area of MIMU and IR ToF sensors is shifted forward in the anteroposterior direction. The principal cause of this shifting error is due to the drift in the integration of the MIMU accelations, which leads to have an anteroposterior and mediolateral displacement higher than the actual. Table 15.4 and Table 15.5 quantify the analysed errors in the BoS estimation. As expected from the results showed for the SW accuracy, the left foot position is better estimated in presence of the flat screen (difference between the mean of left foot shift with and without the flat screen is of 7 mm). Although, it should be noticed that the reported confidence intervals of the left foot shift errors in case with and without the flat screen partially overlap, thus this error type is not statistically different in the two analysed cases, as the SW error was. The accuracy of positioning the right foot of course is not affected by the distance sensors and the difference between the results of the right foot shift errors in case with and without the flat screen is only due to the non-predictable amount of the integration drift. The errors of the left and right foot shifts have an impact on the BoS area, which is thus worse estimated without the flat screen. The difference between the mean values of the BoS area erros between the case with and without the flat screen is 0.0084 m^2.

Improving the positioning of both feet, the BoS estimation would improve in terms of area and position. The right foot position is affected only by the displacement estimation method. The left foot position is affected by not only the displacement estimation of the right foot but also by the detection made by the DSs.
From all the tested strides, it emerges that the outliers of distance data are present especially at the end of the 'scan' of the left foot. The fitting errors caused by these outliers are added to the integration drift and lead to position the left foot forward. This causes an increase of the difference between the positions of the BoS areas from MIMU and SP. A solution to reduce the errors in the positioning of the left foot consists of two expedients:

- The outliers can be reduced considering the cone of vision of the distance sensor, removing the assumption that the DSs only detect a body exactly perpendicular to them. Based on what is declared in the datasheet of the IR ToF sensors [65], the angle of the cone of vision is set at 25°. The distances at the beginning and at the end of the 'scan' interval can be rotated by this angle to detect more reliable points in the common reference.
- If the previous method does not solve the problem, it can be reasonably concluded that the presence of outliers at the end of the detection of the left foot depends on the walking of the subject. A possible solution to reduce these artefacts can be to shift backwards in the anterioposterior direction the center of mass of the detected surface of the left foot. This is done by imposing a threshold on the anterioposterior component of the detected points of the left foot. This threshold can be automatically set depending on the half of the right foot stride length. The center of mass of the detected surface is then achieved by weighting points before and after that threshold in different ways. The length of the linear model is imposed considering this new center of mass.

Figure 15.13 and 15.14 show the same stride of the previous images but with the two described methods to reduce errors in the left foot positioning. In the represented case, the detected points beyond the threshold (half of the right stride length) are multiplied for a factor α of 0.2, while the other for $1 - \alpha$.

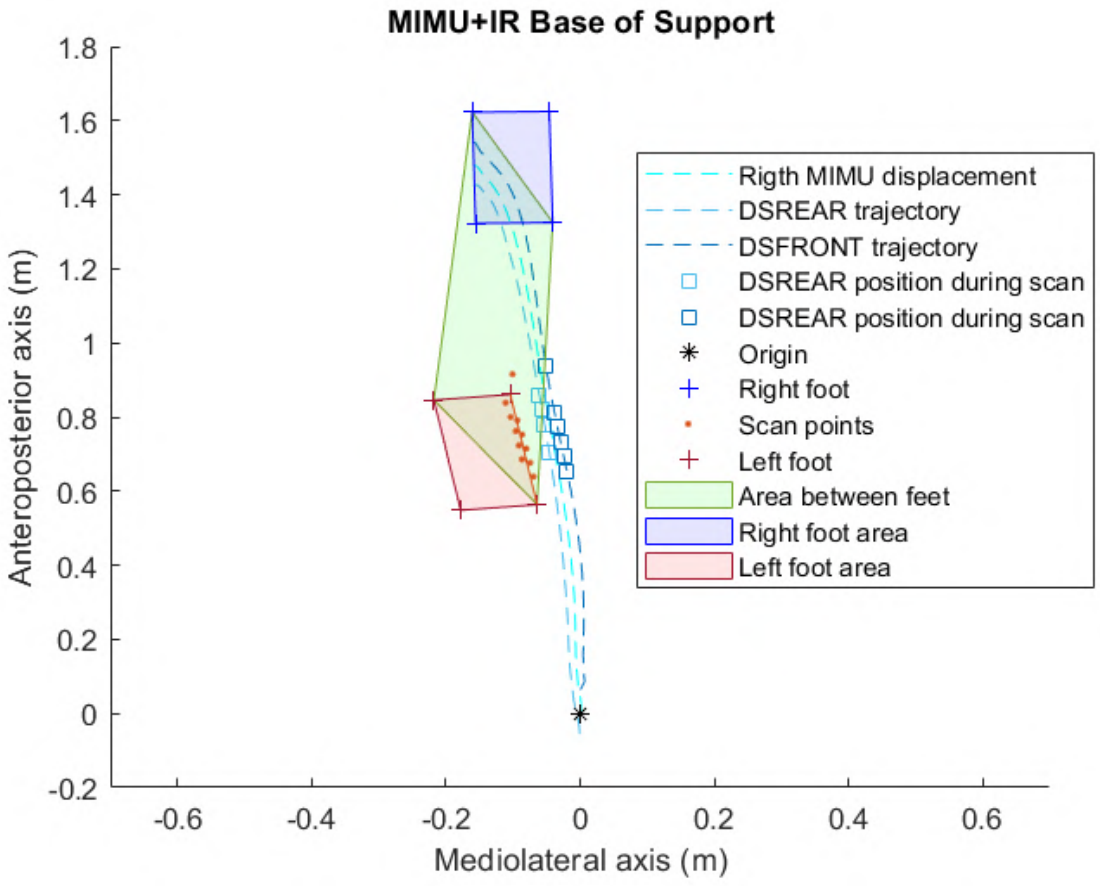

Figure 15.13: *This figure shows the same stride of the previous images, but not assuming that the distance sensors see a body only perpendicularly and giving less weight to the last distance data (containing an artefact due to the way of walking of the subject).*

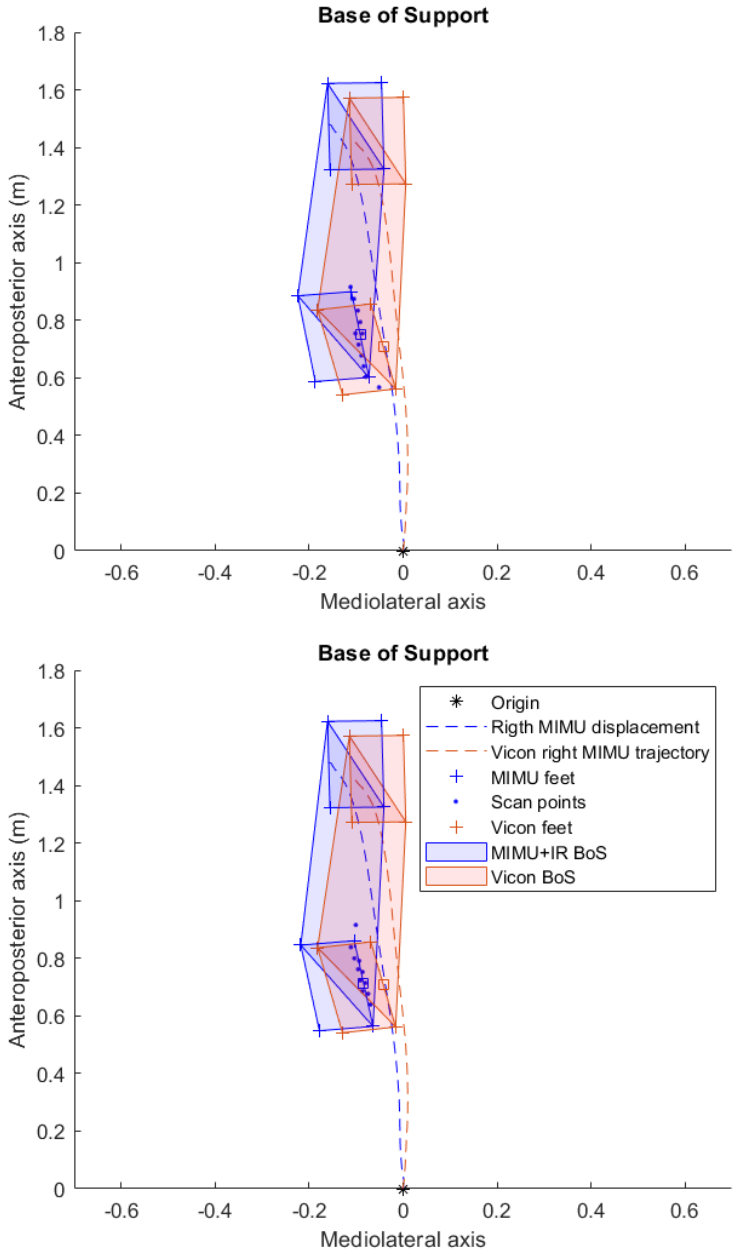

Figure 15.14: *These figures show the base of support obtained with Vicon and with MIMU and distance sensor for the same stride. The second is obtained not assuming that the DSs perceive a body only perpendicularly and giving less weight to the last distance data. It can be noticed that the centers of mass of the lateral side of the left foot (little squares on the lateral segment) have more similar positions along the anteroposterior axis in the second case. The mediolateral position of the left foot is not affected by the expedients adopted in the second image.*

It can be concluded, observing Figure 15.14, that the adopted corrections actually improve the anteroposterior left foot position estimation. Anyway, to implement a complete and robust method for improving the position of the detected foot, to test the algorithms on more subjects is necessary.

In conclusion, the proposed methods seem to be a promising solution for the estimation of gait spatial parameters, enabling to instrument a single foot with only wearable, lightweighted

and self-contained sensors. A great advantage is given by the presence of distance sensors, which enable to estimate not only the stride length, more common in literature, but also the step width and thus the base of support. Although this is a preliminary study aiming at proving the feasibility of these methods, so they were tested only on one healthy subject and it should be underlined that enlarging the number of people on whom they are tested, the algorithms' robustness can improve. The linear parameters (SL and SW) estimation suffers from errors that influence the estimation of the BoS. The first step to do in order to significantly improve the BoS estimation is to further investigate the displacement estimation from MIMU, trying to obtain a complete overlapping between the BoS from Vicon and BoS from MIMU and IR ToF sensors.

Chapter 16

General conclusions and future work

The estimation the BoS, defined as the area of the feet and between the feet in a double support phase, can provide useful information to evaluate gait disorders. This thesis proposed an innovative method for the estimation of the BoS during gait based on the use of wearable units integrating MIMU and IR ToF sensors. Main advantages of the proposed method consist in the capability of:

- estimating the BoS outside human motion analysis laboratories,
- performing ecological acquisitions during patient's daily life,
- increasing the observation periods to several hours,
- providing information about BoS by instrumenting a single foot.

In this study, the adopted wearable system included a MIMU and two IR ToF proximity sensors attached on the same support on the lateral internal side of a single instrumented foot.
In the current state of the art, measurements of the IFD and BoS are generally carried out using SP and force plates [8] [10]. In the last decades, the use of magnetic-inertial sensing is growing and currently considered as the most promising technology for the gait analysis outside the human motion analysis laboratory.
The MIMUs allow to measure acceleration and angular velocities signals and, by combining the latter information with local magnetic north description, to estimate the orientation of the rigid body on which they are attached with respect to a global coordinate system. The main limitation of MIMUs is that they are self-referenced and so they are not able to describe both feet in the same coordinate system [5].
To overcome this limitation, information on the relative position between feet is needed. In this research thesis, this quantity was achieved by using IR ToF distance sensors positioned on a foot. The proximity sensors measure the IFD when the feet face to each other and this is the unique information about the non-instrumented foot required by the proposed method.

The general methods include several steps, as the BoS estimation requires many different information. The BoS was considered as an irregular polygon, whose area is calculated knowing the coordinates of its vertices with respect to the same coordinate system. The principal innovative contribution of this thesis was the implementation and validation of methods for the orientation estimation, displacement estimation, as well as identification of a common reference system for both feet, by instrumenting a single foot for maximizing method acceptability and sensor wearability.

The validity of the output and estimated relevant quantities provided by each single sub-method was tested to evaluate the specific performance and accuracy.

The implemented sensor fusion algorithm was based on an optimisation of Madgwick's quaternion-based complementary filter [36]. The complete adopted filter enables the tuning of a single parameter, low computational cost, and the possibility to be implemented on microprocessor embedded with MIMU. Furthermore, it limits the ferromagnetic disturbances on heading, allowing the attitude to not be affected by them.
Specific experiments were carried out to highlight the errors of the orientation estimation. A MIMU was moved along a straight path to evaluate if the orientation estimation remained constant. It was used a Xsens MIMU [43] because its manufacture provides the orientation quaternions obtained with a Kalman filter. This orientation was assumed as a 'silver standard' for evaluating the performances of the implemented sensor fusion algorithm. This is reasonable because of the good performances of Xsens MIMU assessed by [68] [69]. Since the difference between the obtained Euler angles and the ones provided by Xsens MIMU manufacturer were below 0.5° in attitude and below 2° in heading, the implemented sensor fusion algorithm was assumed to be suitable for BoS application.

The displacement estimation is generally based on the double integration of the accelerations, which suffers from drift problems. The implemented method to estimate the displacement from the accelerometer data considered the foot-flat phases to force the velocity to be zero (ZUPT [52])), detected the integration instants within those phases and exploited the null velocity at the end of the integration interval to reduce the drift. To minimize the errors, the direct integration is weighted with a time-reverse integration which uses as initial condition the zero velocity at the end of the considered integration interval.
The accuracy of this method was evaluated by specific experiments. Considering as a gold standard an imposed displacement of 0.37 m, the RMSd value of the obtained errors was 0.042 m along the direction of the motion with the only direct integration and 0.036 m with the direct and reverse integration (DRI) [51]. Moving again MIMUs along a straight path of 0.037 m, the sensibility to the integration instants was evaluated integrating the same accelerometric signals changing the integration interval for a total of 11 different cases. The percentage error (using the DRI) was within the range of 7.8-11.7%. It could be deduced that the length of the interval has an impact to the displacement estimate even if, in this experiment, the maximum number of added samples is ten. On the other hand, considering the range of the percentage errors, this variation does not significantly affect the results.

A preliminary investigation on the use of the IR ToF to reconstruct the length of a detected surface was carried out with experiments on rigid bodies of known dimensions. The IR ToF sensors have a view cone of 25°, as declared in the datasheet [65]. It follows that they can see the depth of a detected body and not only the surface that it is wanted to detect. The geometry of the object can influence the detection.
To verify the dependence on the target geometry, two objects with different geometries were taken into account: a parallelepiped (with length of 0.19 m, height of 0.05 m and depth of the 0.14 cm) and a flat screen (with length of 0.30 m, height of 0.09 m and depth of 0.004 m). In both cases the results suggested that minimizing the mean square errors was a suitable method to fit the distance data to approximate the plane of the detected surface. Outliers due to border effect occurred in both cases but especially with the parallelepiped. They must be removed with proper thresholds to improve the fitting.
The reconstruction of the length of the rigid body, using the velocity obtained from the MIMU and the sampling interval time of the IR ToF sensors, showed a RMSd values of 0.033 m in the

case of the flat screen and 0.056 m in the case of the parallelepiped. As expected, these results highlighted that the accuracy is higher if the detected body is quite flat, reducing the outliers. A solution to avoid this error in length reconstruction is to impose the known length of the detected body to the linear model. This choice was adopted to prevent a further cause of error in the BoS estimation (where the length of the patient's foot can be easily measured by a ruler). Furthermore, also the accuracy of the slope of the linear model (representing the inclination of the detected body on the horizontal plane) was investigated in both objects: the obtained mean $\pm$ standard deviation was $7.2 \pm 4.2°$ for the parallelepiped and $2.9 \pm 1.7°$ for the flat screen. This result suggested that the presence of outliers is more emphatic if the depth of the object is higher. It can be assessed that the outliers at the beginning and at the end of the detection interval are due to two causes:

- the proximity sensors see the perpendicular side with respect to the one which had to be detected;
- the emitted and received IR waves of the proximity sensors do not just lie on the lines that start from the IR ToF sensors and perpendicularly intersect the object surface, so the DSs see the object before being exactly in front of it.

A solution to limit this error could be to rotate the initial and final values of the collected distance data of the IR ToF sensor view cone angle (25° as reported in [65]) on the horizontal plane.

The spatial gait parameters as obtained by the proposed methods were compared with those provided by the stereophotogrammetric gold standard.
The proposed methods were tested on a healthy subject walking at a self-selected velocity along a straight path of 5 m for ten times. The same experiment was performed with and without a flat screen on the non-instrumented foot to make the internal lateral surface more uniform. The extracted parameters were the stride length, the step width and the BoS. The accuracy for all of them has been evaluated.

The found absolute errors in the estimation of stride length were summarized in the mean $\pm$ standard deviation: 0.037 ± 0.064 m. Generally, the estimated values were higher than the actual stride length due to the drift, which is not completely removed. Since the actual length was between 1.3 and 1.6 m this is considered an acceptable error in the estimation of the stride length.

The step width was considered as the inter feet distance (IFD) measured by the IR ToF sensors when the feet face each other. For the sake of clarity, the step width was defined as the mean value of IFDs for every step. To quantify the errors, the SP data ware processed to obtain the distances between the proximity sensors and the detected surface of the non-instrumented foot. The accuracy of the two DSs was evaluated both separately and together and in case of the presence of the flat screen or not. All the steps of the trials were processed to achieve a as accurate as possible description of IR ToF performances.
The mean $\pm$ standard deviation of the absolute step width errors was 0.015 ± 0.017 m for DS REAR (the distance sensor nearer to the heel) and 0.031 ± 0.022 m for DS FRONT (the distance sensor nearer to the toe). This suggested that the DS FRONT had better performances (mean error difference of 0.016 m) and, if a single IR ToF can be used, the fore position is suggested.
Considering both the DSs data, the mean $\pm$ standard deviation of the absolute step width errors was 0.023 ± 0.021 m in case of the presence of the flat screen and 0.027 ± 0.032 without the flat screen. The mean error difference of 0.006 m suggested that the accuracy is higher if the detected side of the non-instrumented foot is uniform. Although, the calculated 95% confidence intervals (CIs) showed that the errors were not statistically different in the analysed cases since

the CIs partially overlapped.
These results describe errors that cannot be eliminated in the BoS estimation, since the IFD estimate depends only on the distance data, thus also the positioning of the non-instrumented foot significantly depends on them.

The BoS is estimated calculating the area of the feet, modelled as rectangles, and the area between them while the non-instrumented foot is in stance phase and the instrumented foot touches the ground after the swing which performs the 'scan'. The errors between the SP BoS and the obtained BoS are evaluated both in terms of area (m^2) and position on the floor (right foot shift and left foot shift) (m).
The absolute mean value ± standard deviation of the area error was 0.0041 ± 0.0063 m^2 with the flat screen and 0.0125 ± 0.0345 m^2 without the flat screen. This is consistent with the result found for the SW estimation that affects the BoS estimates, which have a mean value of 0.0084 m^2 higher in case without the flat screen.
The displacement estimation of the right foot is not affected by the presence of the flat screen, while the left foot shift comprises the error of the IFD estimate by the DSs. The left foot shift mean value is higher of 0.007 m if the flat screen is not attached on the left foot. The left shift is 0.055 ± 0.024 with the flat screen and 0.062 ± 0.027 without the flat screen. Anyway, also in this case, the errors are not statistically different, considering the 95% CI.
These errors include imprecisions derived from:

- the position estimation of the instrumented foot at the end of the swing phase,
- the orientation estimation of the instrumented foot,
- the inaccuracy of the distance data from the proximity sensors.

The estimate of the position of the instrumented foot is the principal cause of error among the three bullet points above. It influences not only the positioning of the instrumented foot itself but also the positioning of the other foot. These results suggest that an improvement of the BoS estimation is required to reduce errors associated to the displacement estimation, optimizing the DRI. Future work is needed to improve the BoS positioning of the area, making it overlapped with the BoS from the gold standard. Furthermore, methods' robustness should be tested on a larger number of subjects.
In conclusion, the present research has shown that the use of MIMU and IR ToF sensors attached on a single foot represent a promising solution for providing a more complete description of the gait spatial parameters during the daily activities by adding information related to the base of support. Future work should aim to improve algorithms of displacement estimation and test the methods on patients with gait disorders.

Part IV

Appendix

Chapter 17

Appendix A- Madgwick's filter

This appendix deals with the Madwick's filter [36]. It follows a mathematical derivation of the orientation estimate. In the following mathematical formulation, the leading superscript refers to the frame which is described by the one indicated by the leading subscript. The estimated orientation of the sensor frame relative to the Earth frame ${}^{E}_{L}q_{est,t}$ is obtained through the combination of the orientation quaternions calculated separately from the gyroscope (${}^{E}_{L}q_{\omega,t}$) and the vector observations (${}^{E}_{L}q_{\nabla,t}$). Madgwick in [55] declares that the level of accuracy of this filter is sufficient in human motion applications. The performance was tested by the author with a comparison with the Kalman filter provided by Xsens Technologies with MTx orientation sensors [43]. Both filters are evaluated using the same data sensors and their errors were calculated with respect to a Vicon system. The errors are quantified as Root-Mean-Square (RMS) of the static and dynamic roll (θ), pitch (ϕ) and heading (ψ) differences with the optical reference. The experiment consisted of a series of rotations made by hand. All of the reported angles errors are lower than 1.2° and are in general even lower than the ones of the Xsens Kalman filter.

17.1 Orientation from angular rate

The orientation from the angular rate starts from calculating the rate of change of the orientation of the ECS relative to the LCS (${}^{E}_{L}\dot{q}$):

$$ {}^{E}_{L}\dot{q} = \frac{1}{2} {}^{E}_{L}\hat{q} \ \otimes \ \omega^{L} \tag{17.1} $$

where $\omega^{S} = \ [0 \ \omega_x \ \ \omega_y \ \ \omega_z \ ]$ is the angular rate around each axis expressed in rad^{-1}. The orientation of the Earth frame relative to the sensor frame at time t, ${}^{E}_{L}\hat{q}_{\omega,t}$, can be thus evaluated by integrating the quaternion derivative:

$$ {}^{E}_{L}\dot{q}_{\omega,t} = \frac{1}{2} {}^{E}_{L}\hat{q}_{est,t-1} \ \otimes \ \omega^{L}_{t} \tag{17.2} $$

$$ {}^{E}_{L}\hat{q}_{\omega,t} = \ {}^{E}_{L}\hat{q}_{est,t-1} + {}^{E}_{L}\dot{q}_{\omega,t} \ \triangle t \tag{17.3} $$

where ω^{L}_{t} is the angular measurement at time t, $\triangle t$ is the sampling period and ${}^{E}_{L}\hat{q}_{est,t-1}$ is the previous estimate of orientation.

17.2 Orientation from Earth's vectors observations

The estimated orientation based on the vector observations initially assumes that the accelerometer and the magnetometer measure respectively only gravity and only the Earth's magnetic field. This part of the algorithm is divided into the calculation of a quaternion related to the gravity and one related to the magnetic field, that subsequently are combined together in an unique formulation. The orientation of the sensor ${}^{E}_{L}\hat{q}$ must align a predefined reference direction of the field in the ECS ($\hat{d}^E = [0\ d_x\ d_y\ d_z]$) with the measured direction of that field in the LCS ($\hat{s}^L = [0\ s_x\ s_y\ s_z]$). The resolution is presented as an optimisation problem with a cost function that has to be minimized f:

$$f({}^{E}_{L}\hat{q}, \hat{d}^E, \hat{s}^L) = {}^{E}_{L}\hat{q}^* \otimes \hat{d}^E\ x\ {}^{E}_{L}\hat{q} - \hat{s}^L \tag{17.4}$$

Among the various possible optimisation algorithms, the gradient descent algorithm is the one selected due to its simplicity to solve the optimization problem. This method is based on the relation between the direction of the fastest decrease in a certain point of a multi-variable function and the gradient evaluated in that point, which are opposite. The following equations describe the gradient descent algorithm for n iterations to estimate the orientation estimation ${}^{E}_{L}q_{k+1}$ from the value of the orientation of the previous iteration and a step-size μ. It should be underlined that, as expressed in Equation 17.6, the gradient of a function described in a point is equal to the transpose of the Jacobian of that function evaluated in the same point, multiplied for the function evaluated in that point.

$${}^{E}_{L}q_{k+1} = {}^{E}_{L}\hat{q}_k - \mu\frac{\nabla f({}^{E}_{L}\hat{q}_k, \hat{d}^E, \hat{s}^L)}{||\nabla f({}^{E}_{L}\hat{q}_k, \hat{d}^E, \hat{s}^L)||} \quad k = 0, 1, 2, ...n \tag{17.5}$$

$$\nabla f({}^{S}_{E}\hat{q}_k, \hat{d}^E, \hat{s}^L) = J^T({}^{S}_{E}\hat{q}_k, \hat{d}^E) f({}^{S}_{E}\hat{q}_k, \hat{d}^E, \hat{s}^S) \tag{17.6}$$

$$f({}^{E}_{L}\hat{q}_k, \hat{d}^E, \hat{s}^L) = \begin{bmatrix} 2d_x(\frac{1}{2} - q_3^2 - q_4^2) + 2d_y(q_1q_4 + q_2q_3) + 2d_z(q_2q_4 - q_1q_3) - s_x \\ 2d_x(q_2q_3 - q_1q_4) + 2d_y\left(\frac{1}{2} - q_2^2 - q_4^2\right) + 2d_z(q_1q_2 + q_3q_4) - s_y \\ 2d_x(q_1q_3 + q_2q_4) + 2d_y(q_3q_4 - q_1q_2) + 2d_z(\frac{1}{2} - q_2^2 - q_3^2) - s_z \end{bmatrix} \tag{17.7}$$

$$J({}^{E}_{L}\hat{q}_k, \hat{d}^E) = \tag{17.8}$$
$$\begin{bmatrix} 2d_yq_4 - 2d_zq_3 & 2d_yq_3 - 2d_zq_4 & -4d_xq_3 + 2d_zq_2 - 2d_zq_1 & -4d_xq_4 + 2d_yq_1 - 2d_zq_2 \\ -2d_xq_4 - 2d_zq_2 & 2d_xq_3 - 4d_yq_2 + 2d_zq_1 & 2d_xq_2 + 2d_zq_4 & -2d_xq_1 - 4d_yq_4 + 2d_zq_3 \\ 2d_xq_3 - 2d_yq_2 & 2d_xq_4 - 2d_yq_1 - 4d_zq_2 & 2d_xq_1 + 2d_yq_4 - 4d_zq_3 & +2d_xq_2 + 2d_yq_3 \end{bmatrix}$$

The above equations are valid for both gravity and magnetic field vectors and, in both cases, the equations of f_g, f_b, J_g, and J_b are simplified since the directions of the fields are assumed to have components within one or two of the principal axes of the global coordinate frame. The subscript g indicates the objective function or Jacobian related to the gravity vector, while the subscript b to the ones of the Earth's magnetic field. The direction of the gravity defines the vertical axis (z axis), while the magnetic field has components in horizontal and vertical axes (x axis and z axis). It is acceptable to compute one iteration per time sample, since [36] assesses that the convergence rate is not lower than the physical rate of orientation change. μ influences that convergence and depends on the time sample considered, so it has to be chosen properly to ensure the convergence rate of ${}^{E}_{L}q_{\nabla,t}$. The overshooting due to too high mu must be avoided, limiting μ

to the physical orientation rate of the sensor, because μ can be increased by measurement noise both in accelerometer and magnetometer. In conclusion, the estimation of orientation based on the vector observation is obtained by intersecting the two objective functions relative to accelerometer and magnetometer (Equation 17.10). A single vector observation cannot provide a complete orientation estimation, indeed a single objective function identify a line ha minimum solutions. Thus, f merges two objective functions and its minimum is identified by a unique point, the quaternion orientation.

$$ {}^{E}_{L}\hat{q}_{\nabla,t} = \ {}^{E}_{L}\hat{q}_{est,t-1} - \mu_t \frac{\nabla f}{||\nabla f||} \tag{17.9} $$

$$ \nabla f = J_{g,b}{}^{T}({}^{E}_{L}\hat{q}_{est,t-1}, \hat{b}^{E}) f_{g,b}({}^{E}_{L}\hat{q}_{est,t-1}, \hat{a}^{L}, \hat{b}^{E}, \hat{m}^{L}) \tag{17.10} $$

where $\hat{m}^L$ and $\hat{a}^L$ stands for $\hat{s}^L$, while $\hat{b}^E$ for $\hat{d}^E$. Indeed $\hat{m}^L$ is the normalised magnetometer measurement expressed in LCS, $\hat{a}^L$ is the normalised accelerometer measurement, $\hat{b}^E$ is the magnetic field in ECS.

17.3 Filter fusion

The filter fusion algorithm consists in combining these two orientations founded separately from gyroscope and accelerometer with magnetometer:

$$ {}^{E}_{L}\hat{q}_{est,t} = \ \gamma_t {}^{E}_{L}\hat{q}_{\nabla,t} + (1-\gamma_t) {}^{E}_{L}\hat{q}_{\omega,t}, \quad 0 \leq \gamma_t \leq 1 \tag{17.11} $$

As stated by Magdwick (29), an optimal value of γ_t can be define as that which ensures the weighted divergence of ${}^{S}_{E}q_{\omega,t}$ is equal to the weighted convergence of ${}^{S}_{E}q_{\nabla,t}$ and so it derives that:

$$ \gamma_t = \frac{\beta}{\frac{\mu}{\triangle t} + \beta} \tag{17.12} $$

$\frac{\mu}{\triangle t}$ is a term describing the rate of convergence of the estimate based on accelerometer and magnetometer, ${}^{S}_{E}\hat{q}_{\nabla}$, and β is the factor related to the divergence rate of the quaternion coming from the integration of the angular rate, ${}^{S}_{E}\hat{q}_{\omega}$, so the gyroscope measurement errors with null mean. Although, considering a high value of μ with respect to β, the equations can be simplify and the final expression of the estimated complete orientation, which fuses the Equation 17.3 and 17.9 is the following, as it can be seen in the block diagram in Figure 17.1.

$$ {}^{E}_{L}\hat{q}_{est,t} = {}^{E}_{L}\hat{q}_{est,t-1} + \triangle t({}^{E}_{L}\dot{q}_{\omega,t} - \beta \frac{\nabla f}{||\nabla f||}) \tag{17.13} $$

17.4 On-line magnetic distortion compensation

Furthermore, since the vicinity of the magnetometer to ferromagnetic elements, electrical appliances, metal furniture or structures induces distortion, a magnetic distortion compensation is needed. Declination errors, so the ones in horizontal plane of the Earth's surface, can be corrected only with an additional reference of heading. Inclination errors, so the ones in the vertical plane with respect to Earth's surface, may be compensated with an additional measurement of attitude. The accelerometer is the only other sensor that provides a vector, so the gravity, with its vertical direction, can be used for the compensation only of inclination errors. At every time step the magnetometer data is rotated with the previous estimated quaternion. Possible errors of inclination are corrected imposing that the rotated magnetometer data, expressed in

ECS, $\hat{h}_t^E$, coincides with the direction of the Earth's magnetic field $\hat{b}_t^E$. It is achieved by forcing $\hat{b}_t^E$ to have the same component on z axis of $\hat{h}_t^E$ and x component equal to the sum of both x and y components of $\hat{h}_t^E$. Mathematically, the effect of a wrong inclination of the measured direction of the Earth's magnetic field $\hat{h}_t^E$ can be corrected imposing that the reference direction of Earth's magnetic field $\hat{b}_t^E$ is of the same inclination. It is consequentely done by computing $\hat{b}_t^E$ with only x and z components as follow (29):

$$\hat{h}_t^E \;=\; [0 \; h_x \; h_y \; h_z] = {}^E_L\hat{q}_{est,t-1} \otimes \hat{m}_t^S \otimes {}^E_L\hat{q}^*_{est,t-1} \tag{17.14}$$

$$\hat{b}_t^E = \; [0 \; \sqrt{h_x^2 + h_y^2} \;\; 0 \;\; h_z^2] \tag{17.15}$$

This way of compensation enables to limit the magnetic disturbances to affect only the estimated heading component of orientation.

17.5 Gyroscope bias drift compensation

The gyroscope bias has to be compensated since it would lead to important drift in integration and increases with temperature and over time and motion. It is not necessary a Kalman filter to estimate the gyroscope bias as an additional state within the system model. In fact, it is sufficient the information of the error in the rate of change of orientation [36]. The angular error in each gyroscope axis is thus expressed as the error in the rate of change of orientation, ω_ϵ^L, derived from the inverse of the equation 17.2. The gyroscope bias ω_b^L is composed by the DC component of ω_ϵ^L and thus it can be obtain low-filtering ω_ϵ^L through an integral weighted by an appropriate gain ζ. This is the second gain or parameter that has to be set in this algorithm, together with β. The integral gain ζ defines the rate of convergence of the estimated gyroscope bias, $\omega_{b,t}^L$.

$$\omega_{\varepsilon,t}^L \;=\; 2{}^S_E\hat{q}^*_{est,t-1} \;\otimes\; {}^E_L\dot{\hat{q}}_{\varepsilon,t} \tag{17.16}$$

$${}^E_L\dot{\hat{q}}_{\varepsilon,t} = \frac{\nabla f}{||\nabla f||} \tag{17.17}$$

$$\omega_{b,t}^L \;= \zeta \sum_t \omega_{\varepsilon,t}^L \; \triangle t \tag{17.18}$$

Once estimated the bias, the compensated measures of angular rates are the following and can be used instead of the gyroscope readings in the rest of the code, since Equation 17.1.

$$\omega_{c,t}^L \;=\; \omega_t^L - \; \omega_{b,t}^L \tag{17.19}$$

Since the bias is a significant problem, in this study the bias in static periods is also calculated and, with an possible interpolation of the initial and final values, removed from the entire readings.

17.6 Adjustable parameters

As it can be seen in Figure 17.1, in the entire algorithm, the only two parameters that have to be set are:

1. β is related to the zero mean gyroscope measurement errors;

2. ζ is related to the gyroscope errors with non-null mean, the biases. Indeed it represents the rate of convergence to remove gyroscope bias drift.

Both of them are expressed as magnitudes of a quaternion derivative. β could be initialised as the estimate of the zero mean gyroscope measurement errors, which is its minimum acceptable value. Its optimal value is high enough to minimises drift errors but also sufficiently low enough to avoid the introduction of noise due to too large steps of gradient descent iterations, [55]. The use of large gains improves the convergence of the filter from initial conditions in the initialisation phase.

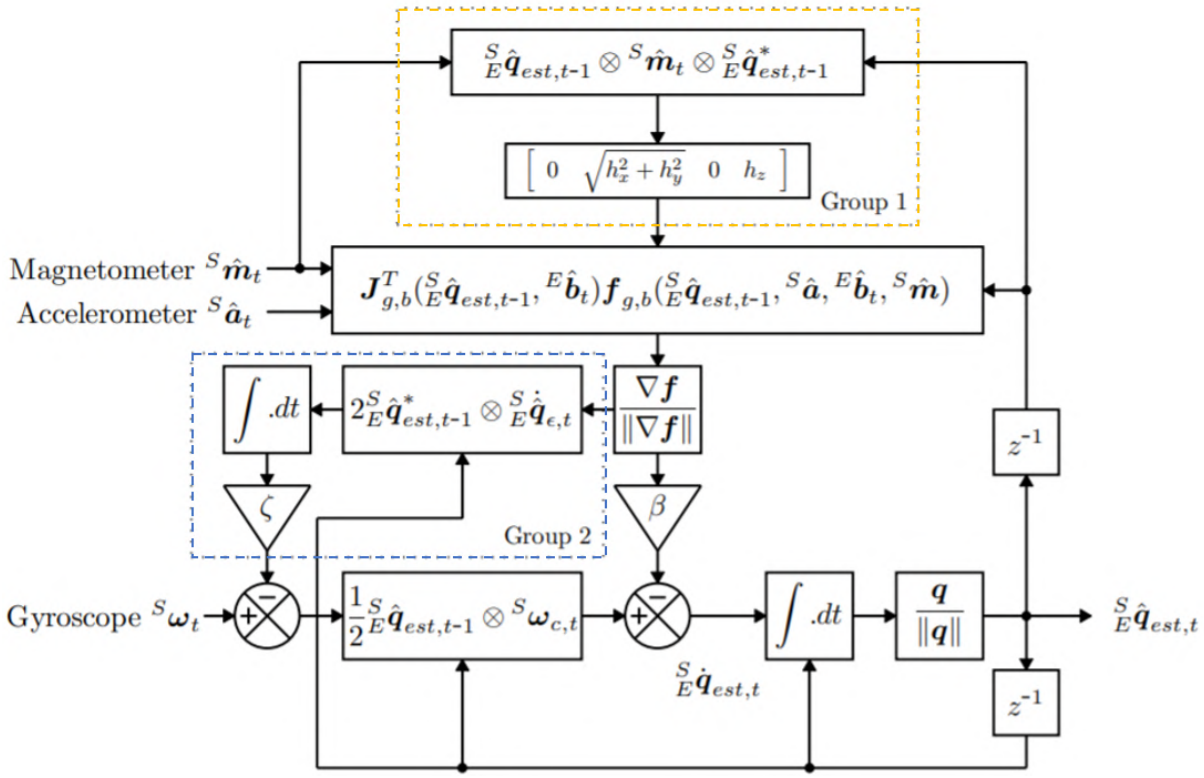

Figure 17.1: *Block diagram representation of Madgwick's complete orientation filter, including magnetic distortion (Group 1, yellow) and gyroscope drift (Group 2, blue) compensation, (29). Madwick considers the coniugate of the quaternions described in this chapter, thus to make the variables names to coincide with the mathematical explaination in this Chapter, S has to be substituded with E and E with L.*

Bibliography

[1] Della Croce U., Cereatti A., Mancini M., *Gait Parameters Estimated Using Inertial Measurement Units.* Springer, 1-21, 2017.

[2] Bertoli M., Cereatti A., Trojaniello D., *Estimation of spatio-temporal parameters of gait from magneto-inertial measurement units: multicenter validation among Parkinson, mildly cognitively impaired and healthy older adults.* Biomedical Engineering OnLine, 17:58, 2018.

[3] Salarian A., Russmann H., Vingerhoets FJG., Dehollain C., Blanc Y., Burkhard PR., et al., *Gait Assessment in Parkinson's Disease: Toward an Ambulatory System for Long-Term Monitoring.* IEEE Transactions on Biomedical Engineering, 51(8):1434–43, 2004.

[4] Muro-de-la-Herran A, García-Zapirain B, Méndez-Zorrilla A., *Gait analysis methods: An overview of wearable and non-wearable systems, highlighting clinical applications.* Sensors (Switzerland), 14(2):3362–94, 2014.

[5] Sabatini A.M., *Estimating three-dimensional orientation of human body parts by inertial/magnetic sensing.* Sensors, 11(2):1489–525, 2011.

[6] Bertuletti S., Cereatti A., Comotti D., Caldara M., Della Croce U., *Static and dynamic accuracy of an innovative miniaturized wearable platform for short range distance measurements for human movement applications.* Sensors (Switzerland), 17(7):1–15, 2017.

[7] Lugade V., Lin V., Chou LS., *Center of mass and base of support interaction during gait.* Gait Posture, 33(3):406–11, 2013. Available from: http://dx.doi.org/10.1016/j.gaitpost.2010.12.013

[8] Caderby T., Yiou E., Peyrot N., Begon M., Dalleau G., *Influence of gait speed on the control of mediolateral dynamic stability during gait initiation.* Journal of Biomechanics, 47(2):417–23, 2014. Available from: http://dx.doi.org/10.1016/j.jbiomech.2013.11.011

[9] Caderby T., Yiou E., Peyrot N., Bonazzi B., Dalleau G., *Gait Parameters Estimated Using Inertial Measurement UnitsDetection of swing heel-off event in gait initiation using force-plate data.* Gait and Posture, 37(3):463–6, 2013. Available from: http://dx.doi.org/10.1016/j.gaitpost.2012.08.011

[10] Yiou E., Teyssèdre C., *Yiou E, Teyssèdre C. Comparison of base of support size during gait initiation using force-plate and motion-capture system: A Bland and Altman analysis.* Journal of Biomechanics, 49:4168–72, 2016.

[11] Arvin M., Mazaheri M., Hoozemans MJM., Pijnappels M., Burger BJ., Verschueren SMP, et al. , *Effects of narrow base gait on mediolateral balance control in young and older adults.* Journal of Biomechanics, 49(7):1264–7, 2016. Available from: http://dx.doi.org/10.1016/j.jbiomech.2016.03.011.

[12] Honeine J-L., Schieppati M., Gagey O., *By counteracting gravity, triceps surae sets both kinematics and kinetics of gait.* Physiological Reports, 2(2):e00229, 2014.

[13] Stins JF., Beek PJ., *Organization of voluntary stepping in response to emotion-inducing pictures.* Gait and Posture, 34(2):164–8, 2011. Available from: http://dx.doi.org/10.1016/j.gaitpost.2011.04.002.

[14] Yiou E., Do MC., *Control of mediolateral stability during rapid step initiation with preferred and non-preferred leg: Is it symmetrical?* Gait Posture, 32(1):145–7, 2010. Available from: http://dx.doi.org/10.1016/j.gaitpost.2010.03.018

[15] Brenière Y., Cuong Do M., Bouisset S., *Are dynamic phenomena prior to stepping essential to walking?* Journal of Motor Behaviour, 19(1):62–76, 1987.

[16] Bril B., Brenière Y., *Postural requirements and progression velocity in young walkers.* Journal of Motor Behaviour, 24(1):105–16, 1992.

[17] Weenk D., Roetenberg D., Van Beijnum BJJF., Hermens HJ., Veltink PH., *Ambulatory estimation of relative foot positions by fusing ultrasound and inertial sensor data.* IEEE Transactions on Neural Systems Rehabilitation Engineering, 23(5):817–26, 2015.

[18] Hung TN., Suh YS., *Inertial sensor-based two feet motion tracking for gait analysis.* Sensors, 13, 5614-5629, 2013.

[19] Trojaniello D., Cereatti A., Bourke AK., Aminian K., Della Croce U., *A waerable system for the measurement of the inter-foot distance during gait.* 20th IMEKO TC4 International Symposium and 18th International Workshop on ADC Modelling and Testing, 2014.

[20] Merat P., Harvey E.J., Mitsis G.D., *A miniature multi-sensor shoe-mounted platform for accurate positioning.* IEEE International Conference on Systems, Man, and Cybernetics, pp. 2772-2777, 2018.

[21] Arami A., Saint Raymond N., Aminian K., *An accurate wearable foot clearence estimation system: towards a real time measurement system.* IEEE Sensors Journal, vol. 17, no. 8, pp. 2542–2549, 2017.

[22] Duong P.D., Suh S., *Foot pose estimation using an inertial sensor unit and two distance sensors.* Sensors, vol. 15, no. 7, pp. 15 888– 15 902, 2015.

[23] Peruzzi A., Della Croce U., Cereatti A., *Estimation of stride length in level walking using an inertial measurement unit attached to the foot: A validation of the zero velocity assumption during stance.*Journal of Biomechanics, 44(10):1991–4, 2011.

[24] Teufl W., Lorenz M., Miezal M., Taetz B., Fröhlich M., Bleser G., *Towards Inertial Sensor Based Mobile Gait Analysis: Event-Detection ans Spatio-Temporal Parameters.* Sensors, 1–20, 2019.

[25] Perry, J., and Burnfield, J. M., *Gait Analysis: Normal and Pathological Function.* 2010

[26] Agostini V., Balestra G., Knaflitz M., *Segmentation and Classi fi cation of Gait Cycles.* IEEE Transactions on Neural Systems Rehabilitation Engineering, 22(5):946–52, 2014.

[27] Krebs DE., Goldvasser D., *Is Base of Support Greater in Unsteady Gait?* Physical Therapy, 82(2):138–47, 2002.

[28] Hollands M., Sorensen K., Patla A., *Effects of head immobilization on the coordination and control of head and body reorientation and translation during steering.* Experimental Brain Research, 140(2):223–33, 2001.

[29] Brach JS., Berthold R., Craik R., VanSwearingen JM., Newman AB., *Gait variability in community-dwelling older adults.* Journal of the Americam Geriatrics Society, 49(12):1646–50, 2001.

[30] Huxham F., Gong J., Baker R., Morris M., Iansek R., *Defining spatial parameters for non-linear walking.* Gait and Posture, 23(2):159–63, 2006.

[31] Pirker W., Katzenschlager R., *Gait disorders in adults and the elderly.* The central European Journal of Medicine, 81–95, 2017.

[32] Lambrecht S., Harutyunyan A., Tanghe K., Afschrift M., Schutter J., Jonkers I., *Real-Time Gait Event Detection Based on Kinematic Data Coupled to a Biomechanical Model.* Sensors, 17-671, 2017.

[33] Cappozzo A., Della U., Leardini A., Chiari L., *Human movement analysis using stereophotogrammetry Part 1: theoretical background.* Gait and Posture, 21:186–96, 2005.

[34] Roetenberg D., *Inertial and Magnetic Sensing of Human Motion.* PhD Thesis, 2006.

[35] Valenti RG., Dryanovski I., Xiao J., *Keeping a good attitude: A quaternion-based orientation filter for IMUs and MARGs.* Sensors (Switzerland), 15(8):19302–30, 2015.

[36] Madgwick S., *An efficient orientation filter for inertial and magneto-inertial sensor arrays.* Report x-io and University of Bristol, 2010.

[37] Pacini Panebianco G., Bisi MC., Stagni R., Fantozzi S., *Gait and Posture Analysis of the performance of 17 algorithms from a systematic review: Influence of sensor position, analysed variable and computational approach in gait timing estimation from IMU measurements.* Gait and Posture, 66(August):76-82, 2018. Available from: https://doi.org/10.1016/j.gaitpost.2018.08.025

[38] Mathie MJ., Coster ACF., Lovell NH., *Accelerometry: Providing an Integrated, Practical Method for Long-Term, Ambulatory Monitoring of Human Movement Accelerometry: providing an integrated, practical method for long-term, ambulatory monitoring of human movement.* 2004.

[39] Luinge HJ., *Inertial Sensing of Human Movement*, PhD Thesis, 2002.

[40] Hamza-lup FG., *Kinesthetic Learning – Haptic User Interfaces for Gyroscopic Precession Kinesthetic Learning – Haptic User Interfaces for Gyroscopic Precession Simulation* 2019;(March).

[41] Nguyen MN., Ha NS., Nguyen LQ., Chu HM., *Z-Axis Micromachined Tuning Fork Gyroscope with Low Air Damping* 2017;1–10.

[42] Sun J., Kosel J., *Finite-Element Modelling and Analysis of Hall effect and Extraordinary Magnetoresistance Effect.* Available from: http://dx.doi.org/10.5772/47777

[43] MTi and MTx User Manual and Technical Documentation- Xsens Technologies B.V., 2009.

[44] Afzal MH., Renaudin V., Lachapelle G., *Use of Earth's Magnetic Field for Mitigating Gyroscope Errors Regardless of Magnetic Perturbation.* Sensors, 2011.

[45] Bertuletti S., Della Croce U., Cereatti A., *A wearable solution for accurate step detection based on the direct measurement of the inter-foot distance.* Journal of Biomechanics, 84:274–7, 2019. Available from: https://doi.org/10.1016/j.jbiomech.2018.12.039.

[46] Shuster MD, Oh SD., *Three-axis attitude determination from vector observations.* Journal of Guidance, Control and Dynamics, 4(1):70–7, 2008.

[47] Islam T., Islam S. et al., *Comparison of complementary and Kalman filter based data fusion for attitude heading reference system Comparison of Complementary and Kalman Filter Based Data Fusion for Attitude Heading Reference System.* AIP Conference Proceedings, 2018.

[48] Kalman R.E., *A New Approach to Linear Filtering and Prediction Problems.* Journal of Basic Engineering, 1960.

[49] Ameid T., Menacer A., Talhaoui H., Harzelli I., *Rotor resistance estimation using Extended Kalman fi lter and spectral analysis for rotor bar fault diagnosis of sensorless vector control induction motor.* Measurement, 111(February):243–59, 2017. Available from: http://dx.doi.org/10.1016/j.measurement.2017.07.039

[50] Bergamini E., *Estimating Orientation Using Magnetic and Inertial Sensors and Different Sensor Fusion Approaches: Accuracy Assessment in Manual and Locomotion Tasks.* Sensors, 2014.

[51] Zok M., Mazzà C., Della Croce U., *Total body centre of mass displacement estimated using ground reactions during transitory motor tasks: Application to step ascent.* Medical Engineering and Physics, 26(9 SPEC.ISS.):791–8, 2014.

[52] Skog I., Händel P., Skog I., Andel PH., *Zero-Velocity Detection — An Algorithm Evaluation.* IEEE Transcations on Biomedical Engineering, 2010.

[53] Trojaniello D., Cereatti A., Pelosin E., Avanzino L., Mirelman A., Hausdorff JM., et al., *Zero-Velocity Detection - An Algorithm Evaluation.Estimation of step-by-step spatio-temporal parameters of normal and impaired gait using shank-mounted magneto-inertial sensors: Application to elderly, hemiparetic, parkinsonian and choreic gait.* Journal of NueroEngineering and Rehabilitation, 11(1):152, 2014.

[54] Mahony R., Hamel T., Pflimli JM., *Nonlinear Complementary Filters on the Special Orthogonal Group.* IEEE Transcations on Automatic Control, 53(5):1203–18, 2008.

[55] Madgwick S., Harrison AJL., Vaidyanathan R., *Estimation of IMU and MARG orientation using a gradient descent algorithm.* IEEE International Conference on Rehabilitation Robotics, 2011.

[56] Mariani B., Hoskovec C., Rochat S., Büla C., Penders J., Aminian K., *3D gait assessment in young and elderly subjects using foot-worn inertial sensors.*Journal of Biomechanics, 43(15):2999–3006, 2010.

[57] Hao M., Chen K., Fu C., *Smoother-based 3D foot trajectoy estimation using inertial sensors.* IEEE, 0018-9294 (c), 2018.

[58] Rodgers MM., *Dynamic biomechanics of the normal foot and ankle during walking and running.* Physical Therapy, 68(12):1822–30, 1988. Available from: http://www.ncbi.nlm.nih.gov/pubmed/3057519.

[59] Winter DA., *Kinematic and kinetic patterns in human gait: Variability and compensating effects.* Human Movement Science, 3(1–2):51-76, 1984.

[60] Sabatini AM., Martelloni C., Scapellato S., Cavallo F., *Assessment of walking features from foot inertial sensing.* IEEE Transcations on Biomedical Engineering, 52(3):486–94, 2005.

[61] Schepers HM., Koopman HFJM., Veltink PH., *Ambulatory assessment of ankle and foot dynamics.* IEEE Transcations on Biomedical Engineering, 54(5):895–902, 2007.

[62] Trojaniello D., *Assessment of gait spatio-temporal parameters in neurological disorders using wearable inertial sensors.* PhD Thesis, 2015.

[63] Mannini A., Sabatini AM., *Gait phase detection and discrimination between walking – jogging activities using hidden Markov models applied to foot motion data from a gyroscope.* Gait and Posture, 36(4):657–61, 2012. Available from: http://dx.doi.org/10.1016/j.gaitpost.2012.06.017

[64] El-Sheimy N., *Emerging MEMS IMU and its impact on mapping applications.* Photogrammetric week, 2009.

[65] STMicroelectronics VL6180X. Available from: http://www.st.com/content/st_com/en/products/imaging-and-photonics-solutions/proximity-sensors/vl6180x.html

[66] INDIP Datasheet, UniSS, 2019.

[67] Zhang JT., Novak AC., Brouwer Li Q., *Concurrent validation of Xsens MVN measurement of lower limb joint kinematics.* Physiological Measurement, 34(8):N63-9, 2013.

[68] *Xsens MVN: Full 6DOF Human Motion Tracking Using Miniature Inertial Sensors.* Xsens Technologies, 2013.

[69] Roetenberg D., Luinge H., Baten C., and Veltink P., *Compensation of magnetic disturbances improves inertial and magnetic sensing of human body segment orientation.* IEEE Transactions on Neural Systems and Rehabilitation Engineering, vol. 13, pp. 395–405, 2005.